



UNIVERSITÀ DEGLI STUDI DI BARI  
ALDO MORO

---

Dipartimento Interateneo di Fisica "M. Merlin"

DOTTORATO DI RICERCA IN FISICA Ciclo XXIII

Detection of Gamma Ray Bursts  
by *Fermi* Space Telescope

Settore scientifico-disciplinare: FIS/05

Tutore:  
Ch.mo Prof. Paolo Spinelli

Studente di Dottorato  
Dott. Francesco de Palma

Ciclo di Dottorato XXIII  
Anno Accademico 2010/2011



# Contents

<b>Introduction</b>	<b>1</b>
<b>1 Gamma-ray Bursts</b>	<b>3</b>
1.1 Introduction . . . . .	3
1.2 Discovery and relevant observations . . . . .	3
1.3 Main Spectral characteristics . . . . .	5
1.4 High Energies characteristics (before <i>Fermi</i> ) . . . . .	8
1.5 GRBs classifications . . . . .	9
1.6 Progenitors . . . . .	11
1.6.1 Observations: long bursts . . . . .	12
1.6.2 Theoretical models: long bursts . . . . .	14
1.6.3 Theoretical models and observation: short bursts . . . . .	16
1.7 Central Engine . . . . .	18
1.8 Accretion Flows . . . . .	21
1.9 Jet production . . . . .	22
1.10 Prompt emission model . . . . .	24
1.10.1 Fireball expansion and shocks . . . . .	24
1.10.2 Synchrotron shock model . . . . .	27
<b>2 Apparatus description</b>	<b>29</b>
2.1 Introduction . . . . .	29
2.2 LAT overview . . . . .	29
2.3 ACD . . . . .	31
2.4 Tracker . . . . .	34
2.5 Calorimeter . . . . .	38
2.6 DAQ and trigger logic . . . . .	41
2.7 Event reconstruction . . . . .	45
2.8 Event classification . . . . .	50
2.9 LAT Instrument Response Function . . . . .	52
2.9.1 IRFs versions . . . . .	53
2.9.2 Effective Area, Acceptance and Field of View . . . . .	55
2.9.3 Point Spread Function . . . . .	57
2.9.4 Energy Dispersion . . . . .	58
2.9.5 GRB sensitivity . . . . .	59

2.10	Time resolution . . . . .	59
2.11	Data product . . . . .	62
2.12	Automated LAT GRB search . . . . .	63
2.12.1	Onboard LAT Detection . . . . .	63
2.12.2	LAT onground Blind Search . . . . .	64
2.13	The Fermi Gamma Ray Burst Monitor . . . . .	64
2.13.1	GBM triggers . . . . .	66
2.13.2	GBM locations . . . . .	67
2.13.3	GBM response function . . . . .	68
2.14	Fermi Orbital characteristics . . . . .	69
2.14.1	Operational (LAT) mode: Survey, Maneuver and ARR . . . . .	69
2.14.2	South Atlantic Anomaly . . . . .	70
2.15	GCN system . . . . .	71
<b>3</b>	<b>GRBs observed by <i>Fermi</i></b>	<b>75</b>
3.1	Observed characteristics . . . . .	75
3.1.1	Delayed onset of the high energy emission . . . . .	78
3.1.2	Extra spectral component . . . . .	79
3.1.3	Long lived high-energy emission . . . . .	80
3.2	GRB090902B . . . . .	81
3.2.1	Detection and Observation . . . . .	81
3.2.2	Spectral characteristics . . . . .	82
3.2.3	Theoretical analysis . . . . .	86
3.2.4	Multi-wavelengths Observations . . . . .	90
3.3	GRB091031A and GRB100325A . . . . .	90
3.4	GRB090510 and limits on the lorentz invariance violation . . . . .	92
<b>4</b>	<b>GRB091003</b>	<b>95</b>
4.1	Detections and Light Curves . . . . .	95
4.2	Prompt emission spectral analysis . . . . .	96
4.3	Highest energy photon . . . . .	99
4.4	Simulation study of the High Energy cutoff . . . . .	104
4.5	Extended emission spectral analysis . . . . .	106
4.6	Discussion . . . . .	109
	<b>Conclusions</b>	<b>113</b>
	<b>A Other space telescopes</b>	<b>115</b>
	<b>Acronyms</b>	<b>119</b>

# Introduction

Gamma Ray Bursts are one of the most puzzling source in the universe. Their short time (from few seconds to few minutes) high energy emission, large spectral end temporal variety, and huge distance (up to  $z \sim 8$ ) have made their study complex and interesting. Their analysis are relevant for pure astrophysical reason and also for general relativity test. Some of the astrophysical issue that can be investigated are the characteristics of their host galaxies, stellar evolution and their possible progenitors. The constraint on some physical parameters as the Lorentz Invariance Violations (LIV) can be tested and evaluated only using the distance of cosmic scale of this kind of sources and their short duration. An other important test is the study of the matter properties in highly relativistic jets (the minimum ejecta Lorentz factor is above 1000).

In the first chapter of this thesis the main characteristics of the Gamma ray bursts are highlighted. The usual classification of *Short* and *Long* is illustrated with its limits and properties. In the following sections the theoretical framework usually adopted for the analysis of those sources is schematically described with the various possible progenitors (collapse of huge stars or merging of two stellar objects) and their energy reservoir (rotational or magnetic).

In the second chapter the *Fermi* satellite and its two instruments (the *Large Area Telescope* and *Gamma-ray Burst Monitor*) are described in details with informations about their components and performances evaluated with tests performed on ground and on orbit. In the same chapters the Instrument Response Functions are illustrated and the operating modes of the satellite are shortly indicated. The Gamma-ray bursts Coordinate Network (GCN) system, that allows to share in short time

the informations through all the telescopes, is also described. This system is particularly relevant since the study of this transient sources through the whole electromagnetic spectrum (from radio wave to GeV photons) is the only way to locate and try to understand them. The future possibly of the observations through other kinds of messengers as neutrinos (with ANTARES and ICECUBE) and gravitational wave (with VIRGO, LIGO and in the future LISA) could solve several theoretical issues. In appendix A the Agile and Swift missions are shortly described.

In chapter three several important results obtained with the *Fermi Large Area Telescope* on the Gamma ray bursts science are highlighted with several theoretical interpretations used in literature. The main spectral characteristics are summarized together with the description of some relevant bursts. Particular relevance is given to GRB090902B, that until now, is the burst with the highest number of photons above 100 MeV ever observed. The interpretation of its spectral characteristics is still debated in literature. The observation of the 33 GeV photons 82 seconds after the start of the emission (the highest energy photon ever observed from a Gamma Ray Bursts) has put several constraint on models of the extra galactic background light. In the last section of the third chapter the tight limits that constrain the Lorentz Invariance Violations obtained using GRB090510C are shown.

In the last chapter, the analysis of the prompt phase of GRB091003 with its spectral characteristics are described together with several details of the standard analysis procedure. This analysis, still preliminary, has shown several interesting characteristics and it has similarity with other bursts.

# Chapter 1

## Gamma-ray Bursts

### 1.1 Introduction

In this chapter an introduction will be done to Gamma Ray Burst (GRB) science. In the first section their discovery and early observations will be described, in the second some spectral and temporal characteristics will be highlighted. In the following sections their classification in subgroups, possible central engines and emission mechanism will be described.

### 1.2 Discovery and relevant observations

The GRBs are short-lived (order of seconds) bright flashes of radiation with spectral energy distributions peaking in the  $\gamma$ -ray band, observable in a huge part of the electromagnetic spectrum from the radio frequencies to GeV energies. The GRBs were discovered in the 1967 by the Vela satellites (with CsI scintillators sensible to energies around 1 MeV). For the first time, 16 GRBs were reported in the 1972 [1] and their cosmological origin and correlation with supernovae was already supposed. A partial review of the history of experiments for the observations of GRBs is in [2] and the history of the GRBs discovery is in [3].

Before the launch of the *Compton Gamma Ray Observatory* (CGRO <sup>12</sup> 1991-2000) the study of this kind of sources was strongly impeded by the fact that their distance was completely unknown. On CGRO there were four instruments: the Burst And Transient Source Experiment (BATSE, 20 keV

---

<sup>1</sup><http://heasarc.gsfc.nasa.gov/docs/cgro/index.html>

<sup>2</sup><http://heasarc.gsfc.nasa.gov/docs/cgro/epo/brochures/compton/bro5.html>

-  $\sim 1$  MeV), the Oriented Scintillation Spectrometer Experiment (OSSE 50 keV - 10 MeV), the Imaging Compton Telescope (COMPTEL 1-30 MeV), and the Energetic Gamma Ray Experiment Telescope (EGRET 20 MeV-30 GeV). After few months of data taking the BATSE team reported that the spatial distribution of the first 153 burst was isotropic and it was compatible with object of cosmological origin and no correlation was found with known distribution of galactic objects [4]. There was still the possibility that their sources were really close to the Earth (solar system) or in a large halo around our galaxy.

From the  $\gamma$ -ray part of the spectrum, observed by BATSE and in few cases by EGRET on CGRO, it is impossible to evaluate the distance of the source, but several theories predicted [5] that the interaction of the ejecta with the surrounding cooler matter would cause a long lasting *afterglow* emission at longer wavelength. This was not observed yet because this emission was faint, the existing observatories were too slow to repoint and the localizations in the sky were not enough accurate. The turning point was the launch of Beppo-Sax<sup>3</sup> (1996-2003) an Italian-Dutch satellite for the X-ray astronomy. It was able to observe, for the first time, GRB 970228 [6]<sup>4</sup> and its X-ray afterglow. With this enhanced localization, the on ground telescope were able to observe its optical counterpart. Only two years later, the redshift of the host galaxy of this burst was measured ( $z=0.695$ ) [7], allowing a complete estimate of its energetic outflow. The first redshift determination was done for the next event observed by BeppoSAX, GRB 970508[8]. This event was localized within four hours of its discovery, allowing research teams to begin making observations much sooner than any previous burst. The spectrum of the object revealed a redshift of  $z = 0.835$  [9]. The radio afterglow of this burst was observable for the first time[10], allowing a joint analysis of the spectrum from the radio to X-ray. With this results the cosmological origin of GRBs was almost unanimously accepted.

The satellite HETE-2 [11] launched in October 2000 was an international

---

<sup>3</sup><http://www.asdc.asi.it/bepposax/>

<sup>4</sup>the name of a GRB is the date in which it happens in the format: YYMMDD, if multiple GRBs happen in the same day a letter is appended in the end

satellite mission devoted to the detection and localization of gamma-ray bursts by using 3 wide-field instruments with a total spectral coverage from 2 to 400 keV. Between the years 2000 and 2006 HETE-2 detected several hundreds GRBs and localized 84 of them, with a precision even as low as few arc minutes and a delay even of just one minute[12].

The discoveries in this field are far to be ended, both experimental and theoretical. Lately two GRBs observed by different telescopes and by the *Swift* satellite, see section A, have set important records for object of cosmological origin. The GRB 090423 has a near-infrared spectroscopic measurement redshift of  $z = 8.1_{-0.3}^{+1.1}$  [13] and it was the farthest object ever observed. This burst happened when the Universe was only about 4% of its current age. The analysis of GRBs at such high redshift (several models suggest that we should be able to detect burst up to  $z \sim 20$ ) is fundamental to understand the universe at an early phase (galaxies and star formations). The GRB 080319B, *naked eye GRB*, was the most luminous optical burst ever observed, with a visual magnitude of 5.3 at a redshift of  $z=0.937$  [14]. The *Fermi* satellites discoveries will be discussed and highlighted in the following chapters.

### 1.3 Main Spectral characteristics

GRBs have a complex time structure and their spectra change with time. The first part of the emission, observable up to the GeV energies was the first to be discovered by the Vela satellite (in the MeV range) and it lasts from few milliseconds to few tens of seconds. This part of the emission, known as *prompt phase*, in the BATSE part of the spectrum ( $\sim$  MeV) was usually well described by two smoothly jointed power law. This empirical non thermal function is called *Band function*[15]:

$$f(E) = \begin{cases} A(E)^\alpha e^{-e(2+\alpha)/E_{peak}} & \text{if } E < E_{break} \\ A \left[ \frac{(\alpha-\beta)E_{peak}}{(2+\alpha)} \right]^{\alpha-\beta} \left( \frac{E}{100} \right)^\beta & \text{if } E > E_{break} \end{cases} \quad (1.3.1)$$

where

$$E_{break} \equiv \frac{(\alpha - \beta)}{2 + \alpha} E_{peak} \equiv E_0(\alpha - \beta), \quad (1.3.2)$$

it is the break energy between the two part of the function.  $\alpha$  and  $\beta$  are, respectively, the spectral indices of the low energy an high energy part of the

spectrum. Their value, in the BATSE sample [15] [16] [17], is  $\alpha \sim -1$  and  $\beta \gtrsim -2$ .  $E_{peak}$  is the peak energy in the  $\nu F_\nu \propto E^2 f(E)$  spectrum if  $\beta < -2$ , a study on  $E_{break}$  distribution and theoretical predicted value is in [18]. If  $\beta \geq -2$  the integrated total energy would be infinite unless the spectrum has a high-energy cutoff. The cutoff cannot be detected if it is above the sensible range of the instrument. The Band function in several analysis is used both for the integrated prompt emission and for the spectral analysis of a single part of it.

In the latest BATSE catalogue of bright burst [16] there are also other spectral function commonly used. The Band function is the more promising for a detection above 100 MeV (in the *Fermi Large Area Space Telescope* (LAT) energy range, see chapter 2) if the  $\beta$  is not too hard ( $\sim -2$ ). The prompt part was observed in few cases also at higher energies by EGRET and Agile: the peculiar characteristics of this detection will be discussed later, see section 1.4.

After the *prompt emission*, the GRB *afterglow emission* is observed in the X, Optical and Radio energy band if a quick and accurate localization in the  $\gamma$ -ray is done and there is the possibility of a follow-up observation on ground. The GRB afterglow could be observed for days and week and it is strongly important to understand the GRB environment and its galaxy. In few cases the X-ray afterglow is observable for years as in the case of GRB 060729 still observable by Chandra two years after the prompt phase [19].

The afterglow in the X-ray band observed by *Swift* has shown a canonical behavior. The light curve is broadly composed by three distinct power-law segments [20]. A bright rapid-falling ( $t^{-\alpha}$  where  $\alpha > 3$ ) afterglow immediately after the prompt emission, that lasts for the first few hundreds of seconds, is followed by a steep-to-shallow transition ( $\alpha \sim 0.5$ ), which is usually accompanied by a change in the spectrum power-law index. Probably those two components arise from physically distinct regions and therefore their spectrum would generally be different and the shallow part can be caused by a continuous injection of energy [20]. The shallow phase then evolves to the classical afterglow phase with no clear evidence for a spectral change ( $\alpha \sim 1.3$ ). In some cases a *jet break* is seen at later times and it is a steep ( $\alpha \sim 2$ ) [21] and aromatic decay of the observed flux. A jet

break is supposed to happen when the decrease of the ejecta Lorentz factor, for the interaction with the surrounding materials, leads to the light-cone angle becoming larger than the jet angular extent  $\Gamma \sim \theta_j^{-1}$  [22] (also see the paragraph 1.10). This latest steep decay is clearly observed in only the 12% of *Swift* GRB's while in a further 30% of the dataset there is a possible jet break [21], while the burst without observable break and a well sampled X-ray light curve are still a theoretical open issue. The jet break is a purely geometric effect therefore it should affect all the emitted wavelength (from X-ray to radio) being achromatic.

Even if the description above holds for the main part of the detected GRBs, there are also outliers. 19 afterglows, over more than 400 observed by XRT on *Swift*, are monotonously decaying as a single power law with index  $1 \sim 1.7$  from tens (or hundreds) of seconds to  $10^5$  s after the trigger. This bursts do not seem peculiar with respect to other characteristics in their prompt phase [23]. An analysis [24] of a GRB sample up to 2007 have shown that seven out of the 13 candidates with multi wavelength data suggest a chromatic break at the *jet break* opposite to the expectation from the jet models.

The energy in the afterglow [25] at these late times is estimated to be comparable to or smaller than that in the prompt gamma-ray emission, even when correcting for radiative losses from the afterglow shock at early times, suggesting a high efficiency of the prompt emission. The presence of the shallow decay phase implies that most of the energy in the afterglow shock was either injected at late times after the prompt gamma-ray emission was over, or was originally in slow material (smaller  $\Gamma$  in the late part of the emission) that would not have contributed to the prompt  $\gamma$ -ray emission [20]. In  $\sim 50\%$  of the *Swift* observed X-rays afterglows, multiple flares have been discovered. In few cases the energy released in these flares is similar to the one emitted in the prompt emission in the  $\gamma$ -rays. Their temporal characteristics and energy [26] suggest that these flares are due to the same mechanism responsible for the prompt emission, which is usually attributed to the activity of the central engine, see section 1.7. When X-ray flares are observed, typically no flaring is seen in the optical band by the UV Optical Telescope on *Swift*. Several other informations and references on GRB's

optical and radio afterglow can be found in [25].

## 1.4 High Energies characteristics (before *Fermi*)

Constraints on the origin of the high-energy emission from GRBs were quite limited due to both the small number of bursts with firm high-energy detection and to the small number of events detected in such cases, before the launch of *Fermi*. High-energy emission from GRBs was first observed by EGRET. Emission above 30 MeV was detected in five cases: GRBs 910503, 910601, 930131, 940217, and 940301 [27]. Their sub-MeV emission, as detected by BATSE, has the largest fluence,  $F$ , and peak intensity,  $I$ , of any of the BATSE detected bursts within the EGRET field of view. Even with this small statistics interesting differences have been highlighted in this sample between the high energy and low energy component. One of these sources, GRB 930131, exhibited high-energy emission that was consistent with an extrapolation from its spectrum obtained with BATSE between 25 keV and 4 MeV [28], with no detected change during all the emission. On the contrary, evidence for an additional high-energy component up to 200 MeV with a different temporal behavior to the low-energy component was discovered in GRB 941017 (in EGRET's calorimeter, the Total Absorption Shower Counter) [29]. With COMPTEL data the additional spectral component (a Power Law with spectral index  $\sim -1$ ) was confirmed and its statistical significance was increased [30]. The high-energy emission for this burst lasted more than 200 s. A unique aspect of the high-energy emission in GRB 940217 was its duration, which lasted up to  $\sim 90$  minutes after the BATSE GRB trigger, including an 18 GeV photon at  $\sim 75$  minutes post-trigger [31]. More recently, the GRID instrument on board AGILE, see section A, detected 10 high-energy events with energies up to 300 MeV from GRB 080514B, in coincidence with its lower energy emission, with a significance of  $3.0 \sigma$  [32]. Also this GRB lasts longer in the high energy band than in the low energy one.

## 1.5 GRBs classifications

Unlike other transient events that have a similar time behavior, the light curves of GRBs are really different and complex. The analysis of over 1200 BATSE burst have shown that no two GRBs are similar to within the statistical limits of the data [33]. Given this variability of the light curve characteristics, one of the main topics of the research was to understand if there are some subclasses. From the bimodality of the duration distribution of the GRBs observed by BATSE they are divided in two classes [34] *long burst* (LGRB) and *short burst* (SGRB). If a burst has a  $T_{90}$ <sup>5</sup> [35] shorter than 2 s it is defined *short*, otherwise it is a *long* burst. Within the same sample these two classes showed also another discrimination, the spectral hardness, as determined by the ratio of two broad energy channels [34]. The short bursts seem to be harder than long bursts. In [36] and references therein they suggest that the characteristics spectral hardness of short bursts could be related strictly on the BATSE triggering method; when the GBM catalogue will be made available some of this issues could be resolved.

Another classification scheme uses the scatter plot of the fluence and duration fitted with two two-dimensional Gaussians [37]. Some analysis showed that there is the possibility of a third population in the  $T_{90}$  distribution; this third GRBs sample has an intermediate duration between the two major classes [38]. Another characteristics that is used to discriminate the two classes is the *spectral lag* [39], namely the time differences between the signal in two broad energy band. The measured lag for short burst is from 20 to 40 times shorter than for long bursts, and their lag distribution is symmetric about zero, unlike long bursts [40]. The average lag (25-50 to 100-300 keV) for the 30 brightest BATSE short bursts is  $\sim 0.1 \pm 0.5$  ms, compared to  $\sim 50$  ms for bright long bursts [36]. Many more classification studies have been done using spectral characteristics [41] and the total observed flux [42].

All this kind of classifications suffers various kind of problems: the  $T_{90}$  strongly depends on the energy bands in which it is measured and on the background selection. Nevertheless some short bursts show an extended

---

<sup>5</sup>interval in which the 90% of the photons are detected

emission [36] (EE) up to  $\sim 10$ s in the BATSE range; its detection can extend the  $T_{90}$  of the GRB above the 2 s limits and make it a long burst. This extended emission has a spiky and pulselike look, in contrast with the standard view of GRB's afterglow and sometimes there is a short pause between the first pulse and the extended emission. The EE is typically softer than the main peak and has an intensity ranging from  $10^{-3}$  to  $10^{-1}$  times that of the initial short pulse complex. It is possible that almost the 75% of bursts without currently detected EE have this component with flux levels below detectability, although there are bursts with upper limits on the intensity of a factor below  $10^{-4}$  times that of the short pulse complex [25]. One of the burst detected by EGRET, GRB 930131 had a  $T_{90} = 14$  s measured by BATSE [43] and high-energy ( $> 30$  MeV) photons accompanying the prompt phase and possibly extending beyond [28]. The BATSE light curve is dominated by a hard initial emission lasting 1 s and followed by a smooth extended emission and it could be a short burst with EE, several analysis have been done on this burst for associate this to the short or the long burst class.

Considering only bursts with known redshift (this is not the case of the BATSE sample) in [44] they have evaluated the  $T_{90}$  vs hardness ratio in the source rest frame and some bursts can go from one class to the other one only for the relativistic time and wavelength corrections. Since usually the short bursts are closer to us (smaller  $z$ ) than long bursts, the  $T'_{90} = T_{90}/(1+z)$  distribution in the source reference frame has even more overlap than the one in the observer frame. In the source frame, the typical long-burst duration is  $\sim 20$  s compared to  $\sim 50$  s in the observer frame. Swift has been detecting a lower fraction ( $\sim 10\%$ ) of short bursts than BATSE did (25%). This is because Swift observes in a softer energy band (15–150 keV) than BATSE does (50 keV–2 MeV) and the image part of the trigger algorithm, required by Swift, is less sensitive to short bursts owing to their lower fluences[25]. One of Swift's major successes has been the first position determination and X-ray afterglow of a short GRB [45] giving rief to a systematic study of their host galaxies.

Several studies have shown that *short* and *long* bursts spectral parameters clusterize in different regions of the parameter space. One

relation well known in literature is the *Amati relation* [46] between the peak energy of the Band Function in the source rest frame ( $E'_p$ ) and the total isotropic energy emission ( $E_{iso}$ ), it seems to hold well for long bursts while short GRBs are outliers. Another well known relation that shows the same property is the *Ghirlanda relation* [47] between the  $E'_p$  and the total energy emission in the jet opening angle ( $E_{\gamma,iso}$ ) (for its application on LAT detected long and short bursts, see respectively [48] [49]). While the *Yonetoku relation* [50] between  $E'_p$  and the total isotropic luminosity ( $L_{iso}$ ) seems to hold on both kind of bursts [51]. This relations are still matter of debate in literature.

A different method for the classification of GRBs was proposed and used in [44], they consider all the available different information of each burst in order to distinguish two clean classes. Each of them has a *golden sample* containing few burst with some clearly stated characteristics. The informations used are not anymore only in the gamma-rays range but they tend to use as much information as they can, considering the optical, near infrared and ultraviolet data that lately are becoming available (they have made also a possible decision chart). They suggest that there are two types of GRB:

1. Type I GRBs (or compact star GRBs) are those GRBs that are associated with the theoretical models invoking destructive explosions in old-population, degenerate, compact stars. The likeliest model candidate is the merging of two compact stars (*mergers*).
2. Type II GRBs (or massive star GRBs) are those GRBs that are associated with the theoretical models invoking destructive explosions in young-population massive stars. The likeliest model candidate is a core collapse of massive stars.

## 1.6 Progenitors

Usually the models of possible sources of GRBs follows the dichotomy of short and long bursts, as indicated in the previous scheme. The short bursts are associated with compact merging of neutron star-neutron star (NS-NS)

or black hole-neutron star (BH–NS) binaries models, while the long bursts are associated with *collapsar*, *hypernova* or *millisecond magnetars* models.

### 1.6.1 Observations: long bursts

After the Beppo-Sax detection of GRB 980425, its association with SN 1998bw [52][53] and the first spectroscopically confirmed association of GRB low redshift ( $z = 0.1685$ ) GRB 030329 [54] with SN 2003dh the collapsar model has become in some cases confirmed. Several other associations have been found studying the *bump* in the afterglow of other long low-redshift GRBs [55], where the temporal behavior of standard GRB afterglow is different and usually steeper than SN spectra. The SN signal could be observed a few days after the explosion if it is not absorbed.

On the basis of this association, several analysis and observation in different wavelenght of supernovae, have been done to better constrain this relationship. As burst emission is supposed to be highly beamed, it is possible to detect the roughly isotropic supernovae emission and miss the GRB owing to the jet axis not being aligned with Earth. If this happens, the hydrodynamic evolution of the jet eventually transitions from the relativistic to the non-relativistic regime, when the electromagnetic signal is no longer emitted in a narrow cone. Radio observations could therefore find emerging evidence of a central engine. An extended radio late-time observation of 68 local Type Ibc SN [56], including six events with broad optical absorption lines or hypernovae has shown that none of these objects exhibit radio emission attributable to off-axis gamma-ray burst jets spreading into our line of sight. Using an afterglow model they conclude that less of 10% of Type Ibc supernovae are associated with typical gamma-ray bursts initially directed away from our line of sight. Using the rate of detected SN and GRBs they were able to evaluate limits of LGRBs relativistic jet opening angle compatible with the observed one.

Mildly relativistic type Ibc SN as SN 2009bb [57] and 2007gr [58] (see also the references in it) were also observed in absence of an observed GRB counterpart. The analysis of the emitted energy and jet velocity of the SN 2009bb has shown that it is closer to the distribution of local GRBs than other SN Ibc. For SN 2007gr optical observations indicate a typical type

Ic supernova with ejecta velocities 6,000 km/s, much lower than in GRB-associated supernovae while the radio data indicate higher velocities. They conclude that in SN 2007gr a small fraction of the ejecta produced a low-energy mildly relativistic bipolar radio jet, while the bulk of the ejecta were slower and, as shown by optical spectropolarimetry.

Extensive search for supernovae counterpart of nearby long GRBs have lead to some really low upper limits. GRB 060505 ( $z=0.089$ ) and GRB 060614 ( $z=0.125$ ) [59] were not accompanied by supernova emission down to limits hundreds of times fainter than the archetypal supernova SN 1998bw that accompanied GRB 980425, and fainter than any type Ic supernova ever observed. Multi-band observations of the early afterglows, as well as spectroscopy of the host galaxies, exclude the possibility of significant dust obscuration and show that the bursts originated in actively star-forming regions. The absence of a supernova could suggests a new phenomenological type of massive stellar death.

The progenitor characteristic and age can be understood also with analysis of GRBs host galaxies, from the analysis of the afterglow. From a cosmological point of view, their characteristics can be used also for understand if the stellar evolution follows the theoretical path. Several surveys of long GRBs host galaxies have established some standard characteristics, they are sub- $L^*$  galaxies (median  $L \sim 0.1L^*$  ) with exponential-disk light profiles and high specific star-formation rates ( $SSFR \sim 1Gyr^{-1}$ ) [25] (and reference therein). The analysis of the distribution of long burst position inside the galaxies provides strong observational evidence for the connection of GRBs to star formation regions [60], that is important to understand that they should be related to young and huge stars collapse. At the same time GRB host galaxies seem to be readily distinguished, as luminosity and morphology, from the host galaxies of core-collapse supernovae at similar redshifts [61]. They suggest that the main differences between this two environments is the low-metallicity needed for a GRB to explode, otherwise the envelope of the star is expelled and the remaining mass is not enough for power an high energy explosion.

### 1.6.2 Theoretical models: long bursts

A complete review of observation and theory on SuperNovae (SN) LGRBs connection could be found in [62],[63] and in [22]. A current SN *standard model* [64] begins with the collapse of the iron core of a highly evolved star that had a main sequence mass of over  $10 M_{\odot}$ . The collapse, triggered by electron capture and the partial photodisintegration of the iron at temperatures  $T \sim 10^{10}$  K and densities  $\rho \sim 10^{10} gcm^{-3}$ , continues until the center of the central core exceeds nuclear density by a factor of about two. The rebound, generated by this overshoot and the short range repulsive component of the nuclear force, launches a shock wave, but this *prompt* shock wave quickly loses all its outward velocity owing to photodisintegration and neutrino losses. After  $\sim 0.1$  s the onset of the collapse, a *proto-neutron star* remains at the center of the collapsar. It has a radius of  $\sim 30$  km and a mass  $1.4M_{\odot}$  with a standing accretion shock at  $\sim 150$  km through which matter is falling at about  $0.1 - 0.3M_{\odot}s^{-1}$ . In the next seconds a neutrino flux cools the surrounding materials and can expell a great part of it, enough to create a SN and similarly a GRB, see also section 1.7. A full description can be found in [65]. Several simulation in 2D and 3D have been done of this model, showing several difficulties and characteristics [66].

Since the energetic outflow of known SN are usually smaller than SN associated with GRBs, in literature the term *Hypernovae* [67] [68] (HN) is used. HN are really huge energetic explosion of massive stars composed mainly of carbon and oxygen (having lost its hydrogen and helium envelopes as the Ic type SN [69]). For the GRB980425 the main sequence original star had a mass of  $40 M_{\odot}$  [67] leaving a remnant of  $M_{rem} \sim 2.9M_{\odot}$  and emitting  $E_{exp} = 3 \times 10^{52}$  erg. The  $M_{res}$  exceeds the upper mass limit for a stable neutron star, suggesting the formation of a black hole.

A SNe with associated GRB should create, far away from the progenitor star, focused jets with at least 200 times as much energy in motion and fields as in rest mass. The jet typically must have an opening angle  $\sim 0.1$  radiant or wider and a power  $\sim 10^{50}$  erg/s, see section 1.9. In some cases the energy budget needed for really huge GRBs, as the ones detected by the *Fermi Large Area Telescope* (LAT,see chapter 2), can go up to  $10^{53}$  erg if

the emission is isotropic and to  $10^{51}$  if it is highly collimated. To produce SNe like SN 2003dh and SN 1998bw the model must deliver  $10^{52}$  erg of kinetic energy within a much larger solid angle ( $\sim 1$  radian), in addition to the collimated outflow. This is at least 10 times more than an ordinary SN. This high energy budget strongly limits the models for the central engine.

The *collapsar model* creates a jet for at least 10s [70]; if the duration of short-hard bursts ( $\sim 0.3$ s) reflects the activity of a central engine, the energy source for short-hard bursts and long-soft ones cannot be the same one and the short should be originated in another way. This problem could be solved in some particular cases where the observed emission is not strongly relativistic and the GRB jet is observed at a large angle (misaligned GRB); under this circumstances a short burst could be created in a *collapsar model* [71].

An alternative central engine is the *millisecond magnetars* [72], where the GRB is caused by a purely electromagnetic explosion. The source for GRBs is the rotation of a highly magnetized neutron star with an initial period of about one millisecond, it is rotating near breakup. For a rotational velocity  $\Omega \sim 5000 \text{rads}^{-1}$  and a dynamo-generated magnetic field,  $B \sim 2 \times 10^{15}$  G, the rotational energy is  $E \sim 10^{52}$  erg. The strength of these models is that they relate GRBs to the birth of an object known as, the magnetar, at energy scale that is about right for a neutron star rotating near break up. Soft Gamma-ray Repeaters (SGRs) and anomalous X-ray pulsars are known to be magnetars [73], whose X-ray emission is powered by the very strong magnetic field. SGRs occasionally become *active*, producing many short X-ray bursts. Very seldom, an SGR emits a giant flare with a total energy about a thousand times higher than in a typical burst. This events have a smaller energy release than that of a standard GRB but the emission mechanism could be similar. As proposed in [73] they could be also source of some of short GRBs. The fields required are large ( $\sim 10^{15}$  G), but no larger than in other models. A possible evidence for this kind of source is a very steep decay in the X-ray afterglow flux, as in GRB 070110 [74], where the authors propose that the observed X-ray plateau is powered by a spinning-down central engine, possibly a millisecond pulsar, which dissipates energy inside an internal radius before depositing energy into the external shock.

As noticed in [62], however, these models ignore the accretion,  $\sim 0.1M_{\odot}s^{-1}$ , that occurs onto the proto-neutron star for several seconds before it contracts to its final radius and develops its full rotation rate. This accretion must be reversed before the neutron star becomes a black hole. In [75] the proto-magnetar could be both accompanied or not by a SN and in both cases a neutrino-powered explosion can stop the matter falling. The major limits to the magnetar scenario are the total energy collimated outflow  $\sim 10^{52}$  erg and the duration of the prompt phase  $> 200$ s [75] up to several ks, both are stressed by some analysis of *Fermi* observed GRBs. Gamma ray (0.1-10 GeV) emission from known galactic magnetars was searched in the 17 months data of *Fermi* LAT, but no significant evidence was found [205].

### 1.6.3 Theoretical models and observation: short bursts

The possible central engine of short burst was less known since the first localization of a short burst [76] GRB 050509b observed by the Swift satellite. This allowed for the first time the study of the host galaxy, giving the distance of the explosion from the galaxy center and the absence of an associated Supernovae. A detailed comparison of the galaxies hosting short bursts [77] and long GRBs shows systematically higher luminosities, lower specific star formation rates, and higher metallicities. The probability that they belong to the same populations of galaxies is  $10^{-3}$ . Short GRB hosts appear to be drawn uniformly from the underlying field galaxy distribution, indicating that the progenitors have a wide age distribution of several Gyr. The lack of association with star forming regions disfavors the collapsar origin of short burst.

The current view [65] (and reference there in) is that short burst arise in a very small fraction ( $\sim 10^{-6}$ ) of stars which undergo a catastrophic energy release event at the end of their evolution in old systems. One conventional possibility is the coalescence of binary Neutron Stars (NSs). Double NS binaries can eventually coalesce due to angular momentum and energy losses to gravitational radiation. The resulting system could be above the mass limit to survive as a single NS and a BH would be unable to swallow the large amount of angular momentum present. The expected outcome would then be a spinning hole, orbited by a torus of NS debris. Other types of

progenitor have been suggested in literature [65]: Neutron Star-Black Hole merger where the NS is tidally disrupted before being swallowed by the hole; the merger of a White Dwarf (WD) with a BH; the coalescence of binary WDs; or accretion induced collapse (AIC) of a NS, where the collapsing NS has too much angular momentum to collapse quietly into a BH. In an alternative class of models, it is supposed that the compact objects are contained within a Galaxy Clusters, and that the binary system will evolve mainly through hardening of the binary through three-body interactions or physical star–star collisions rather than by pure gravitational wave emission. All this models could be tested using the relative frequencies in the galaxies, energetic budget, redshift distribution and also location in the host galaxies itself, since the SN explosion of one or both the star can create a kick and move far from its original location the system [78].

The authors of [79] have shown that all short burst with EE lie very close to their hosts. They suggest that neutron star-black hole binary mergers offer a natural explanation for the properties of this extended-duration/low-offset group. While short burst with large offsets have no observed EE and are less likely to have an optically detected afterglow properties consistent with neutron star-neutron star binary mergers occurring in low-density environments. The first comprehensive survey [80] with the *Hubble Space Telescope* (HST) of 10 short GRB host galaxies has shown that: 1) the host have exponential disk profiles, characteristic of late type galaxies and that are larger than the hosts of LGRBs; 2) the distribution of projected physical offsets (GRB-host center) has a median of  $\approx 5$  kpc, about five times larger than that for long GRBs; 3) short burst are concentrated in less bright region of the host galaxies than long GRB. With these results, the authors conclude that short GRBs are consistent with a progenitor population of NS–NS binaries. They have not found no convincing evidence that short GRBs with extended emission have smaller physical offsets than those without extended emission. Both this analysis rely still on small samples of observed burst and their results will be confirmed in the next years.

The absence of a clear host associations for several short burst has lead to different interpretation, for example that several of them have a redshift around 3 and the galaxies are too faint to be observed or that the GRBs are

far  $\gtrsim 15kpc$  from nearby galaxies ( $z \lesssim 1$ ) [81] for the natal kick.

GRB 070429B[82] is the short burst with the highest redshift ( $z \sim 0.9$ ) ever recorded (a similar value is observed for GRB090510 [83]). This means that it occurred when the Universe was about 40% of its present age, shortly after the time when most stars were being assembled in galaxies. This dramatically moves back the time (the previous highest redshift was  $\sim 0.5$ ) where we know that short bursts were being formed and it could suggest that the present evidence for an old progenitor population may be observationally biased. A review of short burst progenitor and its evolution with a graphical representation of a possible evolutionary path is in [84] and in [65].

## 1.7 Central Engine

In the following section a schematic overview of the central engine is done. It is pretty similar for both classes.

The gravitational energy liberated in the collapse or merger involves the order of a few solar masses, which is converted into free energy on timescales of milliseconds inside a volume of the order of tens of kilometers cubed [22] [85]. This prompt energy is then increased by a comparable amount of energy release in a similar or slightly larger volume over a longer timescale from a few seconds to hundreds of seconds, by the continued infall or accretion of gas from the orbiting torus of debris onto the central object.

A really efficient converter is needed to make free the observed GRBs energy budget. The deeper the gas can fall into the potential well before the radiation is converted, the more efficient is the process, hence the appealing nature of compact objects. For BHs approximately  $\sim GM/R_{ms} \sim 0.1c^2 \equiv 10^{20}ergg^{-1}$  (where  $R_{ms}$  is the radius of the marginally stable orbit) can be released, and even more if the hole is endowed with a large angular momentum. This efficiency is over a hundred times that traditionally associated with thermonuclear reactions (hydrogen burning releases  $0.007c^2 \sim 6 \times 10^{18}ergg^{-1}$ ) [65].

The principal result of the sudden release of this large gravitational energy in this compact volume is the conversion of a fraction of that energy into neutrinos, initially in thermal equilibrium, and gravitational waves

(which are not in thermal equilibrium), while a significantly smaller fraction of energy ( $10^{-2} - 10^{-3}$ ) goes into a high temperature *fireball* ( $kT \gtrsim \text{MeV}$ ) consisting of  $e^\pm$ , photons and baryons. The fireball is transparent to the gravitational waves and, beyond several interaction lengths, also to the neutrinos. In this phase a considerable part of the energy budget (several  $\times 10^{53}$  ergs) is emitted in gravitational waves and thermal neutrinos ( $\nu_e \bar{\nu}_e$ ), both this component are not detected yet. A smaller fraction of the free energy ( $10^{50} - 10^{52}$  ergs), remains trapped inside the fireball, which can also contain a comparable (or in some scenarios a larger) amount of magnetic field energy. This amount of energy is observed, mainly as non-thermal gamma-rays and it is more intense than any other explosive event in the universe. The total energy released is comparable to the electromagnetic and kinetic energy of SuperNovae, but it is emitted in few seconds in  $\gamma$ -rays instead than in months mainly in optical wavelength.

The accretion of black holes is usually thought to be limited by the self-regulatory balance between Newtonian gravity and radiation pressure. A fiducial luminosity is the *Eddington limit* associated with quasi-spherical accretion, at which radiation pressure balances gravity. If Thomson scattering provides the main opacity and the relevant material is fully ionized hydrogen, then this luminosity is:

$$L_{Edd} = \frac{4\pi GMcm_p}{\sigma_T} = 1.3 \times 10^{38} \left( \frac{M}{M_\odot} \right) \text{ergs}^{-1}. \quad (1.7.1)$$

For GRBs the photon luminosities is several order of magnitudes larger than this limits [65]. In this case the Eddington photon limit is circumvented if the main cooling agent is emission of neutrinos rather than electromagnetic waves. The associated interaction cross-section is then many orders of magnitude smaller, and the allowed accretion rates and luminosities are correspondingly higher. Using the cross-section for neutrino pair production (the estimates vary little when one considers, for example, coherent scattering of neutrinos by nuclei and/or free nucleons (except for the energy scaling) [25]), the Eddington limit can be rewritten as:

$$L_{Edd,\nu} = 8 \times 10^{53} \left( \frac{E_\nu}{50 \text{MeV}} \right)^{-2} \left( \frac{M}{M_\odot} \right) \text{ergs}^{-1}, \quad (1.7.2)$$

with an associated accretion rate, assuming unit efficiency for conversion of mass into neutrino energy

$$\dot{M}_{Edd,\nu} = 0.4 \left( \frac{M}{M_\odot} \right) \left( \frac{E_\nu}{50 \text{ MeV}} \right)^{-2} M_\odot s^{-1}, \quad (1.7.3)$$

if the efficiency is different than 1, the accretion rate becomes  $\dot{M}_{Edd,\nu} \times (\text{efficiency})^{-1}$ . The time it would take an object to radiate away its entire rest-mass energy in this way is a mass-independent Eddington time given by

$$t_{Edd,\nu} = \frac{M}{\dot{M}_{Edd,\nu}} \sim 2.5 \left( \frac{E_\nu}{50 \text{ MeV}} \right)^2 s \quad (1.7.4)$$

while the timescale over which an accretion-driven source would double its mass is  $\sim (L/L_{Edd,\nu})^{-1} \times (\text{efficiency})^{-1} \times t_{Edd,\nu}$ . The dynamical time ( $t_{\text{dynamical}}$ ) scales near BHs are modest multiples of  $R_g/c$ , where  $R_g$  is the characteristic size of the collapsed object (and half of the Schwarzschild radius):

$$R_g = \frac{GM}{c^2} \sim 1.5 \times 10^5 \left( \frac{M}{M_\odot} \right) \text{ cm}, \quad (1.7.5)$$

and are therefore much shorter than  $t_{Edd,\nu}$ . A fiducial Eddington density, characteristic near the horizon when the hole accretes at the Eddington rate, is:

$$\rho_{Edd,\nu} = \frac{\dot{M}_{Edd,\nu}}{4\pi R_g^2 c} \sim 10^{11} \left( \frac{M}{M_\odot} \right)^{-1} \left( \frac{E_\nu}{50 \text{ MeV}} \right)^{-2} \text{ g cm}^{-3}. \quad (1.7.6)$$

The typical Thomson optical depth under these conditions is  $\tau_T \sim 10^{16}$  and so photons are unable to leave the fireball and constitute part of the fluid. The Eddington temperature is defined as the black body temperature if a luminosity  $L_{Edd,\nu}$  emerges from a sphere of radius  $R_g$ :

$$T_{Edd,\nu} = \left( \frac{L_{Edd,\nu}}{4\pi R_g^2 \sigma_{SB}} \right)^{\frac{1}{4}} \sim 5 \times 10^{11} \left( \frac{M}{M_\odot} \right)^{-\frac{1}{4}} \left( \frac{E_\nu}{50 \text{ MeV}} \right)^{-\frac{1}{2}} \text{ K}, \quad (1.7.7)$$

or

$$kT_{Edd,\nu} \sim 45 \left( \frac{M}{M_\odot} \right)^{-\frac{1}{4}} \left( \frac{E_\nu}{50 \text{ MeV}} \right)^{-\frac{1}{2}} \text{ MeV}. \quad (1.7.8)$$

The characteristic Eddington magnetic field strength is that for which  $B_{Edd,\nu}^2/8\pi = n_{Edd,\nu} m_p c^2$ :

$$B_{Edd,\nu} = \left( \frac{L_{Edd,\nu}}{R_g^2 c} \right)^{\frac{1}{2}} \sim 3 \times 10^{16} \left( \frac{M}{M_\odot} \right)^{\frac{11}{2}} \left( \frac{E_\nu}{50 \text{ MeV}} \right)^{-1} \text{ G}. \quad (1.7.9)$$

Finally, for comparison,  $T_{th}$  is the temperature the accreted material would reach if its gravitational potential energy were turned entirely into thermal energy:

$$T_{th} = \frac{GMm_p}{3kR_g} \sim 3 \times 10^{12} K, \quad (1.7.10)$$

the radiation temperature is expected to be  $< T_{th}$ . In deriving the above estimates we have assumed that the radiating material can be characterized by a single temperature. This may not apply, for example, when a hot corona deforms the neutrino spectrum away from that of a cooler thermal emitter [65][86]. Similar fiducial values are obtained if the remnant star is a NS, instead of a black hole. In this regime the photons are trapped inside the fireball while the main cooling system is through the neutrino flux and any neutrinos that emerge directly from the central core would have energies of a few MeV. Note that,  $T_{Edd,\nu}$  is below  $T_{th}$ .

## 1.8 Accretion Flows

The progenitors shortly described in the previous sections leave just before the GRB emission a BH or a NS and a surrounding torus. The binding energy of the orbiting debris, and the spin energy of the BH are the two main reservoirs for the case of a BH central engine: up to 42% of the rest mass energy of the torus, and 29% of the rest-mass energy of the BH itself can be extracted for a maximal BH spin[65]. A possible third energetic reservoir is the magnetic energy stored during the collapse.

If the debris have no angular momentum and the magnetic field is dynamically unimportant, there will be essentially radial inflow. Spherical accretion onto BHs is relatively inefficient despite the deep potential well, because the gas is compressed, but not shocked, and thus cannot easily convert gravitational to thermal energy. The flow pattern changes dramatically if the inflowing gas has a small amount of angular momentum. The quasi-spherical approximation breaks down when the gas reaches a radius  $R_{circ} \sim \frac{l^2}{GM}$ , where  $l$  is the angular momentum per unit mass, and if injection occurs more or less isotropically at large radii, an accretion disk will form. The inner regions of disks with mass fluxes  $\leq \dot{M}_{Edd,\nu}$  are generally able to cool by emitting neutrinos on timescales shorter than the inflow time.

The remaining relevant parameter, related to the angular momentum of the system, is the ratio  $v_{inflow}/v_{freefall}$ , where  $v_{freefall} = (2GM/R)^{1/2}$  is the free fall velocity. The inward drift speed  $v_{inflow}$  would be of order  $v_{freefall}$  for supersonic radial accretion. When angular momentum is important, this ratio depends on the mechanism for its transport through the disk, which is related to the effective shear viscosity. This parameter is connected to the dynamical and magnetical characteristics of the accretion disc.

The emitted neutrino luminosity emitted when disk material accretes on a time scale  $t \sim 1$  s is roughly:

$$L_{\nu} \sim 2 \times 10^{52} \left( \frac{M_{disk}}{0.1M_{\odot}} \right) \left( \frac{\Delta t}{1s} \right) \text{ergs}^{-1} \quad (1.8.1)$$

for a canonical radiation efficiency of 0.1. The flow pattern when accretion occurs would be then determined by the value of the ratio  $L_{\nu}/L_{Edd,\nu}$ . The previous parameter determine the importance of radiation pressure and gravity, and the ratio  $t_{cool}/t_{dynamical}$ , which fixes the temperature if a stationary flow pattern is set up, where  $t_{cool} \sim E_{int}/L_{\nu}$ .

## 1.9 Jet production

Since the observed GRBs energy budget can be really high (up to several  $\times 10^{52} \text{erg}$ , see following chapters on *Fermi* detected bursts) and several jet breaks have been observed, it is comonly accepted that the GRBs outflow is in relativistic Jets. The preceding general scheme of neutrino-cooled accretion flows thus provides a power output from the flow of accreting gas but a self-consistent model incorporating outflow and inflow must explain why some fraction of the matter can acquire a really high share of the total energy (i.e., a high enthalpy). Several models are being studied and applied, the two more comon mechanism involves the neutrino flux recombination [87] [88] and the magnetic field with the Blandford–Znajek [89] mechanism. The first one consist in the reconversion of part of the energy emitted through neutrinos (equation 1.8.1) via collisions outside the disk into electron-positron pairs or photons. If this occurs in a region of low baryon density (e.g. along the rotation axis, away from the equatorial plane of the disk) a relativistic pair-dominated wind can be produced. A

requirement for this mechanism to be efficient is that the neutrinos escape from the core in a time scale shorter than that of the matter infall into the BH. The efficiency for conversion into pairs (scaling with the square of the neutrino density) is too low if the neutrino production is too gradual, so this can become a delicate balancing act. Typical estimates suggest a lower bound of  $L_{\nu\bar{\nu}} \sim 10^{-3}L_\nu$  when the entire surface area emits close to a single temperature black-body.

If the jet is emitted electromagnetically the problem of efficiency could be reduced. The potential difference across a disk threaded by open magnetic field lines can exceed  $10^{22}$  V, and this is available for accelerating high-energy particles, which will produce an electron-positron cascade and ultimately a relativistic jet that carries away the binding energy of the accreting gas [89]. A more realistic magnetohydrodynamics (MHD) description of this mechanism is more likely to be appropriate [90] [91].

A MHD wind carries both bulk kinetic energy and ordered Poynting flux, and it is possible that gamma-ray production occurs mainly at large distances from the source. A rapidly rotating NS (or accretion disk) releases energy via magnetic torques at a rate:

$$L_{em} \sim 10^{49} \left( \frac{B}{10^{15}G} \right)^2 \left( \frac{P}{10^{-3}s} \right)^{-4} \left( \frac{R}{10km} \right)^6 \text{ ergs}^{-1} \quad (1.9.1)$$

where P is the spin period, and B is the strength of the poloidal field at a radius R. The last stable orbit for a Schwarzschild hole lies at a coordinate distance  $R = 6R_g = 9(M/M_\odot)$  km, to be compared with  $R_g = 3/2(M/M_\odot)$  km for an extremal Kerr hole. The magnetic field required to produce  $L_{em} \geq 10^{51} \text{ ergs}^{-1}$  (and even higher for LAT detected bursts) is huge, but several realistic solutions for its creation are present in literature [92] and [65]. However, it only takes a residual torus (or even a cold disk) of  $10^{-3}M_\odot$  to confine a field of  $10^{15}$  G.

A serious limitation for this relativistic outflows can be the amount of entrained baryonic mass from the surrounding medium. For instance, a Poynting flux of  $10^{52}$  erg could not accelerate an outflow to Lorentz Factor  $\Gamma \gtrsim 100$  if it had to move more than  $\sim 10^{-5}M_\odot$  of baryons with it. The detection of GeV photons and the latest evaluation of really high Lorentz factor for *Fermi* bursts (above 1000), put even tighter constraints on this,

and more information are in the following chapters. Another complication to relativistic jet formation is that the high neutrino fluxes are capable of ablating baryonic material from the surface of the disk at a rate:

$$\dot{M}_\eta \sim 5 \times 10^{-4} \left( \frac{L_\nu}{10^{52} \text{ergs}^{-1}} \right)^{\frac{5}{3}} M_\odot \text{s}^{-1}. \quad (1.9.2)$$

Thus a rest mass flux  $\dot{M}_\eta$  limits the bulk Lorentz factor of the wind to  $\Gamma_{eta} = L_{wind}/\dot{M}_\eta c^2$  [93]. Assuming that the external poloidal field strength is limited by the vigour of the convective motions, the spin-down luminosity scales with neutrino flux as  $L_{wind} \approx L_{em} \propto B^2 \propto v_{con}^2 \propto L_\nu^{\frac{2}{3}}$ , where  $v_{con}$  is the convective velocity. The ablation rate given in equation 1.9.2 then indicates that the limiting bulk Lorentz factor  $\Gamma_{eta}$  of the wind decreases as  $L_\nu^{-1}$ . Thus the burst luminosity emitted by a magnetized neutrino cooled disk may be self-limiting. Mass loss could, however, be suppressed if the relativistic wind were somehow collimated into a jet. This suggests that centrifugally driven mass loss will be heaviest in the outer parts of the disk, and that a detectable burst may be emitted only within a relatively small solid angle centred on the rotation axis.

Another big theoretical issue is the stability and collimation of the jet when it pass through the circumbust medium. It is still matter of debate if in case of huge star collapse the jet can be created inside the stellar envelope or outside, and if jet remains highly relativistic even if the environment is not so much baryon depleted. Probably if the stellar envelope is too extended only TeV neutrinos can escape accelerated through the Fermi mechanism and gravitational waves. The sensibility of existing neutrino telescopes is approaching the attended flux from GRBs [94]. More reference on jet propagation can be found in [25].

## 1.10 Prompt emission model

### 1.10.1 Fireball expansion and shocks

The expanding fireball as described above is originally optically thin and during the expansion there is a decrease of the internal energy per particle that is balanced by an increase in the expansion-related energy. The  $\Gamma$  Lorents factor of the ejecta increases linearly ( $\propto r$ ) up to the initial value of

random internal energy per particle,  $\gamma_0 = \eta E_0 / M_0 c^2$ . The maximum  $\Gamma_{max}$  is reached at a *saturation radius*  $r_s$ . At this radius the main part of the  $e^\pm$  pairs are already recombined (at a comoving temperature of  $T' \sim 17\text{keV}$ ), but the scattering optical depth is still large at this radius, due to the electrons associated with baryons. Usually this phase is better described with a continuous environment of mini-shells, each at a different radius and with different optical behaviour. The photosphere is the surface where the optical depth is around 1 and above that the fireball became optically thin and the photons can be emitted freely, for a complete evaluation of those values see [22] and reference therein.

The spectrum of the photosphere would be expected to be a black body and be characterized only by the temperature of the surface, modified by comptonization at the higher energy. However, the observed  $\gamma$ -ray spectrum observed is generally a Band function or a broken power law and so highly non-thermal (recent analysis have shown that through multiple collision a Band function could be also obtained from photosphere emission [95]). An exception is the prompt spectrum of GRB090902B, see paragraph 3.2, that was interpreted as a multicolor black body with an additive non-thermal powerlaw [206].

In addition, another problem is that the expansion would lead to a conversion of internal energy into kinetic energy of expansion, therefore even after the fireball becomes optically thin, it would be highly inefficient, with most of the energy released in the kinetic energy of the associated protons, rather than in photons. The most natural way to obtain this kind of spectra in an energetically efficient manner is to have the kinetic energy of the flow re-converted into random energy via shocks, after the flow has become optically thin. Such shocks will be collisionless (mediated by chaotic electric and magnetic fields rather than by binary particle interactions), as known for other kind of cosmological sources as Active Galactic Nuclei (AGN). These shocks can be expected to accelerate particles via the Fermi process to ultra-relativistic energies [22][96] and the relativistic electron component can produce non-thermal radiation via the synchrotron and Inverse Compton (IC) processes, this mechanism are expected to generate the GeV tail that is observed by *Fermi* LAT.

A shock is essentially unavoidable as the fireball runs into the external medium, producing a blast wave. The external medium may be the interstellar medium (ISM) or the pre-ejected stellar wind from the progenitor before the collapse. The characteristics of *external shocks* emission are due mostly to the medium that the ejecta finds on its way, and the lightcurve can be spiky if the external medium is extremely lumpy; this is usually associated with the afterglow emission (from X-rays to radio wave) but is lately used also for explain the prompt phase and its extended emission [97].

Before the jet interacts with the external matter (and it reaches its characteristic radius  $r_{es}$ ), *internal shocks* can also occur as faster portions of the ejecta overtake slower ones, leading to pp collisions and  $\pi^0$  decay  $\gamma$ rays, giving rise to fast variability in the emission. This temporal variability should reflect the variability of the central engine, which might be expected, from accretion disc intermittency and flares. The radiation from the disc or flares, however, cannot be observed directly, since it occurs well below the scattering photosphere of the outflow and the variability of the photons below it is washed out. Ejecta with different Lorentz factor (and energy) can catch up at a  $r_{is}$  above the photosphere and the saturation radius and emit the high energy photons. The internal shock models have the advantage to allow an arbitrarily complicated light curve, with the shortest variation timescale  $t_{v,min} \geq 10^{-4}$  s being limited only by the dynamic timescale where the energy input may be expected to vary chaotically, while the total duration is  $t_{grb} \gg t_v$ . The gamma-ray emission of GRB from internal shocks radiating via a synchrotron and/or inverse Compton mechanism reproduces the general features of the gamma-ray observations. Issues arise with the radiation efficiency, which is estimated to be moderate for internal shocks, but it can increase if the shells have widely differing Lorentz factors, although in this case one might expect large variations in the spectral peak energy  $E_{peak}$  between spikes in the same burst. The efficiency for emitting in the BATSE range is typically low  $\sim 1 - 5\%$ , both when the MeV break is due to synchrotron and when it is due to inverse Compton [22]. Usually in the afterglow also *reverse shocks* are considered, they are generated when the jet expand in the external medium, if the density of medium is enough and it goes backward.

### 1.10.2 Synchrotron shock model

Scattering of electrons (and protons) by magnetic irregularities upstream and downstream can lead to a Fermi acceleration process resulting in a relativistic power law distribution of energies  $N(\gamma) \propto \gamma^{-p}$  with  $p \geq 2$ . This mechanism is applied in several physical field, but the conditions in this kind of environment can modify the spectra. The electrons (and also protons) are accelerated through this mechanism and they gain also energy from the protons through collisionless interaction[22]. The observer frame synchrotron spectral peak is:

$$\nu_m \sim \Gamma(3/8\pi)(eB'/m_e c)\gamma_m^2 \sim 2 \times 10^6 B' \gamma_m^2 Hz, \quad (1.10.1)$$

where  $\gamma_m$  is the initial minimum electron random comoving Lorentz factor and  $B'$  is the magnetic field in the shock. The optically thin synchrotron spectrum is [98]:

$$F_\nu \propto \begin{cases} \nu^{\frac{1}{3}} & \text{for } \nu > \nu_m, \\ \nu^{-\frac{(p-1)}{2}} & \text{for } \nu < \nu_m, \end{cases} \quad (1.10.2)$$

assuming that the radiative losses are small (adiabatic regime). For the prompt emission, the high energy slope  $\beta_2 = (p - 1)/2$  is close to the mean high energy slope of the band fit (Band  $\beta = -(\beta_2 + 1) = -(p + 1)/2 \lesssim -3/2$ ), while the lower energy slope can easily approach  $\beta_1 \sim 0$  (Band  $\alpha \sim -1$ ) considering observations from, for example, a range of  $B'$  values. The basic synchrotron spectrum is modified at low energies by synchrotron self-absorption, where it makes the spectrum steeper ( $F_\nu \sim \nu^2$  for an absorption frequency  $\nu_a < \nu_m$ ). This synchrotron model can explain  $\sim 2/3$  of the sample of the spectra in the 10 keV - 1 MeV [99]. The high energy part of the spectrum is modified at high energies due to inverse Compton (IC) scattering of thermal photons and Synchrotron Self Compton (SSC) effects, that can extend the spectrum into the GeV range.



## Chapter 2

# Apparatus description

### 2.1 Introduction

The *Fermi Gamma-Ray Space telescope*, formerly the *Gamma-ray Large Area Space Telescope* (GLAST) [100], was launched by NASA on 2008 June 11 on a Delta II Heavy launch vehicle from Cape Canaveral at an orbital height of 565 km. Fermi consists of two experiments the *Large Area Telescope* (LAT) [101] and the *Gamma-Ray Burst Monitor* (GBM) [102]. In this chapter the main characteristics and performances of these two experiments will be highlighted, followed by some informations on their calibrations and the descriptions of some flight mode of the satellite useful for GRBs observations. Other satellites that are often used in cooperation with the Fermi data are shortly described in the Appendix A.

### 2.2 LAT overview

The LAT is the main experiment on board *Fermi* and by measuring the tracks of the electron ( $e^-$ ) and the positron ( $e^+$ ). These are produced when an incident  $\gamma$ -ray undergoes pair-conversion, preferentially in a thin, high- $Z$  foil, and it allows the measurement of the energy of the  $\gamma$ , by means of the subsequent electromagnetic shower. For a correct evaluation of the energy and direction of the incident photon and a good rejection of the background due to incident charge particles, the LAT is composed by some sub detectors placed as in Fig 2.1, where a candidate  $\gamma$  event and its couple of  $e^\pm$  are represented.

The LAT is composed by a precision converter-tracker (section 2.4),

and calorimeter (section 2.5), each consisting of a  $4 \times 4$  array of 16 modules supported by a low-mass aluminum grid structure. A segmented anticoincidence detector (ACD, section 2.3), covers the tracker array, and a programmable trigger and data acquisition system (DAQ, section 2.6), utilizes prompt signals available from the tracker, calorimeter, and ACD subsystems to form a trigger. To minimize the chance of light leaks due to penetrations by micrometeoroids and space debris of the light-tight wrapping, the ACD is completely surrounded by a low-mass thermal-blanket micrometeoroid shield ( $0.39 \text{ g cm}^{-2}$ , in yellow in Fig. 2.1). The overall aspect ratio of the LAT tracker (height/width) is 0.4, allowing a large Field of View, see Paragraph 2.9, and ensuring that nearly all pair-conversion events initiated in the tracker will pass into the calorimeter for energy measurement.

This experiment was studied and produced to improve the results obtained previously by the EGRET telescope [103] on board of the *Compton Gamma-Ray Observatory* (CGRO). All of the LAT instrument subsystems utilize technologies that do not use consumables such as gas, allowing a very stable response, see paragraph 2.9, and a longer operational life than its predecessor. In addition, the choice of silicon-strip detector technologies for the LAT design allows the self-triggering of the tracker. The sensitivity of the LAT is at least an order of magnitude greater than EGRET, and unlike EGRET the LAT observes the entire sky several times per day, allowing much deeper monitoring and study of the dynamic high-energy sky.

From the outset, the LAT design included a modular  $4 \times 4$  array of identical trackers and calorimeters. This is partially dictated by the quantized nature of the silicon strip detectors and electronics of the tracker, but also because the modular design had desirable properties relative to a monolithic instrument:

- Modular design provides redundancy and soft failure modes;
- Construction and test are more manageable with potential to reduce costs and schedule risk;
- Early prototyping and performance tests can be performed on detector modules that are full-scale relevant to flight;

- Module size is a good match with relatively localized event signatures for triggering a large-area instrument.

It was crucial to demonstrate that internal dead areas associated with support material and gaps between towers were not a problem.

Before the launch a calibration unit, built from spare flight module and flight-like electronic module was tested between July and November 2006 at CERN and GSI. The result were compared with the Monte Carlo data finding an overall agreement. The whole preliminary report could be found in [104] and [105]. Several more informations on the calibration on ground and on board could be found here [106] and for the onboard calibration of the whole telescope in [207].

Upon triggering, the DAQ initiates the read out of the three subsystems, tracker , calorimeter and ACD and utilizes onboard event processing to reduce the rate of events transmitted to the ground to a rate compatible with the 1 Mb/s average downlink available to the LAT. The onboard processing is optimized for rejecting events triggered by cosmic-ray background particles while maximizing the number of events triggered by  $\gamma$ -rays, which are transmitted to the ground. Heat produced by the tracker, calorimeter, and DAQ electronics is transferred to radiators through heat pipes in the grid. Each operational mode and reboot has to keep the temperature almost stable for not damage any part of each subsystem. Several temperature studies were done, during the first part of the mission and during the few reboot of the LAT, for ensure the temperature stability of the subsystems.

## 2.3 ACD

The ACD is LAT first-level discrimination between the charged cosmic ray background and the  $\gamma$ -rays. The photons are outnumbered by 3-5 orders of magnitude by the charged particle. The ACD covers the top and four sides of the LAT tracker, requiring a total active area of  $\sim 8.3m^2$ . The ACD detector utilizes plastic scintillator tiles with wavelength shifting fiber readout. This provides uniformity of light collection (that is required to be within 10% of its average value, excluding the tile edge area) over each detector segment, and allows the two redundant photomultiplier tubes (PMTs), for each, to be

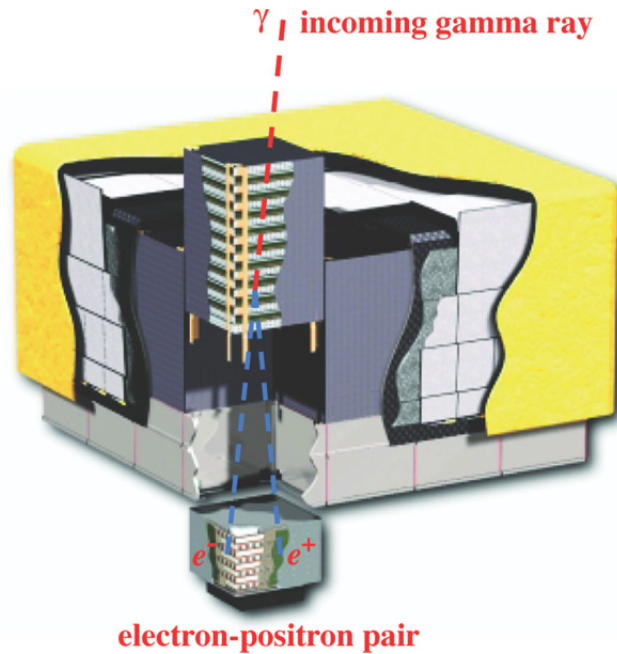


**Figure 2.1:** Schematic diagram of the LAT. The telescope's dimensions are  $1.8\text{ m} \times 1.8\text{ m} \times 0.72\text{ m}$ . The power required and the mass are  $650\text{ W}$  and  $2789\text{ kg}$ , respectively. taken from [101].

placed far away from the scintillator tiles. The overall scheme of the ACD is depicted in Fig. 2.2. The overall ACD efficiency for detection of singly charged relativistic particles entering the tracking detector from the top or sides of the LAT exceeds the required 0.9997.

The requirement to measure photon energies up to 300 GeV leads to the presence of a heavy calorimeter (see section 2.5) employed to absorb great part of the energy to make this measurement. A small fraction of secondary particles (mostly 100-1000 keV photons) from the electromagnetic shower, created by the incident high energy photon in the calorimeter ( $\sim 1800\text{ kg}$ ), travels backward through the tracker and it crosses the ACD, where they can Compton scatter and thereby induce signals from the recoil electrons. These ACD signals will be interpreted by the instrument as vetoes; real high energy incident photon events could be rejected (see Fig.2.3) this effect is known as *backsplash*. The higher is the primary photon energy, the more intense is the backsplash effect. It was present in EGRET, where the instrument detection efficiency for 10 GeV photons was a factor of two lower than at

1 GeV due to false vetoes caused by backsplash. At energies above  $\sim 50$  GeV EGRET was almost insensitive due to this effect [103]. After several studies [107], according to the design requirement, that vetoes created by backsplash would reject not more than 20% of otherwise accepted photons at 300 GeV, the ACD was segmented in 89 different tiles ( $5 \times 5$  array on the top and 16 tiles on each of the 4 sides). This segmentation strongly suppress the probability that the track (in the tracker subsystem, paragraph 2.4) points back to a scintillating tile with a signal from a backsplash photon. This combination of tracker and ACD information reduces the self-veto rate by nearly two orders of magnitude. Also, with every ACD tile independently wrapped, a punch by a micrometeoroid can disable only one tile, causing system performance degradation by no more than a few percent, which is tolerable.

Overall detection efficiency for incident charged particles is maintained by overlapping scintillator tiles in one direction. In the other direction, gaps between tiles are covered by flexible scintillating fiber ribbons, see Fig. 2.4. The ribbons follow the gaps between tiles and provide detection of particles that hit the gaps. There are a total of eight ribbons, four to cover the gaps along the X-axis and the other four to cover the gaps along the Y-axis, each of them readout by two redundant PMTs. To minimize the chance of fatal light leaks due to penetrations of the light-tight wrapping by micrometeoroids and space debris, the ACD is completely surrounded by a micrometeoroid shield (MMS), with a total area density of  $0.39g/cm^2$ .

The incoming hadronic cosmic rays, at grazing incidence, can interact with the large flat portion of the MMS, producing neutral pions ( $\pi^0$ ), which immediately decay in two  $\gamma$ -rays. Some of this photons can enter the LAT and can be indistinguishable from cosmic gamma rays. This background, that could be as much as 5% of the extragalactic diffuse radiation at energies above several GeV, is minimized by extending the top row of side tiles above the tiles in the ACD top to the upper surface of the micrometeoroid shield (MMS), as shown in the upper panel of Fig. 2.2. This forces charged products of a grazing  $\pi^0$ -production event to pass through and be detected in a scintillator tile. This extension is known as the *crown*. The complete description of the ACD, of its components and readout with all the steps of

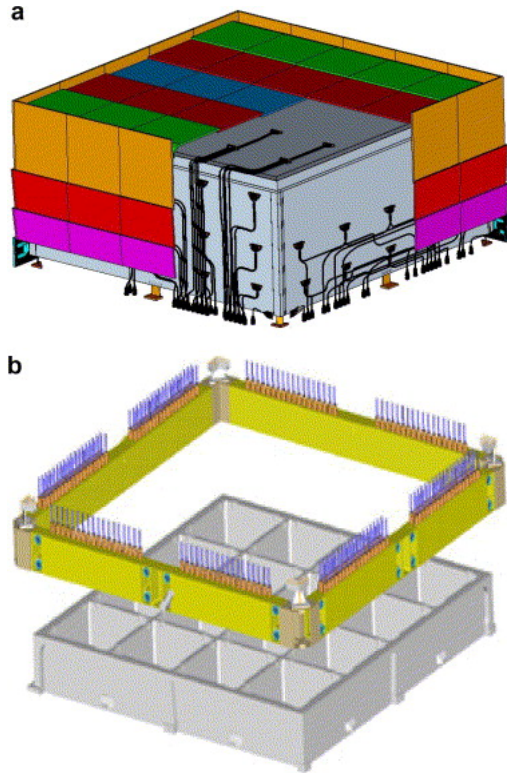


**Figure 2.2:** ACD structure. (a) – ACD tile shell assembly, with tile rows shown in different colors. Clear fiber cables are seen in the cutout. Ribbons and bottom row (long) tiles are not shown. (b) – ACD base electronics assembly (yellow) with PMTs shown. The LAT grid is shown in gray below. Image from [108]

design building and testing could be found in [108] and in [109].

## 2.4 Tracker

The Tracker as a whole consists of 880,000 readout channels, nearly  $74 \text{ m}^2$  of silicon, with a sensitive area of close to  $2 \text{ m}^2$ , and a field of view greater than  $2 \text{ sr}$ . It operates with only  $160 \text{ W}$  of power and is capable of triggering at rates up to at least  $10 \text{ kHz}$  with negligible dead time [110]. Each of the  $4 \times 4$  tracker modules is  $37.3 \text{ cm}$  wide and  $66 \text{ cm}$  high. The width, and hence the number of tracker modules spanning the LAT, was set by the longest silicon strips that were practical to read out with good noise performance, high efficiency, and low power, while the height was optimized to ensure adequate lever arm between successive measurements on a track while keeping the LAT aspect ratio low to maximize the field of view.

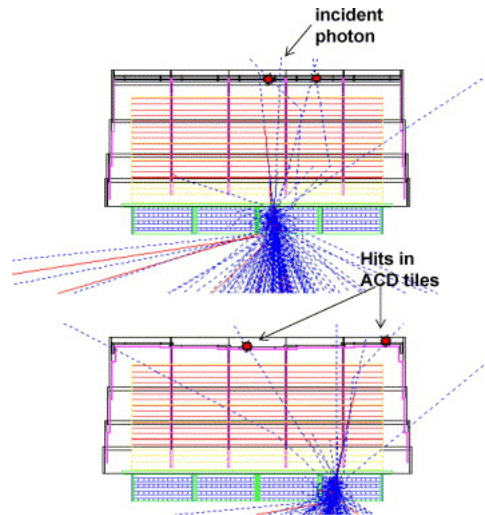


**Figure 2.3:** Backslash in the LAT ACD simulation model. Charged particles are shown by red lines, and photons by blue dashed lines. Signals in the ACD caused by backslash are shown by red dots. Image from [108]

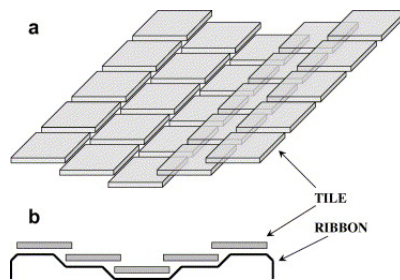


**Figure 2.4:** Schematic of tile overlap (a) and cross section (b) for the top of ACD.

The converter-tracker [101] has 16 planes of high-Z material, namely tungsten, where  $\gamma$ -rays incident on the LAT preferentially convert to an  $e^+e^-$  pair. The converter planes are interleaved with position-sensitive, silicon strip, detectors that log the passage of charged particles, thus measuring the tracks of the particles resulting from pair conversion. This information is used to reconstruct the directions of the incident  $\gamma$ -rays; some possible topologies are depicted in Fig. 2.5. Each tracker module has 18 (x, y) tracking planes, consisting of two layers (x and y) of single-sided silicon strip detectors (SSDs). The exploded view of one of this module is in Fig. 2.6.

The support structure for the detectors and converter foil planes is a stack of 19 *trays* (composite panels), Fig. 2.5, supported by carbon-composite sidewalls that also serve to conduct heat to the base of the tracker array. The tray structure is a low mass, carbon-composite assembly, carbon was chosen for its long radiation length, high modulus stiffness-to-density ratio, good thermal conductivity and stability. The tray-panel structure is about 3 cm thick and is instrumented with converter foils, silicon strip detectors, and front end electronics. All trays are similar, but the top and bottom trays have the silicon strip detectors on only a single face. The bottom trays include the mechanical and thermal interfaces to the grid, while the top trays support the readout-cable terminations, mechanical lifting attachments, and optical survey retroreflectors.

The silicon strips on the top and bottom of a given tray are parallel, while alternate trays are rotated  $90^\circ$  with respect to each other. A (x, y) measurement plane consists of a layer of detectors on the bottom of one tray together with an orthogonal detector layer on the top of the tray positioned just below, with only a 2 mm separation. The tungsten converter foils in the first 16 planes lie immediately above the upper detector layer in each plane. The lowest two (x, y)-planes have no tungsten converter material.

The thickness of the tungsten foil determine the chance that a photon interact and the direction of the pair after the creation. If it is too thin the high energy photons could not interact, determining a smaller effective area (section 2.9.2), while if they are too thick the pair generated by low energy photons could be too much deflected by the original direction of

the photon, increasing the point spread function (PSF)(section 2.9.3). The trade-off between this two characteristics is obtained dividing the tracker in two regions *front* and *back*. The front region (first 12 (x, y) tracking planes) has thin converters, each 0.03 radiation lengths thick to optimize the resolution (PSF) at low energy. The converters in the back (four (x, y)-planes after the front tracker section) are  $\sim 6$  times thicker, to maximize the effective area at the expense of less than a factor of 2 in angular resolution (at 1 GeV) for photons converting in that region. In the high level data product (see section 2.11); the conversion zone, front or back is indicated, so some analysis could be done considering effectively this two part of the telescope as two different instruments. Each of the 16 tracker tower modules is composed of a stack of 19 *trays* supported by four sidewalls, as in Fig. 2.1, the layout could be schematized as following:

- 1 Top tray equipped with only one (Y) tracking plane with the converter foil above;
- 11 thin trays, that are standard trays with two tracking planes and the tungsten converter foil 2.7% radiation length thick ( $\sim 105\mu m$ );
- 4 thick trays that are standard trays equipped with two tracking planes and a tungsten converter foil 18% radiation length in thickness ( $\sim 630\mu m$ ), in order to increase the detection efficiency for high-energy gamma rays;
- 2 standard trays without converter foils;
- 1 Bottom tray equipped with only one Y tracking planes without the converter foil.

The complete depth of the tracker is about 1.5 radiation length.

Trays supporting thick converter foils have stronger face sheets and heavier core material than those supporting thin foils or no foils. The high intrinsic efficiency and reliability of this technology enables straightforward event reconstruction and determination of the direction of the incident photon. The system also measures and records the time-over-threshold

(TOT) of each layer’s trigger output signal, which provides charge-deposition information. The TOT and the pair conversion signature, as in in Fig. 2.5 are useful for background rejection. In particular, isolated tracks that start from showers in the calorimeter sometimes range out in the tracker, mimicking a  $\gamma$ -ray conversion. The TOT information is effective for detecting and rejecting such background events because at the termination of such tracks the charge deposition is very large, often resulting in a large TOT in the last SSD traversed.

The tracker provides the principal trigger for the LAT. Each detector layer in each module outputs a logical OR of all of its 1536 channels, and a first-level trigger is derived from coincidence of successive layers (typically 3 (x, y)-planes). There is no detectable coherent noise in the system, therefore the coincidence rate from electronics noise is immeasurably small, while the trigger efficiency for charged particles approaches 100% when all layers are considered [101].

The whole system was designed for a really high reliability, all the 16 modules operate independently, providing much redundancy. Similarly, the multilayer design of each module provides redundancy. The readout system is also designed to minimize or eliminate the impact of single-point failures. Each tracker layer has two separate readout and control paths, and the 24 amplifier-discriminator chips in each layer can be partitioned between the two paths by remote command. Therefore, failure of a single chip or readout cable would result in the loss of at most only 64 channels.

## 2.5 Calorimeter

The electronic calorimeter has two different primary objectives:

- Measure the energy deposition due to the electromagnetic particle shower initiated by the  $e^+e^-$  pair produced by the incident photon. It must have adequate depth to contain most of the energy of the gamma-ray showers. In general this means that shower maximum must be within the detector. The calorimeter must contain a sufficiently high fraction of active detector material that the total energy measurement is not dominated by “sampling” statistics.

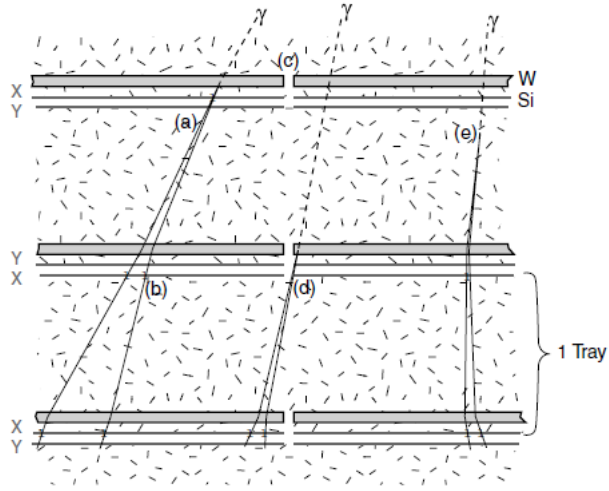


**Figure 2.5:** Illustration of tracker design principles. The first two points dominate the measurement of the photon direction, especially at low energy. (Note that in this projection only the  $x$  hits can be displayed.) (a) Ideal conversion in  $W$ :  $Si$  detectors are located as close as possible to the  $W$  foils, to minimize the lever arm for multiple scattering. Therefore, scattering in the second  $W$  layer has very little impact on the measurement. (b) Fine detectors segmentation can separately detect the two particles in many cases, enhancing both the PSF and the background rejection. (c) Converter foils cover only the active area of the Silicon strip detector, to minimize conversions for which a close-by measurement is not possible. (d) A missed hit in the first or second layer can degrade the PSF, see section 2.9.3, by up to a factor of 2, so it is important to have such inefficiencies well localized and identifiable, rather than spread across the active area. (e) A conversion in the structural material or  $Si$  can give long lever arms for multiple scattering, so such material is minimized. Good two-hit resolution can help identify such conversions.

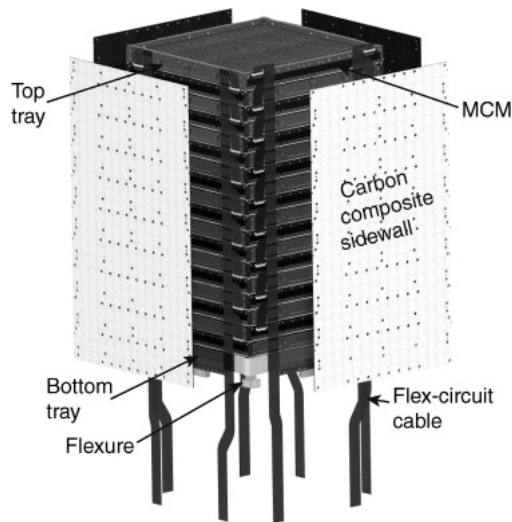


**Figure 2.6:** Exploded view of a Tracker tower module. The detailed cable terminations at the top have been omitted, for more information see [110].

- Image the shower development profile, thereby providing an important background discrimination and an estimator of the shower energy leakage fluctuations.

Both these needs were addressed in the design process of the LAT [111] and [112], ground calibrations and studies of the radiation damage are in [113]. In the following calorimeter's main characteristics will be described, its scheme is depicted in Fig. 2.7.

The electromagnetic calorimeter consists of 16 towers of CsI(Tl) crystals. Each tower contains 8 layers of 12 crystals (each  $326.0 \times 26.7 \times 19.9 \text{ mm}^3$ ) arranged in a hodoscopic fashion, alternate layers are arranged orthogonally [114], see Fig. 2.7. The  $4 \times 4$  structure was adopted for compatibility with the geometry of the electronic readout of the tracker, that is intrinsically modular. This structure was really helpful in the building and testing phase. The CsI crystals in each calorimeter module are housed in a carbon composite cell structure and each of the crystal is optically isolated.

Each of the 1536 crystals is read out by two dual-photodiode assemblies (one at each end) in order to measure the scintillation light produced in the crystal. Each photodiode assembly contains a large-area photodiode to measure small energy depositions, and a small-area photodiode to measure large energy depositions. The large photodiodes, with area  $147 \text{ mm}^2$ , cover the range 2 MeV– 1.6 GeV, while the small photodiodes, with area  $25 \text{ mm}^2$ , cover the range 100 MeV– 70 GeV. Each crystal end has its own front end electronics and pre-amplifier electronics assembly. Both low and high energy signals go through a pre-amplifier and shaper and then a pair of Track and Hold circuits with gains differing nominally by a factor of 8. An energy domain selection circuit routes the best energy measurement through an analog multiplexer to an Analog to Digital Converter. A calibration charge injection signal can be fed directly to the front end of the pre-amplifiers.

The final size of the CsI crystals is a compromise between electronic channel count and desired segmentation within the calorimeter; the dimension of each crystal are comparable with the main characteristic length of the CsI(Tl) (its interaction length is of 36 cm). Although the calorimeter is only 8.6 radiation lengths deep (the tracker is 1.5), the

longitudinal segmentation enables energy measurements up to a TeV. From the longitudinal shower profile, an unbiased estimate of the initial electron energy is derived by fitting the measurements to an analytical description of the energy-dependent mean longitudinal profile. Except for the lower end of the energy range, the resulting energy resolution is limited by fluctuations in the shower leakage as described in [207] and [104].

Each CsI crystal provides three spatial coordinates for the energy deposited within, two discrete coordinates from the physical location of the crystal in the array and the third, more precise, coordinate determined by measuring the light yield asymmetry at the ends of the crystal along its long dimension. The position resolution achieved by the ratio of light seen at each end of a crystal scales with the deposited energy and ranges from a few millimeters for low energy depositions ( $\sim 10$  MeV) to a fraction of a millimeter for large energy depositions ( $> 1$  GeV). Simple analytic forms are used to convert the light asymmetry into a position. The calorimeter's shower imaging capability and depth enable the high-energy reach of the LAT and contribute significantly to background rejection.

Calibrations of the calorimeter energy scale and crystal response map are performed on galactic cosmic rays that are accepted by event filters running in LAT flight software at all times in nominal flight operations. Calibration of the electronic gain and linearity of each electronic modules, however, is performed on data acquired by charge-injection calibration runs that are scheduled one to two times per year by ground command. Details of the on-orbit calibration plan, processes, and derived quantities are in [207] and the update to the whole second here is in [112].

## 2.6 DAQ and trigger logic

The Data Acquisition System (DAQ), [101] and [115], collects the data from the other subsystems, implements the multilevel event trigger, provides onboard event processing to run filter algorithms to reduce the number of downlinked events, and provides an onboard science analysis platform to rapidly search for transients.

The DAQ architecture is hierarchical as shown in Fig. 2.8. At the

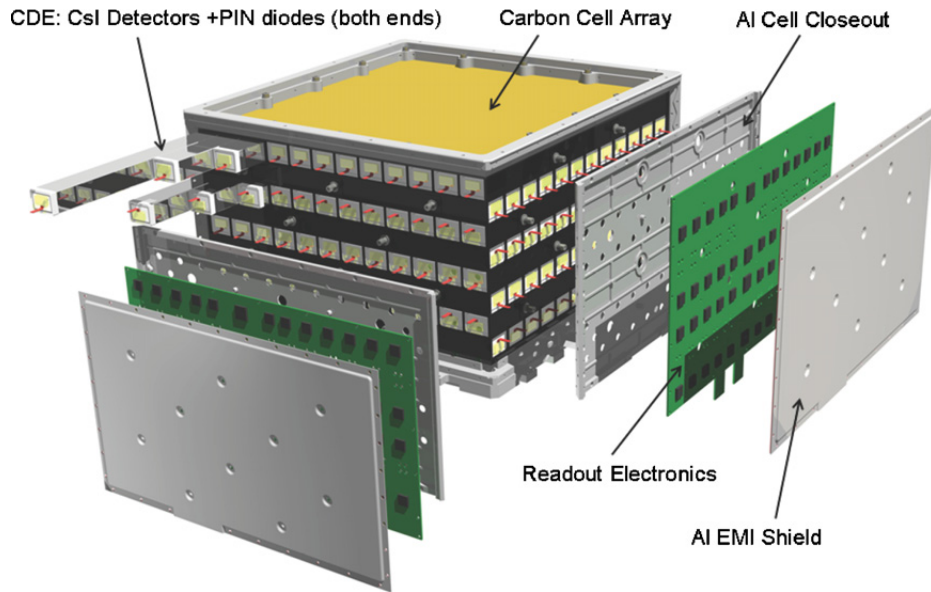


**Figure 2.7:** LAT calorimeter module. The 96 CsI(Tl) scintillator crystal detector elements are arranged in eight layers, with the orientation of the crystals in adjacent layers rotated by  $90^\circ$ . The total calorimeter depth (at normal incidence) is 8.6 radiation lengths. Taken from [101].

lowest level shown, each of 16 Tower Electronics Modules (TEMs) provides the interface to the tracker and calorimeter pair in one of the towers. Each TEM generates instrument trigger primitives from combinations of tower subsystem (tracker and calorimeter) triggers, provides event buffering to support event readout, and communicates with the instrument-level Event Builder Module (EBM) that is part of the Global-trigger/ACD-module/Signal distribution Unit (GASU). The GASU consists of:

- the Command Response Unit (CRU) that sends and receives commands and distributes the DAQ clock signal,
- the Global-Trigger Electronics Module (GEM) that generates LAT-wide readout decision signals based on trigger primitives from the TEMs and the ACD,
- the ACD Electronics Module (AEM) that performs tasks, much like a TEM, for the ACD,
- the EBM that builds complete LAT events out of the information

provided by the TEMs and the AEM, and sends them to dynamically selected target Event Processor Units (EPUs).

There are two operating EPUs to support onboard processing of events with filter algorithms designed to reduce the event rate from 2–4 kHz to  $\sim 400$  Hz that is then downlinked for processing on the ground. The onboard filters are optimized to remove charged particle background events and to maximize the rate of  $\gamma$ -ray triggered events within the total rate that can be downlinked. Finally, the Spacecraft Interface Unit (SIU) controls the LAT and hosts the command interface to the spacecraft [101](see Fig. 2.9).

There is also a Power Distribution Unit (PDU), which is also redundant, that controls spacecraft power to the TEMs, the GASU, and the EPUs. In turn, the TEMs control power to the tracker and the calorimeter modules and the GASU controls power to the ACD. Power to the SIUs is directly provided by the spacecraft.

An instrument-level trigger acceptance message (TAM) signal is issued by the GEM, only if the GEM logic is fulfilled by the input trigger primitives within the (adjustable) trigger window width. The TAM signal is sent to each TEM and to the AEM with no delays. Upon receipt of the TAM signal, a Trigger Acknowledge (TACK) signal with an adjustable delay is sent by the TEM to the tracker front ends and a command, also with an adjustable delay, is sent to the calorimeter front ends. The AEM sends a signal to the ACD front ends. The TACK causes the entire instrument to be read out (e.g., addresses of hit strips in the tracker and TOT for each layer in each tracker module, and pulse heights for all 3072 calorimeter channels and 216 ACD channels). Any of the TEMs or the AEM can issue a trigger request to the GEM. The time between a particle interaction in the LAT that causes an event trigger and the latching of the tracker discriminators is 2.3–2.4  $\mu\text{s}$ , much of this delay due to the analog rise times in the tracker front end electronics. Similarly, the latching of the analog sample-and-holds for the calorimeter and the ACD are delayed (programmable delay of  $\sim 2.5$   $\mu\text{s}$ ) until the shaped analog signals peak. The minimum instrumental dead time per event readout is 26.50  $\mu\text{s}$  and is the time required to latch the trigger information in the GEM and send it from the GEM to the EBM

[101]. The GEM then evaluates the overall dead time, the system records this information and adds it to the data stream transmitted to the ground and it is used for evaluate the livetime fraction used in the high level dataset, see paragraph 2.11.

Any of the TEMs can generate a trigger request in two ways:

- If any tracker channel in the tracker module is over threshold, a trigger request is sent to the module's TEM which then checks if a trigger condition is fulfilled, typically requiring triggers from three (x, y)-planes in a row. If this condition is satisfied, the TEM sends a trigger request to the GEM.
- If a predetermined low-energy (CAL-LO) or high-energy (CAL-HI) threshold is exceeded for any crystal in the calorimeter module, a trigger request is sent to the GEM.

The prompt ACD signals sent to the GEM are of two types:

- a discriminated signal (nominal 0.4 MIPs threshold) from each of the 97 scintillators (89 tiles and 8 ribbons) of the ACD, used to (potentially) veto tracker triggers originating in any one of the sixteen towers,
- an high-level discriminated signal (nominal 20 MIPs threshold) generated by highly ionizing heavy nuclei cosmic-rays (carbon–nitrogen–oxygen or CNO), used for energy calibration purposes.

Finally, non-detector based trigger inputs to the GEM are used for calibration and diagnostic purposes. The GEM can utilize also a periodic signal (2 Hz) and a solicited trigger signal input that allows the instrument to be triggered through operator intervention. The spacecraft clock is also used to strobe the internal time base of the GEM, thus allowing an accurate measurement of the time of an event relative to the spacecraft clock.

Table 2.1 summarizes the observed LAT trigger rates, live time and event rates [115]. The large difference between trigger request and acknowledge rates is caused by the pre-scaling of tracker triggers with coincident ACD tile

hit – these background events are only sampled, greatly reducing the number of events acquired. The trigger acknowledge rate also includes an unbiased sample of all trigger conditions at a low sampling rate (2 Hz) for onboard calibration and test. Data compression algorithms are also applied to the filtered events to further reduce the downlink data volume. The minimum instrumental dead time per event readout is  $26.50 \mu\text{s}$  however additional deadtime can arise from back-pressure from full buffers.

*Table 2.1: Daily average on-orbit trigger and event rates*

Trigger requests from detector elements	13.5 kHz
Trigger acknowledge rate from global trigger unit	2.3 kHz
LAT live time	92.1%
On-board filter output event rate	460 Hz
Classified as potential photons	285 Hz
Classified as particles or unknown	175 Hz
Average Event Size Uncompressed	2,200 bytes
Compressed	480 bytes
Average data rate transmitted to ground	1.5 Mbits/s

## 2.7 Event reconstruction

After triggering and onboard filtering, accepted candidate photons are downlinked to Earth, where they undergo the full event reconstruction and data analysis. The event reconstruction processes the raw data from the various subsystems, correlating and unifying them under a unique event hypothesis. The development of the reconstruction relies heavily on the Monte Carlo simulation of the events. The Fermi LAT Monte Carlo [101] is based on the Geant4 Monte Carlo toolkit [116].

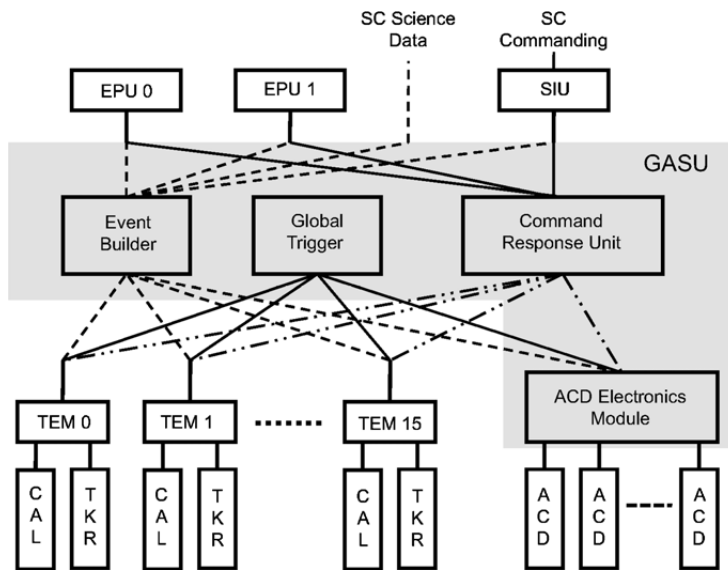


**Figure 2.8:** LAT Data Acquisition System (DAQ) architecture. The GASU consists of the AEM, the Global Trigger Module (GTM), the EBM, and the CRU. The trigger and data readout from each of the 16 pairs of tracker and calorimeter modules is supported by a TEM. There are two primary Event Processing Units (EPU) and one primary Spacecraft Interface Unit (SIU). Not shown on the diagram are the redundant units (e.g., 1 SIU, 1 EPU, 1 GASU) and the Power Distribution Unit (PDU), that is also redundant. For more details see text and [101].

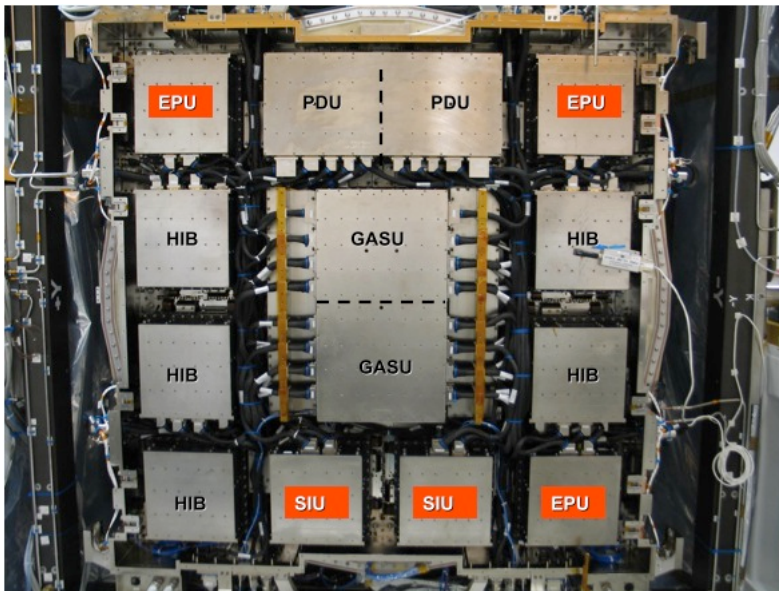


**Figure 2.9:** Trigger and data acquisition electronics and cabling mounted on the bottom side of the LAT consist of 16 Tower Electronic Modules (TEM) and power supplies, 3 event processing units, 2 spacecraft interface units, a global trigger-ACD- and system communications unit, a power distribution unit, and 4 heater interface boxes.

Spatially adjacent hit tracker strips are grouped together, forming *clusters*, and the coordinates of these clusters are used in the track finding and fitting. Each cluster determines a precise location in two space coordinate  $z$  and either  $x$  or  $y$ . The other coordinate is evaluated from the information in the following SSD tracker plane, in case of multiple tracks the ambiguity is resolved using information from different layers or from the calorimeter.

In the core of track-finding algorithms there is a mechanism to generate a trajectory (*track hypothesis*) that can be rejected or accepted on the base of its consistency with the sensor readouts. The generation algorithm is combinatorial, with a significant constraint imposed on the number of trial trajectories considered, for the limited computing power. Two algorithms [101] are used:

- *Calorimeter-Seeded Pattern Recognition (CSPR)*. For most of the LAT science analysis, some energy deposition in the calorimeter is required. In few new loose cuts this requirement can be relaxed, just for transient studies see par. 2.8. If there is some energy collected by the calorimeter, the three-dimensional energy centroid is computed along with energy moments (similar to the moment of inertia, but with energy in place of mass). The shower direction is given by the eigenvector with the smallest eigenvalue. Initially, the overall energy is taken to be the sum of the crystal energies. The CSPR algorithm is based on the assumption that the energy centroid lies on the trajectory. The first hit on the hypothesized track, composed of an  $(x, y)$  pair from the layer in the tracker furthest from the calorimeter, is selected randomly from the possible  $(x, y)$  pairs. If a subsequent hit is found to be close to the line between the first hit and the location of the energy centroid in the calorimeter, a *track hypothesis* is generated. The candidate track is then populated with hits in the intervening layers if they are close enough to the track, a correct estimate of the multiple scattering is included, using an adaptation of Kalman fitting (e.g., [117]). Adding more hits to the track is terminated when more than a specified number of gaps have accumulated (nominally two).

The whole process is repeated, starting with each possible  $(x, y)$  pair in the furthest plane from the calorimeter and then continued using pairs from closer layers. After a track of sufficient quality is found, and at least two layers have been looped over, the process is terminated. Only the *best* track is retained, while all the others tracks are discarded. The bias caused by the track quality parameters makes this *the longest, straightest track* and hence, for  $\gamma$  conversions, preferentially the higher-energy track of the  $e^+e^-$  pair. At high energies ( $>1$  GeV) the first-hit search is limited to a cone around the direction provided by the calorimeter moments analysis in order to minimize confusion with hits caused by secondary particles generated by backsplash. The cone angle is narrowed as the energy increases, reflecting the improved directional information provided by the calorimeter.

- *Blind Search Pattern Recognition* (BSPR). In this algorithm, calorimeter information is not used for track finding. Events having essentially no energy deposition in the calorimeter are analyzed using this algorithm as well as for subsequent track finding following the CSPR. The same procedure described is used, but here the selection of the second hit, used for create the initial trajectory is now done randomly from the next closest layer to the calorimeter. The trajectory formed by these two hits is projected onto the following layer and if a hit in that layer lies sufficiently close to the projection a trial track is generated.

Hits are allowed to be shared between tracks if the hit is the first hit on the best track (two tracks forming a vertex) or if the cluster size (number of strips) is larger than expected for the track already assigned to that hit. The total number of tracks allowed to be found is limited (10 by default), and all of this are stored in the data files. The final stage of track reconstruction combines tracks into vertices, basically the points where the pair is created. The process begins with the best track. The second track is selected by simply looping over the other tracks in the event. The distance of closest approach between the best track and the candidate second track is computed and if within a specified distance (6 mm by default) a vertex

solution is generated by covariantly combining the parameters of the two tracks. The z-axis location (coordinate along the instrument axis) of the vertex candidate is selected using the detailed topology of the first hits and is assigned either to be in the center of the preceding tungsten foil radiator, in the silicon detector itself, or within the core material of the tracker tray directly above the first hit. A quality parameter is evaluated, namely, the first track that is paired with the track having the best quality parameter. The process continues iteratively trying to find a vertex for each track; when it fails the track is assigned to a vertex by itself. In addition to the previous vertexing discussed above, an additional improvement is possible if calorimeter information is included. This are particularly important in some cases when much of the energy lost in the interaction is in photons [101].

At low energy ( $\sim 100$  MeV), a significant fraction ( $\sim 50\%$ ) of the energy in a photon conversion event can be deposited in the tracker. This energy fraction is evaluated, considering the tracker as a sampling calorimeter, and added to the corrected calorimeter energy. The event energy is re-evaluated using the final track reconstruction with three different algorithm: a *parametric correction* (PC) based on the barycenter of the shower, a fit to the *shower profile* (SP) taking into account the longitudinal and transverse development of the shower, and a *maximum likelihood* (LK) fit based on the correlations of the overall total energy deposited with the number of hits in the tracker and with the energy seen in the last layer. The PC works in the full LAT energy range, while the SP is applicable above 1 GeV and the LK method works below 300 GeV. The best track and energy value are chosen using classification threes (CT) [118], that return for both also the corresponding *probability*, expressing the degree of confidence that the chosen values do not lie far from the core of the corresponding distribution.

After energy and direction are selected, an additional background rejection stage is applied, improving the on-orbit filtering, described in the previous paragraph. To do this, information from all LAT subsystems is examined in detail and several figures-of-merit are evaluated using automated data-mining techniques based on CT.

All these automated algorithms are trained on detailed Monte Carlo

simulations of the behavior of and background particles hitting the LAT. A complete background model [101] was developed, it includes cosmic rays and earth albedo  $\gamma$ -rays within the energy range 10 MeV to  $10^6$  MeV. Any particles that might either make non-astrophysical  $\gamma$ -rays and/or need to be rejected as background are included. The model does not include X-rays or soft  $\gamma$ -rays that might cause individual detectors within the LAT to be activated. The model is created using the data of several space experiment as EGRET and AMS; the full table of the source is in [101].

## 2.8 Event classification

As a result of the on-ground reconstruction analysis the direction and the energy of each photons is determined, with the corresponding confidence levels and the estimates of the probability that the event describes a photon and not a background particle. From this high-level parameters and probability each photon is associated to one of the three (for now) standard event classes. The definition and the aim of each class is highlighted in the Table 2.2. They were developed and introduced before the launch based on the background expected in orbit and the performance of the LAT [101]. The use of at least 3 standard classes was needed for the broad range of LAT observations and analysis. Different science topics leads to different optimizations of the event selections and different rates of residual backgrounds. The trade-off is between efficiency in detection, necessary for the study of transient source (that last from few seconds to few minutes as GRBs and solar flares), and resolution and low background contamination really useful in the study of the diffuse radiation and steady point sources.

The background rejection analysis has been constructed to allow analysis classes to be optimized for specific science topics. Further looser cuts have been applied on LAT data just for timing analysis of the gamma ray bursts, since the energyreconstruction in that case is still not validated and reliable. Additional looser cuts, even without calorimeter information are actively being tested and will be used for source analysis in the near future.

Common to all of these analysis classes is the rejection of the charged-particle backgrounds entering within the FoV. The classes are separated

by an increasingly tighter requiring that the candidate photon events in both the tracker and the calorimeter behave as expected for  $\gamma$ -ray induced electromagnetic showers. The loosest cuts apply to the *Transient class*, for which the background rejection was set to allow a background rate of  $< 2$  Hz, estimated using a pre-launch background model, which would result in no more than one background event every 5 s inside a  $10^\circ$  radius about a source. The *Source class* was designed so that the residual background contamination was similar to that expected from the extragalactic  $\gamma$ -ray background (EGRB) flux over the entire Field of View. Finally, the *Diffuse class* has the best background rejection and was designed such that harsher cuts would not significantly improve the signal to noise ratio. These three analysis classes are hierarchical; it means that all events in the diffuse class are contained in the Source class and all events in the Source class are in the Transient class. The event of the diffuse class are flagged with a class level equal to 3 and the source class are all the ones flagged with 2 and 3, so on for the transient class.

The residuals of background events for the three analysis classes are shown in Fig. 2.10. For the diffuse class, the resulting rejection factor is  $\sim 1 : 10^6$  at some energies (e.g.,  $\sim 10$  GeV) while retaining  $> 80\%$  efficiency for retaining  $\gamma$ -ray events. The residual background is worse at low energy particularly for events originating in the thick radiator portion of the tracker. It happens here that “splash” backgrounds, entering the backside of the calorimeter can undergo interactions that result in low energy particles which range out in the thick radiators, thus mimicking an event originating in the thick tracker section. In this sense, the thick section shields the thin section from this flux and hence the thin section is somewhat cleaner.

In the analysis of a GRB, the relatively small region of the sky as well as the very short time window of the prompt phase ( $\sim$  few tens of seconds) allow the background rejection cuts to be relaxed relative to an analysis of a diffuse source covering a large portion of the sky. Furthermore a key science attribute for GRB observations is the time evolution and the measurement sensitivity to rapid time variation scales as the square root of the number of detected burst photons. Given this requirement the standard event class for the prompt phase is the *Transient*. For the analysis of the long lasting

Analysis Class	Residual Background Rate (Hz)	Characteristics	Class level
Transient	2	Maximize effective area, particularly at low energy, at the expense of higher residual background rate; suitable for study of localized, transient sources	1-3
Source	0.4	Residual background rate comparable to extragalactic diffuse rate estimated from EGRET; suitable for study of localized sources	2-3
Diffuse	0.1	Residual background rate comparable to irreducible limit and tails of PSF at high-energy minimized; suitable for study of the weakest diffuse sources expected.	3

**Table 2.2:** *LAT analysis class [101].*

emission ( $\sim 1ks$ ) a cleaner data sample is needed and the Diffuse class is used as for the analysis of all the other point sources.

The absolute LAT energy scale, at this early stage of the mission, is determined with an uncertainty of  $+5\% -10\%$ , for more details see [208], its main effect is to rigidly shift any observed spectrum by  $+10\% -20\%$  without introducing significant deformations.

## 2.9 LAT Instrument Response Function

The Instrument Response Functions (IRFs) are a set of analytical functions that describe the response of a detector to an incoming flux of particles. If  $F$  is the differential incident flux from a source, the differential flux of detected particle is given by the following equation:

$$\frac{dN(E', \vec{v}')}{dE dt} = R(E', \vec{v}' | E, \vec{v}) F(E, \vec{v}), \quad (2.9.1)$$

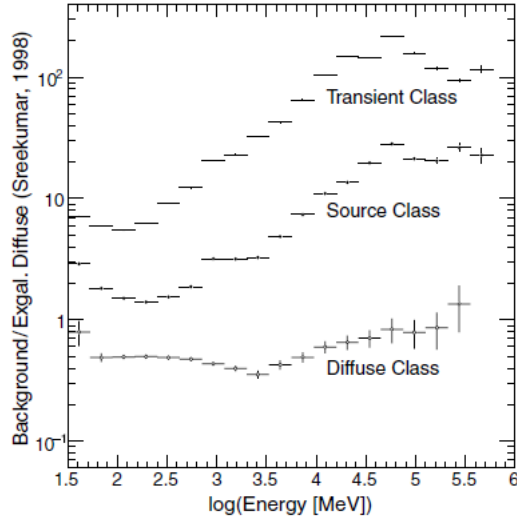


**Figure 2.10:** Ratio of the residual background to the extragalactic diffuse background inferred from EGRET observations[119] for each of the three prelaunch analysis classes (P6-V1). The integral EGRET diffuse flux is  $1.45 \times 10^{-7} \text{ ph cm}^{-2} \text{ s}^{-1} \text{ sr}^{-1}$  above 100 MeV [101].

where  $E$  and  $\vec{v}$  ( $E'$  and  $\vec{v}'$ ) are respectively the energy and the direction of the incident (measured and reconstructed) photon and  $R(E', \vec{v}' | E, \vec{v})$  is the **Instrument Response Function**. This function is usually factorized as in the following equation:

$$R(E', \vec{v}' | E, \vec{v}) = A_{eff}(E, \vec{v}) PSF(\vec{v}' | E, \vec{v}) \Delta E(E' | E, \vec{v}). \quad (2.9.2)$$

The three function in the right part of the previous equation are:

- $A_{eff}(E, \vec{v})$  is the *Effective Area* of the detector,
- $PSF(\vec{v}' | E, \vec{v})$  is the *Point Spread Function*,
- $\Delta E(E' | E, \vec{v})$  is the *Energy Dispersion* (here and in the following considered independent to the measured direction of the photon  $\vec{v}'$ ).

A full explanation of the instrument response functions theory could be found in [120] and in [106].

### 2.9.1 IRFs versions

The Instrument Response Functions (IRFs) depend not only on the instrument itself, but also on the reconstruction algorithms and its version,

on the background rejection algorithm, and on any eventual selection of the events, that are basically the event classes, see Table 2.2. The various analysis cuts, event selections and the IRFs optimized before the launch [101], known as P6\_V1, are being optimized for the conditions found on-orbit during the all-sky survey phase. The IRFs obtained after the first year are known as P6\_V3 [121] and are the ones used up to now. A new set of IRFs, called P7, are being developed and tested inside the collaboration. In the P7 other science classes will be made available for the analysis, as looser cuts for the transients and selection for charged particles; energies below 100 MeV will be usable and new science results will be possible.

The switch between the P6\_V3 and the P6\_V1 IRFs was needed since onboard were observed the so called *ghost events*[121] that were not previously introduced in the Monte Carlo simulations. The use of the old P6\_V1 can bias the analysis. To make an example of the ghost events effect, let us consider a background event releasing energy in the detector active volumes. Most background events are easily recognizable, so we can assume that a trigger request is not issued and the LAT remains in an active state, waiting for a photon event. If a  $\gamma$ -ray strikes the LAT and triggers the data acquisition, while the energy released by the background particle is still being collected from sensitive volumes, signals caused by both the photon and the background hit are read. This signal are then digitized and transmitted to the Earth. When looking at the downlinked event we see the  $\gamma$  event, plus artifacts due to the ghost background hit. A certain amount of perfectly legitimate photon events have their signal mixed up with background events. The reconstruction routines (DT, see paragraph 2.7) trained on samples unaffected by ghost effect could discard them reducing the efficiency. The spectral analysis done with the IRFs obtained from a Monte Carlo sample without ghost events, as the P6\_V1, are affected by a systematic overestimate of the LAT efficiency. The P6\_V3 IRFs does not correct the reconstruction, taking care of the spurious signal, as the P7 will do, but introducing the ghost effect in the MonteCarlo, a correct modeling of the instrument is achieved. This effect was implemented in the Monte Carlo using an appropriate sample of flight data periodic triggers overlayed as a background to standard simulations of gamma-rays;

the resulting performance was derived by applying pre-launch event analysis to such updated simulations.

Since the IRFs are strongly dependent to the hardware of the telescope, two kinds of them are separately generated for the FRONT or THIN part of the tracker detector and BACK or THICK part of it. They can be used together by combining them or choosing only events that convert in the FRONT (top 12 layers) or BACK and using the correspondent IRFs. An online LAT performance page <sup>1</sup> is kept updated in case of IRFs change.

### 2.9.2 Effective Area, Acceptance and Field of View

The Effective area as introduced before, depends on the incident photon energy and direction respect to the telescope. The direction of the incident  $\gamma$ -rays is expressed in polar coordinates centered in the LAT, the z axis is directly towards the LAT (from the calorimeter to the tracker), while the Y axis is along the solar panels. The dependence of the IRFs in function of the  $\phi$  angle (respect to the Y axis) was investigate with the *P6\_V5* IRFs, the efficiency shows a 4-fold symmetry over the azimuthal angle around the LAT z axis, with a variation of the order of a few percent [121]. Following this result the dependence from the  $\phi$  angle is not considered by now. The Effective Area is then evaluated from Monte Carlo and stored in a 2D matrix in function of  $\log(E)$  and  $\cos(\theta)$ , in respectively 60 and 32 bins. It's evaluated with  $\cos(\theta)$  between 0.2 and 1 (the normal incidence) and with energy between 18 MeV and 560 GeV. In the bin (i,j) the effective area results:

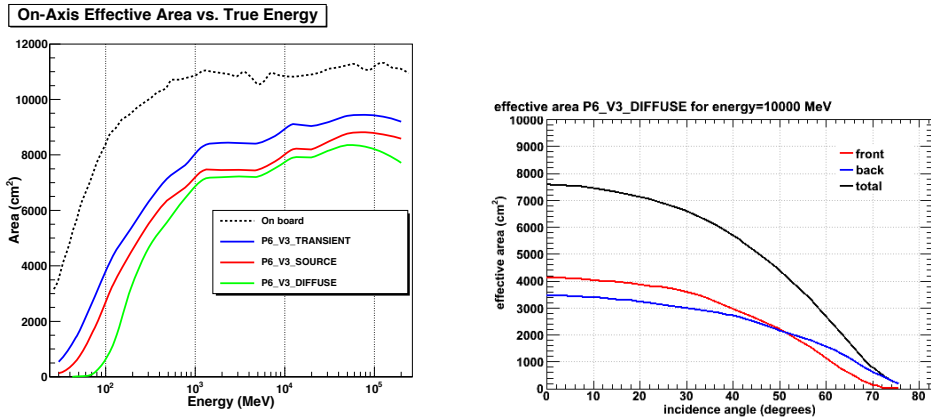
$$A_{eff}(\log(E_i), \cos\theta_j) = \frac{N_{sel}(\log(E_i), \cos\theta_j) A_{gen}}{N_{gen}(\log(E_i), \cos\theta_j)}, \quad (2.9.3)$$

where  $N_{gen}$  is the number of simulated photons on the surface  $A_{gen}$  (usually a sphere around the LAT) while  $N_{sel}$  is the number of photons detected. The on-axis effective area reported here is about 7000  $cm^2$  at 1 GeV; at the same energy this is approximately 10% lower than the pre-launch effective area (P6\_V1) corresponding to the same event selection. This decrease lies within the level of systematics evaluated for pre-flight performance [121].

In Fig. 2.11(a) the on-axis (normal incidence) effective area as a function

---

<sup>1</sup>[http://www-glast.slac.stanford.edu/software/IS/glast\\_lat\\_performance.htm](http://www-glast.slac.stanford.edu/software/IS/glast_lat_performance.htm)



(a) Effective area for normal incidence (defined here as  $\cos(\theta) > 0.975$ ) photons for the onboard selection and for the three standard event classes (b) Effective area for 10 GeV photons as a function of incidence angle for the DIFFUSE class, divided also in FRONT and BACK and the total (FRONT + BACK)

*Figure 2.11: LAT effective area (for the onboard performances see [209])*

of energy for each of the three event classes, described in table 2.2, are depicted. The onboard effective area [209] in Fig. 2.11(a) is shown for comparison, it is larger due to the looser cut for the onboard selection, but the astrophysical photons are diluted by a larger background flux, therefore the onboard burst trigger is not as sensitive as the on ground ones. The onboard LAT notices use this kind of selection, see paragraph 2.15. In the plot 2.11(b) it is shown the Effective Area in function of the incidence angle for the diffuse class for the front and back of the detector and together, each part of the detector contribute for around an half of the total. At low energies, below hundreds of MeV, the effective area for the transient class is a factor of  $\sim 1.5$  larger than the for the diffuse class. This characteristics, with the background contamination [101] shown in Fig. 2.10, make the transient class the best suited for the study of source in really short time scale where the expected background is really small. The decrease in effective area with respect to pre-flight estimates (P6\_V1) lies within the level of systematics evaluated for pre-flight performance: the efficiency degradation is estimated to be less than 20% above 200 MeV.

The Field Of View (FOV) is the Acceptance, Effective Area integrated over the solid angle (all the possible incident directions of the photons),

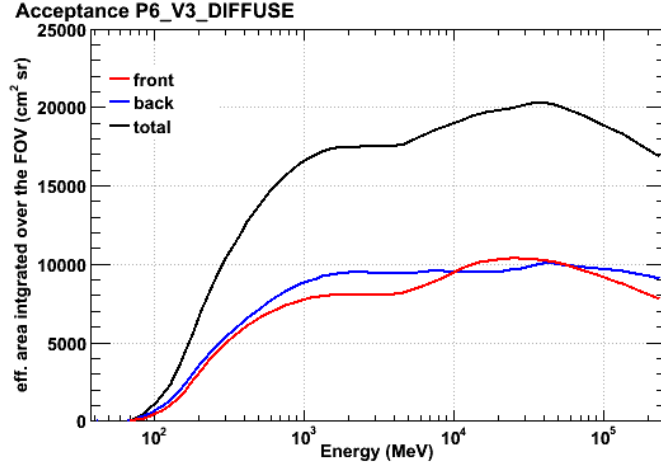


**Figure 2.12:** LAT acceptance in function of the incident photon energy for the Diffuse class (FRONT and BACK are shown separated and joint)

divided for the peak Effective Area:

$$FOV = \frac{Acceptance}{A_{eff}(0,0)} = \frac{\int A_{eff}(\theta, \phi) d\Omega}{A_{eff,peak}}. \quad (2.9.4)$$

For the LAT after all the cuts and the background selection is around 2.4 sr at 1 GeV. This big value is due to the overall aspect ratio of the LAT tracker (height/width) of 0.4. In Fig. 2.12 the acceptance of the LAT in function of the incident photon energy for the diffuse class is shown. The difference with the other classes are higher at low energies. The acceptance has a slower turn-on with respect to the effective area, highlighting the dependence of the FOV on energy. The plot shows the intrinsic acceptance regardless of the orbital characteristics. To obtain the effective acceptance, the curve has to be scaled by a constant factor which takes into account the instrument deadtime, the South Atlantic Anomaly (see paragraph 2.14) and details of the observation strategy (about 20% for standard survey and according to current simulations).

### 2.9.3 Point Spread Function

The probability distribution for the reconstructed direction of incident  $\gamma$ -rays from a point source is referred to as the Point Spread Function (PSF). Multiple scattering of the  $e^+$  and  $e^-$  and bremsstrahlung production limit the obtainable resolution. To get optimal results the  $e^-$  and  $e^+$  directions

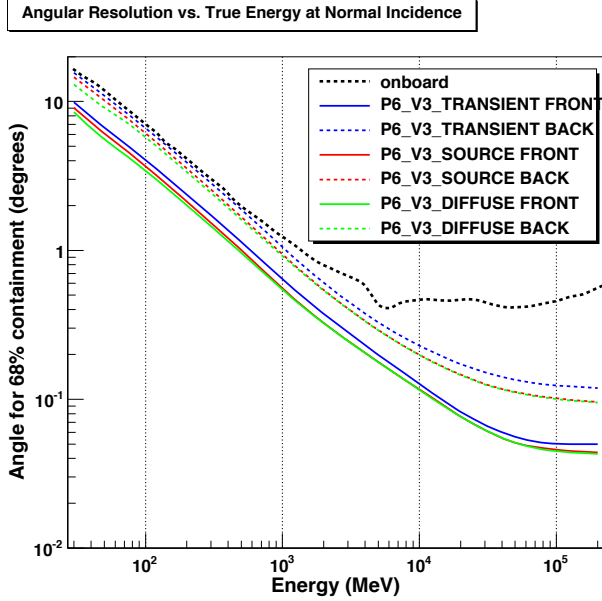


**Figure 2.13:** Angles for 68% containment of the reconstructed incoming photon direction, for normal incidence photons (defined as  $\cos(\theta) > 0.9$ ), are in the LAT performance page

must be measured immediately following the conversion. At 100 MeV the loss for missing one of the first hits is about a factor of 2 in resolution, resulting in large tails in the PSF. The containment radius shown in Fig.2.13 is the angle  $\theta = \arccos(\vec{v} \cdot \vec{v}')$ , where  $\vec{v}$   $\vec{v}'$  are respectively incident direction and reconstructed ones. In Fig. 2.13 the containment radius at 68% (this fraction of the MC sample has a smaller or equal containment radius) of both the three standard analysis classes and the onboard PSF [209]. The onboard reconstruction for hardware limitation gives a larger onboard PSF resulting in larger localizations uncertainties.

#### 2.9.4 Energy Dispersion

The Energy Redistribution Function describes the probability density to have a reconstructed energy  $E'$ , given the true energy  $E$  and the true incoming direction of the photons. In the ideal case, at fixed energy of the incoming photons, the energy redistribution function is a delta function. In real detectors, the energy response function is a curve that typically can be fitted with a Gaussian with a mean value ( $E_{mean}$ ) and a standard deviation

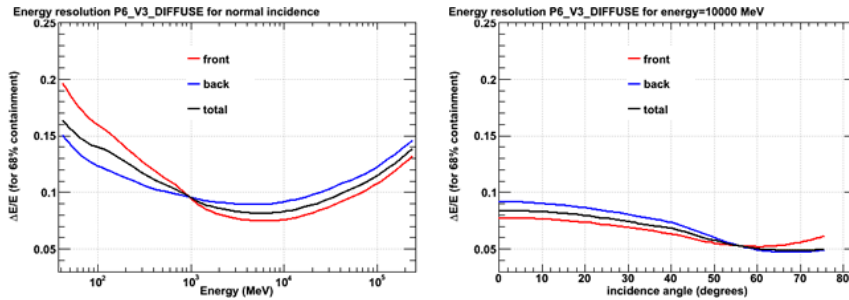


**Figure 2.14:** LAT energy resolution for the diffuse class, 68% containment of the reconstructed incoming photon energy. The plot on the left is for normal incident photons (defined as  $\cos(\theta) > 0.9$ ); the one on the right is for 10 GeV photons as a function of incidence angle.

$\sigma$ . A good description of the Energy Redistribution function can be given, for each value of the true energy  $E$ , in terms of the energy resolution, that is defined as:

$$R = \frac{\sigma}{E_{mean}}. \quad (2.9.5)$$

In Fig. 2.14 the energy resolution for photon of the diffuse class that convert in the front and back part of the tracker. Between the pre-launch and post-launch spatial and energy resolution change very little, see [121].

## 2.9.5 GRB sensitivity

The on ground localization of a GRB depends strongly on the spectral characteristics of the burst and on its location in the spacecraft coordinate, an estimator for the localization power as a function of the fluence is shown in Fig. 2.15. This estimate is made using the extrapolation of a Band function in the LAT energy range, if there are high energy cutoff or different spectral components the results may vary.

## 2.10 Time resolution

The evaluation of accurate arrival times of photons is essential for the study of several characteristics of GRBs and for the comparison with other instrument data, since the GRBs have shown a time variability of the order of ms, an example of the scientific relevance of this parameter see section 3.4. During pre-launch tests [207] cosmic rays were recorded to measure the time difference between two GPS systems. As shown in Fig. 2.16(a), a

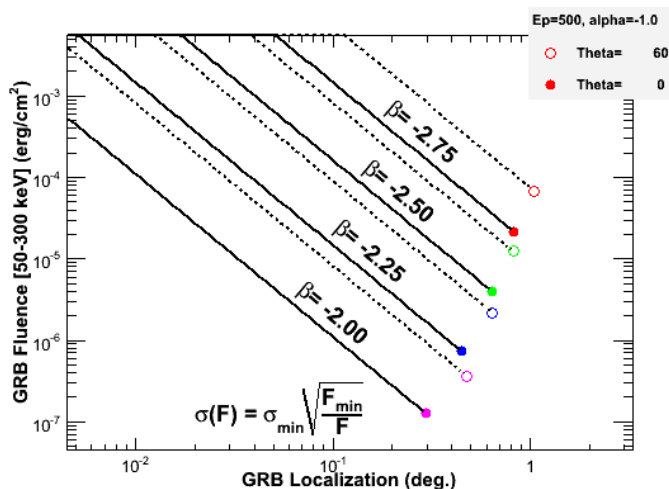


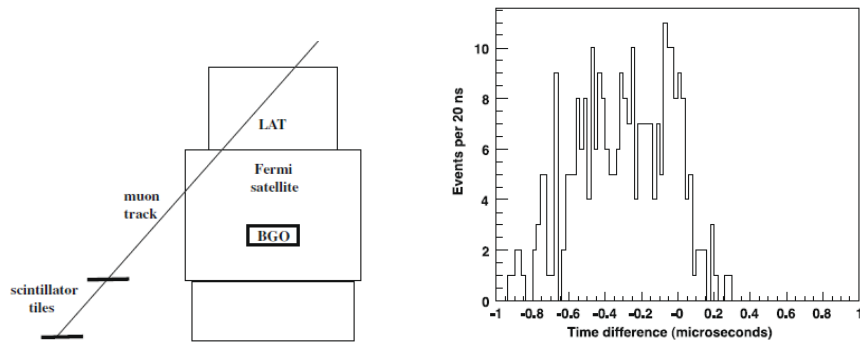
**Figure 2.15:** Each marker corresponds to a different inclination angle and a different high energy spectral index ( $\beta$ ) of a Band [15] function, (see section 1.3), and represents the minimum fluence ( $F_{min}$  in the standard 50 keV-300 keV energy band), which corresponds to a detection (y-axis) vs the 68% localization accuracy (x-axis). The solid and dotted lines are the result of the formula shown on the canvas, and they allow the computation of the localization at a given fluence (for normal incidence and for 60 degrees off-axis).

pair of scintillator tiles provided a reference for the LAT timestamps. The coincidence signal from these tiles triggered a VME-based GPS time system. Reconstructed muon tracks traversing the LAT detector were extrapolated to their impact point on the laboratory floor and their timestamps were measured with respect to the GPS of the Fermi satellite. If a muon passed through the pair of scintillators placed next to Fermi, a GPS timestamp from a standalone VME data acquisition system was also recorded. Fig. 2.16(b) shows that the LAT timestamps agreed with the reference GPS to within  $0.3\mu\text{s}$ .

On orbit, *GPS receivers* use the arrival times of reference signals from other GPS satellites to calculate their time and position and transmit that information to processors on *Fermi*. This is accompanied by an electronic *Pulse Per Second* (PPS) at the moment of validity of the timestamp word [207]. The processors, using the 20 MHz LAT system clock, maintain the PPS accuracy in the case of occasional short losses of GPS signal reception. These events are monitored with automated alarms and the Data Quality Monitor (DQM) shifter analyze the cause of this lost. The behavior of

the oscillator was extensively characterized during the ground tests. On-orbit telemetry monitoring shows that the internal spacecraft timing signals behave as before launch, from which we conclude that LAT timestamps are still well within  $1 \mu\text{s}$  of the GPS times used by the spacecraft. GPS times are maintained within 20 ns (1 sigma) of UTC [122]. On board test for the timing accuracy were done using bright gamma-ray pulsars. An integer offset in the Fermi clocks would make a large shift in observed gamma-ray phase, different for each pulsar. The rotational phase of the gamma-rays peaks of the Vela and Crab pulsars relative to the radio peak agree with that measured by previous experiment [210] and [211]. We conclude that the integer seconds of absolute time from the GPS receiver conform to Coordinated Universal Time (UTC).

Furthermore, the first gamma-ray peak of the Crab pulsar leads the radio peak by  $281 \pm 12 \pm 21 \mu\text{s}$  (the first error is statistical, the second one represents the accuracy of the radio ephemeris used for phase-folding the LAT photons) [210], in agreement with EGRET results [123]. The absolute timing accuracy is hence under  $100 \mu\text{s}$  (assuming the accuracy of the previous measurements). Finally, the peak width of PSR J0030+0451 is  $< 100 \mu\text{s}$  [212], demonstrating the stability of the LAT event times over 6 months of data-taking.



(a) Diagram of the muon scintillator telescope placed next to the Fermi satellite during pre-launch tests. (b) Histogram of time differences between the LAT system and the external stand alone VME-based GPS time system. This plots indicate an offset mean and RMS values around  $0.3 \mu\text{s}$

**Figure 2.16:** Pre launch time tests

## 2.11 Data product

The data are transferred on-ground in time contiguous *runs*, each with a few hours duration. For the transmission they could be splitted in several parts, usually 2 or 3, and then recombined on ground. Each of those runs is reprocessed on ground in the SLAC farms and a series of data product are created. The main data product are some root<sup>2</sup> file called *merit* and the *Flexible Image Transport System* (FITS) files [124]. The FITS files in an energy interval that goes from 100 MeV to 300 GeV are made public from the NASA *Fermi Science Support Center* (FSSC) website <sup>3</sup>. The FITS file are of two kinds, the ft1 contains the information on the reconstructed photons (direction, energy, point of conversion and event class), while in the ft2 the attitude of the satellite is stored. Using both this file a full analysis of the LAT data is possible. The ft2 are produced with a step of 1 second and of 30 seconds. For the study of transients source is important to use the file with the finest time sampling. In this way the exposure is evaluated using a more precise attitude of the spacecraft, the 30 s step files are used for long time observation of steady sources for reduce the memory needed for process the analysis. Weekly ft2 predicted file is also created and posted on the FSSC website, and is used when a burst is detected and the data product are not already downloaded to the ground and processed . Some non canonical analysis are done starting from the merit file, because only the photons in the three event classes are stored in the ft1 files.

When a burst is detected the satellite can be repointed, see section 2.14. During the repoint some downlinks can be missed and the data are stored in the satellite for a longer time than usual (the data can be available up to 12 hours after trigger). The telemetry data are transefered on ground on a smaller channel and more often than science data. If the burst is particularly intense it can be observed in the total number of events that pass the onboard filters, this is one of the telemetry variable. This is happen for the intense GRB090902B (see section 3.2)

---

<sup>2</sup><http://root.cern.ch/drupal/>

<sup>3</sup><http://fermi.gsfc.nasa.gov/cgi-bin/ssc/LAT/LATDataQuery.cgi>

## 2.12 Automated LAT GRB search

The research for a transient signal in LAT data, with or without external trigger from GBM (on ground also from other telescopes), is done automatically both onboard and onground. In this paragraph the used algorithms will be shortly described.

### 2.12.1 Onboard LAT Detection

The LAT flight software detects bursts, localizes them, and reports their positions to the ground through the burst alert telemetry; automated GCN circulars are sent, see 2.15. The onboard burst trigger is described in [125] and in [209]. The events that pass the onboard gamma filter are used for research onboard GRBs and are the same that are downloaded to the ground (rate  $\sim 400$  Hz). Since the algorithm needs both spatial and temporal information of the track, the rate is reduced to  $\sim 120$  Hz (the Transient event class has a rate  $\sim 2$  Hz, see paragraph 2.8). The onboard effective area is higher than the onground, so more events are used, however there is a much higher non-photon background on board than on ground see Fig. 2.11 and this strongly limits the onboard detection. The onboard track reconstruction is less precise than the onground so that the PSF is bigger and affects the onboard localizations, see Fig. 2.13. The events that have arrival times, energies and origins on the sky are feeded to the algorithm that search for statistically significant clusters in time and space. The trigger has two tiers. The first tier identifies potentially interesting event clusters for further investigation by the second tier; the threshold for the first tier allows many false tier 1 triggers that are then rejected by the second tier. The first tier operates continuously, except while the second tier code is running (600 s). A GBM, see paragraph 2.13 trigger is equivalent to a first tier trigger in that the GBM's trigger time and position are passed directly to the second tier. An improvement of the integration between the GBM and the LAT trigger was needed since the threshold was set to only 1 event in  $10^\circ$ . The updated configuration is described in [126].

### 2.12.2 LAT onground Blind Search

In order to detect burst that have not triggered any other telescope and the onboard algorithms a *blind search* [209] is performed on the event reconstructed onground. It is similar to the onboard algorithm but uses better reconstructed track and a two order of magnitude smaller background than onboard. The first stage of the this algorithm is applied to consecutive sets of 20 to 100 counts, even if they belongs to different runs. A burst is detected if it has a significance of above  $5\sigma$  and the threshold can be adjusted and further analysis (spectral and time) are performed.

## 2.13 The Fermi Gamma Ray Burst Monitor

The Fermi Gamma Ray Burst Monitor (GBM [102]) flight hardware is constituted by 12 thallium activated sodium iodide (NaI(Tl)) scintillation detectors, two bismuth germanate (BGO) scintillation detectors, a Data Processing Unit (DPU), and a Power Box. An High Speed Science Data Bus (HSSDB) is the primary channel to send GBM science data to the spacecraft for transmission to the ground. The Command and Telemetry Data Bus (CTDB) transmits commands from the spacecraft to GBM and housekeeping data from GBM to the spacecraft. The CTDB is also used to send immediate notifications of GRBs to the ground and for communications between the GBM and LAT. The pulse per second (PPS) signal provides a timing pulse to GBM every second. The immediate trigger signal provides a prompt notification to the LAT that GBM has triggered. The NaI(Tl) detectors measure the low-energy spectrum (8 keV to 1 MeV) and are used to determine the locations of GRBs. Their axes are oriented in a way that the positions of GRBs can be derived from the measured relative counting rates, a technique previously employed by Konus and BATSE. The locations and orientations of the detectors are shown in Fig. 2.17. The BGO detectors have an energy range of  $\sim 200$  keV to  $\sim 40$  MeV, overlapping at low energy with the NaI(Tl) detectors and at high energy with the LAT, thus providing for cross-calibration. They are positioned at opposite sides of the spacecraft so that any burst above the horizon will be visible to at least one of them. Each of the BGOs is read by two PMTs for a better light collection

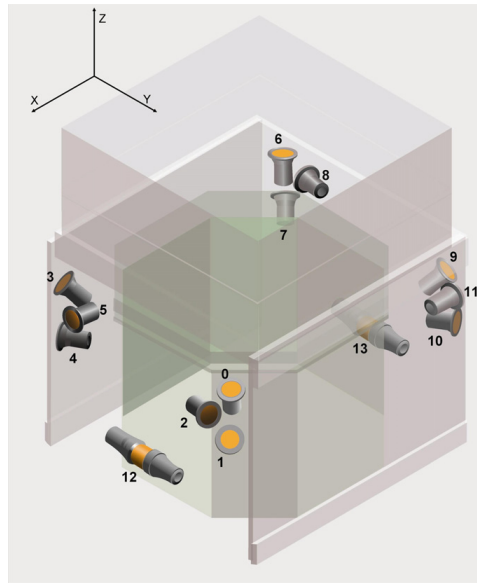


**Figure 2.17:** Locations and orientations of the GBM detectors. The NaIs are indicated with numbers from 0 to 11 while the 2 BGOs are 12 and 13. This dislocation of the detectors allows the observation of all not unocculted sky, from [102].

and for redundancy, and their signal is combined at the DPU. The signal from the detectors is digitized and three different kind of data, described in Tab. 2.3, are produced by the DPU and transmitted to the ground; each of them is suited for different analysis. Raw data are provided by the spacecraft telemetry to the ground and are processed by the *Fermi* Mission Operations Center (MOC), then they are transmitted to the *Fermi* Science Support Center (FSSC) <sup>4</sup>, where the data are available for the scientific community. The final scientific GBM data consist of continuous and burst data. Continuous data are the rates in all GBM detectors in different energy bands, regardless of whether a burst has been detected. Burst data are the counts, rates, catalog information (e.g., fluence, duration, peak flux), and ancillary data necessary for analyzing the GRB, the full list of GBM public file can be found on the FSSC website<sup>5</sup>

<sup>4</sup><http://fermi.gsfc.nasa.gov/ssc/data/>

<sup>5</sup><http://fermi.gsfc.nasa.gov/ssc/data/access/gbm/>

Name	Purpose	Temporal Resolution	Energy Resolution
CSPEC	Continuous high spectral resolution	Nominal: 4.096s During bursts: 1.024s Adjustable range: 1.024÷32.768s	128 energy channels (adjustable channel boundaries)
CTIME	Continuous high time resolution	Nominal: 0.256s During bursts: 0.064s Adjustable range: 0.064÷1.024 s	8 energy channels (adjustable channel boundaries)
TTE	Time-tagged events during bursts	2 $\mu$ s time tags for 300s after trigger; 500 K events before trigger. Max. rate, all detectors: 375 kHz.	128 energy channels (same as CSPEC)

*Table 2.3: GBM Science Data Type [102].*

### 2.13.1 GBM triggers

A GBM burst trigger occurs when the flight software detects an increase in the count rates of two or more NaI detectors above an adjustable threshold specified in units of the standard deviation in the previous interval (nominally 17 s except the 4 s closest to the trigger time). Energy ranges are confined to combinations of the eight channels of the CTIME data. A total of 120 different triggers can be specified, each with a distinct threshold. Burst triggering was enabled on 2008 July 11. There have been 404 triggers between then and 2009 March 31. In Table 2.4, the sources of these triggers as determined by ground analysis (not necessarily the classification determined by the flight software). The class “other” includes particle precipitation events, accidentals caused by statistical fluctuations in the background, Cygnus X-1 fluctuations, and events with uncertain classifications. The requirement that at least two detectors exceed threshold effectively eliminates triggers from phosphorescence spikes caused by high-Z particles [127]. The GRB trigger rate is  $\sim 260$  bursts  $yr^{-1}$ . The

Trigger Classification	Number of Triggers
Gamma-ray burst	183
SGR 1547–5488	124
SGR 1501+4516	27
SGR 1806–20	2
AXP 1E1547.0–5408	14
Solar flare	1
Terrestrial gamma flash	8
Other	45
TOTAL	404

**Table 2.4:** Burst Trigger Statistics for the Period 2008 July 11 to 2008 March 31 [102]

average onboard location error for GRBs with precisely known locations is  $9^\circ$ , consistent with prelaunch predictions.

When a burst trigger occurs, the flight software makes several changes to the data output. TTE data are rerouted from the preburst ring buffer to the spacecraft, it has a capacity of 512 k events,  $\sim 30$  s at the usual background rate. The CTIME and CSPEC integration times are decreased, nominally to 64 ms and 1.024 s, respectively. After a set time, nominally 300 s, the direct output of TTE data is terminated, and the preburst TTE buffer is dumped and restarted. Accelerated CTIME and CSPEC data rates continue for an additional time, nominally 600 s after the trigger. At the nominal telemetry settings for CTIME and CSPEC data, GBM generates  $\sim 1.2$  Gbits of data per day, plus a variable amount for each burst trigger. A burst generates between 0.3 and 0.5 Gbits of data, comprising mainly 300 s of background TTE data.

### 2.13.2 GBM locations

When a burst trigger occurs, onboard software determines a direction to the source using the relative rates in the 12 NaI detectors. These rates are compared to a table of calculated relative rates for each of the 1634 directions ( $\sim 5^\circ$  resolution) in spacecraft coordinates. The location with the best  $\chi^2$

fit is converted into right ascension and declination using spacecraft attitude information and transmitted to the ground as TRIGDAT data, using a real-time communication channel, opened when a trigger happens.

Improved locations are automatically computed on the ground in near real-time by the Burst Alert Processor (BAP) using three different precalculated tables, for soft, typical and hard GRB spectra. Both of these location types are promptly transmitted the Gamma-ray bursts Coordinate Network (GCN) as automatic Notices, see paragraph 2.15. The high-priority telemetry is also processed by humans, to produce locations based on a more careful selection of source and background time intervals. These locations, often called human in the loop (hitl) locations, are published via the GCN as human-written Circulars, after a delay of tens of minutes to a day or more, with some relevant preliminary spectral information. If the burst is also detected by the LAT often it is jointly written. The on ground and hitl locations are reported with a statistical only error to which an additional systematical error should be added. This value was preliminary evaluated about  $\sim 2^\circ \div 3^\circ$ . The result of a Bayesian analysis of a sample of GRBs with other enhanced locations, from the LAT or other satellite or on ground telescope for the hitl locations is  $\sigma_{sys} = 3.8^\circ \pm 0.5^\circ$ , [128].

### 2.13.3 GBM response function

Analysis of GBM data [102] products is fundamentally a process of hypothesis testing wherein trial source spectra and locations are converted to predicted detector count histograms, that are statistically compared to the observed data. A process usually called *forward folding*, the official tool is RMFIT<sup>6</sup> and the minimizing function is the Cash Statistics [129] (see section 4 for more details). The key element in the conversion process is the representation of the composite GBM instrument response function, that is detailed and accurate. It is collected in the form of Detector Response Matrices (DRMs) for all individual GBM detectors. The DRMs, which contain the multivariate effective detection area, include the effects of angular dependence of the detector efficiency, partial energy deposition

---

<sup>6</sup>[http://fermi.gsfc.nasa.gov/ssc/data/analysis/user/FGST-rmfit\\_ver33pr7.tar.gz](http://fermi.gsfc.nasa.gov/ssc/data/analysis/user/FGST-rmfit_ver33pr7.tar.gz)

in the detector, energy dispersion and nonlinearity of the detector, and atmospheric and spacecraft scattering (and shadowing) of photons into the detector. They are therefore functions of photon energy, measured (deposited) energy, the direction to the source with respect to the spacecraft, and the orientation of the spacecraft with respect to the Earth. The DRMs are generated using the General Response Simulation System (GRESS), a simulation and modeling code based on the GEANT4 Monte Carlo radiation transport simulation toolkit [116]. The GRESS code and models were extensively validated against data from radioactive source calibration of individual GBM detectors as well as data from a radioactive source survey of the integrated Fermi spacecraft (see reference in [102]). In practice, the multivariate GBM DRMs are separated into two components for GRESS computation efficiency. The first component includes the energy and angular dependent response of detectors with the Fermi spacecraft. It is stored in a large data set called the direct response database. The second component includes the effects of photons scattering in Earth’s atmosphere as a function of energy and source-Earth spacecraft geometry. It is stored in a large data set called the atmospheric response database. In the data analysis process, these two components are combined together for a specific set of observing conditions to form the composite set of DRMs. A set of composite DRMs is provided as a standard data product for each GBM trigger, together with the fits data file described in Table 2.3.

## 2.14 Fermi Orbital characteristics

### 2.14.1 Operational (LAT) mode: Survey, Maneuver and ARR

To take full advantage of the LAT’s large FOV, the primary observing mode of Fermi is the so-called *scanning* mode in which the normal to the front of the instrument (z-axis or LAT boresight) and the Earth zenith angle form a fixed angle, called *rocking angle*. In order to cover the full sky, each orbit the satellite observes alternatively the two half of the sky. From the start of the mission the rocking angle was  $35^\circ$ ; it was changed a few times and now is  $50^\circ$  to decrease the batteries temperature and increase their duration. After two orbits, that is about 3 hr for Fermi’s orbit at  $\sim 565$

km and  $25.5^\circ$  inclination, the sky exposure is almost uniform. Fig. 2.18 illustrates the sensitivity and FoV achieved with the LAT for exposures on various timescales. For particularly interesting targets of opportunity, the observatory can be inertially pointed. This repointing can be decided on ground and are called *Target Of Opportunity* (TOO) or the onboard software can decide the repointing to follow a new transient source, e.g. a GRB; this is called *Automatic Repoint Request* (ARR) and lasts totally 5 hours. The trigger for an ARR can be issued, also, on request of GBM if the transient has a particularly high peak flux or fluence (flux x time duration) as can be seen in paragraph 2.13. Automatically the spacecraft tries to put the new transient few degrees to the center of the FOV where the Effective Area is larger. The ARR has to keep the Earth limb and the Earth outside the FOV, so if this is not possible the spacecraft returns temporarily in *scanning* mode, repointing again when this condition is satisfied. More informations on operating modes can be found on the FSSC website <sup>7</sup> **other parameters on ARR can be found and added** Up to half of the 2010 there have been just two TOO that lasted several hours (**this numbers be rechecked**), while there have been 49 ARR (from August 2008 to August 2010), the pointing history of the satellite is posted in the FSSC website<sup>8</sup>. The threshold of the ARR have been adjusted to improve the selection of possible burst detectable by the LAT. Several change in the orbital parameters have been done for improve the observation and reduce the background contamination and from the launch the orbital *overshot* at each manouver was reduced.

### 2.14.2 South Atlantic Anomaly

The orbit of Fermi intersects the Earth's inner radiation belt in a region that is known as the South Atlantic Anomaly (SAA). In this region there are geomagnetically trapped protons with energies up to hundreds of MeV and electrons with energies up to tens of MeV. The flux of protons and electrons in the LAT energy range reach levels which are several orders of magnitude above those of primary cosmic rays. The tracker electronics saturate due

<sup>7</sup>[http://fermi.gsfc.nasa.gov/ssc/proposals/pointing\\_analysis/](http://fermi.gsfc.nasa.gov/ssc/proposals/pointing_analysis/)

<sup>8</sup><http://fermi.gsfc.nasa.gov/ssc/observations/timeline/posting/>

to this extreme particle flux, hampering the scientific observations. The continuous influx of particles generate high current in the ACD PMTs; this would lead to their rapid deterioration unless their bias voltage is lowered in this part of the orbit. Therefore, during SAA passages, triggering, recording and transmission of science data are stopped and only LAT housekeeping data are recorded and transmitted to the ground. The position along the orbit defined by the GPS receiver aboard the Fermi spacecraft determines the transition between nominal science operations and the SAA transit mode. The latitude and longitude of the Fermi position are compared to the bounds of a polygon defined by 12 latitude–longitude vertices stored in the spacecraft memory. As the spacecraft position crosses this polygonal boundary the SAA transit mode is triggered. To avoid multiple entries and exits during a single orbit, a convex polygon is used to define the SAA region. Before the launch a conservative definition for the SAA polygon was used, based on other spacecraft data and theoretical models; this definition resulted in a loss of observation time of about 17%. When the on orbit diagnostic data of the LAT were available the size of the polygon was refined [207].

Even though science triggers are disabled during SAA passages, fast trigger signals remain operational. Special TKR and ACD counters can sample the rate of fast trigger signals to determine position-dependent rates of the LAT along the orbit. Fig. 2.19 shows the rates recorded in the TKR counters versus spacecraft position [207]. A cross-check during nominal science operations is performed with the ACD trigger signal counters. There is no significant increase in the rate of ACD fast trigger signals as Fermi approaches the SAA boundary, thus validating the optimized polygon. Since the SAA moves at a rate of a few tenths of a degree per year and its size and particle fluxes vary with the solar cycle, there will be other updates to the SAA boundary [207].

## 2.15 GCN system

Since the GRBs emit in several wavelength it's fundamental in order to understand the underlying physic the use of several different telescope,

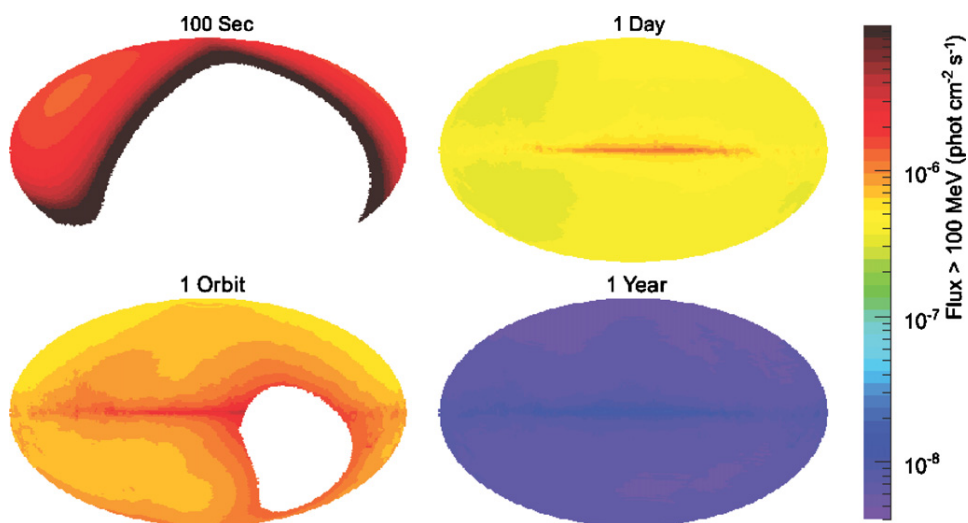


**Figure 2.18:** LAT source sensitivity for exposures on various timescales. Each map is an Aitoff projection in galactic coordinates. In standard sky-survey mode, nearly uniform exposure is achieved every two orbits, with every region viewed for  $\sim 30$  minutes every 3 hr. This are made for a rocking angle of 35 degrees, from [101].

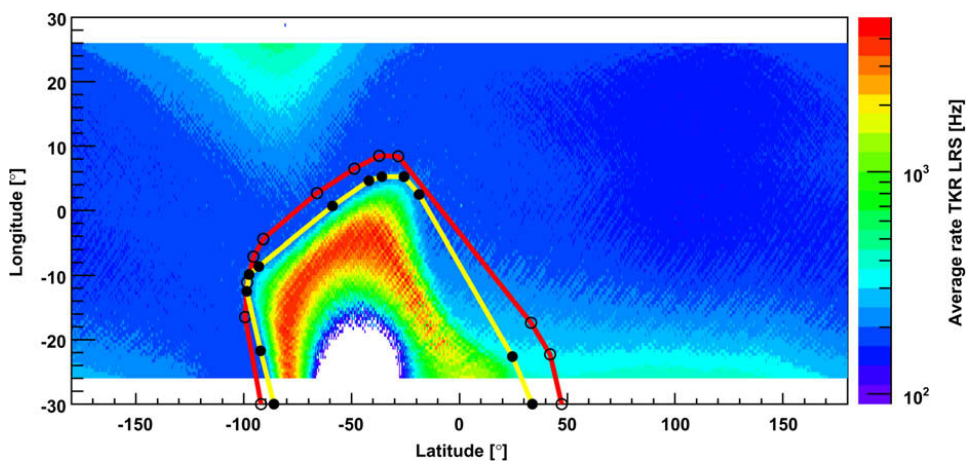


**Figure 2.19:** Average rate of TKR counters obtained during 26.6 days of LAT nominal science operations versus geographic latitude and longitude. Superimposed are the prelaunch SAA boundary (red) used during the initial phase of the mission, and the updated SAA boundary (yellow) derived from measurements of the TKR counter data. A rate increase is visible at the edges of the SAA before the TKR electronics saturates and suppresses fast trigger signals, thus bringing the count rates to zero [207]. The updated polygon (yellow) reduced the loss in observation time to approximately 13% of the total on-orbit time. This polygon has been the default for the LAT operations since July 28, 2008.

on ground and on space. Since their duration goes from few minutes to a few hours, it's important to transfer the spectral informations and the locations between different telescope as fast as possible. The Gamma-ray bursts Coordinates Network (GCN)[130] distributes information from the telescopes to the scientific community, in a fast and preliminary way. Each burst take the name of the day in which it happen in the format YYMMDD and at the end it's appendend a letter (A for the first, B for the second and so on). Before the 1st of January 2010 the fist burst of the day has not an A at the end. There are three major parts to GCN:

1. the *Notices* distributes GRB/Transient position messages via email or sockets in real-time from different space telescopes as Fermi LAT , Fermi GBM, Swift, AGILE, INTEGRAL and others.
2. the *Circulars* distributes prose-style messages about follow-up observation in several wavelength (optical, radio, x-ray and gamma-ray) with also refined locations obtained not only in automatic way.
3. the *Reports* distributes final reports on each burst by a follow-up observing team.

Lately [126] there was a change in the onboard triggering algorithm, that was optimized for the research also of the extended emission, characteristic highlited for the *Fermi* LAT bursts, see section 3.1. The LAT onboards automated notices, generated by the on board software, are following this change and we thus expect this new configuration to provide onboard detections of 3-5 GRB/year, with localizations in the range 0.1 to 0.5 degrees. The table of all the LAT detected burst and corresponding circular is on th FSSC page<sup>9</sup>.

---

<sup>9</sup>[http://fermi.gsfc.nasa.gov/ssc/observations/types/grbs/grb\\_table/](http://fermi.gsfc.nasa.gov/ssc/observations/types/grbs/grb_table/)



## Chapter 3

# GRBs observed by *Fermi*

### 3.1 Observed characteristics

Until November 2010 21 GRBs have been detected and reported through notices by the LAT. In the following their main characteristics will be described, they are summarized in table 3.1. The skymap with the GRBs location is in Fig. 3.1. The adjoined table can be found on the Fermi Science Support Center (FSSC) website <sup>1</sup>, with the full reference list.

During its first 1.5 yr of routine operation, from Aug. 2008 to Jan. 2010, the LAT has detected 14 GRBs, corresponding to a detection rate of  $\sim 9.3\text{yr}^{-1}$ . While at least 13 of the 14 LAT GRBs had  $\geq 10$  photons above 100 MeV, 4 were particularly bright in the LAT with  $\geq 1$  photon above 10 GeV,  $\geq 10$  photons above 1 GeV, and  $\geq 100$  photons above 100 MeV. This corresponds to a bright LAT GRB (as defined above) detection rate of  $\sim 2.7$  GRB/yr (with a rather large uncertainty due to the small number statistics). There were also 11 GRBs with  $\geq 1$  photon above 1 GeV, corresponding to  $\sim 7.3$  GRB/yr. These detection rates are compatible with pre-launch expectations [209] based on a sample of bright BATSE GRBs for which the fit to a Band spectrum over the BATSE energy range (20 keV to 2 MeV) was extrapolated into the LAT energy range, see Fig. 3.2. The agreement is slightly better when excluding cases with a rising  $\nu F_\nu$  spectrum at high energies (i.e. a high-energy photon index  $\beta > -2$ , this rise could be an artifact of the BATSE fit [131]). This suggests that, on average, there is no significant excess or deficit of high-energy emission in the LAT energy range

---

<sup>1</sup>[http://fermi.gsfc.nasa.gov/ssc/resources/observations/grbs/grb\\_table/](http://fermi.gsfc.nasa.gov/ssc/resources/observations/grbs/grb_table/)

GRB	Angle from LAT	Duration (or class)	# of events > 100 MeV	# of events > 1 GeV	Delayed HE onset	Long-lived HE emission	Extra spectral comp.	Highest photon Energy	Redshift
080825C	$\sim 60^\circ$	long	$\sim 10$	0	?	yes	no	$\sim 600$ MeV	-
080916C	$49^\circ$	long	145	14	yes	yes	?	$\sim 13.2$ GeV	$\sim 4.35$
081024B	$21^\circ$	short	$\sim 10$	2	yes	yes	?	3 GeV	-
081215A	$\sim 86^\circ$	long	-	-	-	-	-	-	-
090217	$\sim 34^\circ$	long	$\sim 10$	0	no	no	no	$\sim 1$ GeV	-
090323	$\sim 55^\circ$	long	$\sim 20$	$> 0$	?	yes	?	-	3.57
090328	$\sim 64^\circ$	long	$\sim 20$	$> 0$	?	yes	?	-	0.736
090510	$\sim 14^\circ$	short	$> 150$	$> 20$	yes	yes	yes	$\sim 31$ GeV	0.903
090626	$\sim 15^\circ$	long	$\sim 20$	$> 0$	?	yes	?	-	-
090902B	$\sim 51^\circ$	long	$\sim 200$	$> 30$	yes	yes	yes	$\sim 33$ GeV	1.822
090926	$\sim 52^\circ$	long	$> 150$	$> 50$	yes	yes	yes	$\sim 20$ GeV	2.1062
091003A	$\sim 13^\circ$	long	$\sim 20$	$> 0$	?	?	?	-	0.8969
091031	$\sim 22^\circ$	long	$\sim 20$	$> 0$	?	?	?	$\sim 1.2$ GeV	-
100116A	$\sim 29^\circ$	long	$\sim 10$	3	?	?	?	$\sim 2.2$ GeV	-
100225A	$\sim 60^\circ$	long	$\lesssim 10$	0	?	?	?	-	-
100325A	$\sim 9.2^\circ$	long	$\sim 4$	0	?	?	?	-	-
100414A	$\sim 70^\circ$	long	$\sim 20$	-	?	yes	?	$\sim 4$ GeV	1.368
100707A	$\sim 90^\circ$	long	-	-	?	?	?	-	-
100724B	$\sim 49^\circ$	long	-	-	?	?	?	-	-
100826A	$\sim 70^\circ$	long	-	-	?	?	?	-	-
101014A	$\sim 54^\circ$	long	-	-	?	?	?	-	-

**Table 3.1:** GRB 100225A [294], 100325A [295] have a significance of  $\gtrsim 4\sigma$ . GRB 100707A, 100724B, 100826A and 101014A are detected and analyzed at a large angle using a non standard event selections. For the not yet published papers those peaces of informations are taken from the GCNs and are preliminary.

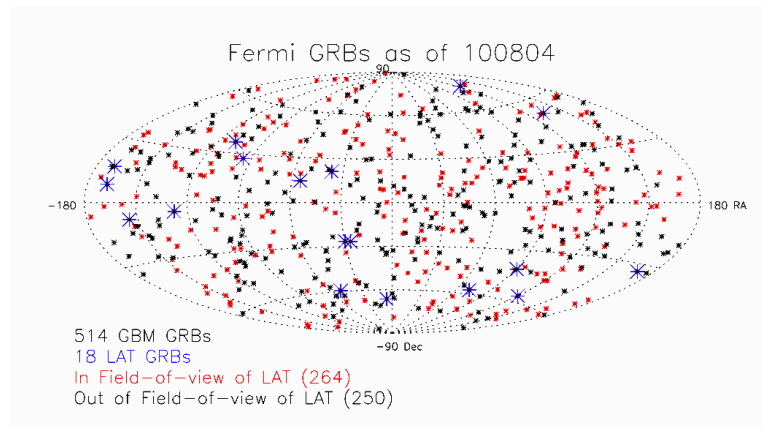


**Figure 3.1:** Skymap of the Fermi observed GRBs up to 4th of August 2010.

relative to such an extrapolation from lower energies.

From January until now only the GRB100414 [132] is observed with more than 10 photons above 100 MeV (in this statistics are not considered the burst detected with not standard technique or significance not clearly above  $5\sigma$ ) and few photons above 1 GeV. The previous values (also reported in Fig. 3.2) evaluated for 2 years (instead than 1.5) of operations (until August 2010) are: 15 GRBs with  $\geq 10$  photons above 100 MeV (7.5 GRB/yr), 12 with  $\geq 1$  photons above 1 GeV (6 GRB/yr) while there are still only 4 burst that pass the other 3 selections and the rates become 2. GRB/yr. All these value are well inside the error bars of the values shown in Fig. 3.2. A sistematic study of bright GRBs detected by the GBM in the LAT FoV but not observed by the LAT is in preparation.

Another summary of the *Fermi* LAT observation can be found in [133] and in [131], while the *Fermi* LAT collaboration GRB catalog are in preparation. There are other catalogs and studies of LAT burst as [134] and [135]. An analysis [136] of the whole dataset was also independently performed, searching for undetected GRB, they have found a possible significant emission in coincidence of GRB 090228A.

In the following three sections the main characteristics of GRBs, that the LAT has observed in this two years of operations, are summarized. Given the differences and the interesting results from each burst, in the last part of the chapter, the main characteristics of the GRBs that I have analyzed and

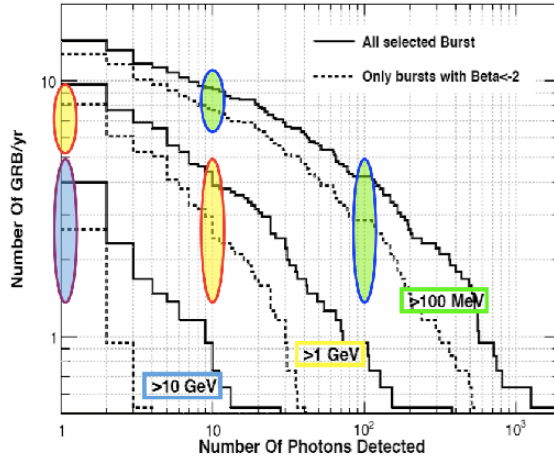


**Figure 3.2:** LAT GRB detection rates in 1.5 (color ellipses) superposed on top of pre-launch expected rates based on the extrapolation of a Band spectrum fit from the BATSE energy range [209]. The ellipses inner color indicates the minimal photon energy (green, yellow and cyan correspond to 0.1, 1 and 10 GeV, respectively), while their height indicates the uncertainty ( $\pm\sqrt{N}/1.5\text{yr}$ ) on the corresponding LAT detection rate ( $N/1.5\text{ yr}$ ) due to the small number ( $N$ ) of detected GRBs. Taken from [131].

studied in more details are described. In the last chapter the preliminary analysis of GRB091003A are shown with several information, since until now few results are available for this burst in literature, that has shown some interesting characteristics.

### 3.1.1 Delayed onset of the high energy emission

The first unexpected result brought by the Fermi GRB observations is the delayed onset of high energy emission. This was for the first time evident in the light curve of bright long GRB 080916C [213] where the first bright peak seen in low-energy GBM light curves was not observed in high-energy LAT. This feature is clearly seen for 5 LAT GRBs both long (GRB 080916C [213], 090902B [214] and 090926A [137]) and short (GRB081024B [215] and GRB090510 [216]). Many models have been proposed to explain this delayed onset. In the leptonic scenario, different emission region between low and high-energy emission is required to explain the delay and the possible coincidence of the following peak [213]. In the framework of the internal-shocks model for the prompt emission of GRBs [138], where intermittent winds of relativistic plasma are ejected by a newly formed black hole and

collide to form shocks and accelerate particles, where the two emission regions could arise from two different pairs of colliding shells, with variations in physical conditions leading to nonthermal electrons with different spectral hardnesses. An alternative explanation [213] is that a surrounding volume becomes filled with radiation that attenuates the high-energy photons until a later time when the emitting region expands and becomes optically thin. A  $\gamma\gamma$  pair-production opacity effect would, however, produce a high-energy spectral softening or cutoff that is not observed since the joint GRB/LAT fit are in good agreement with the Band function. Moreover, internal  $\gamma$ -ray opacity models predict that high energy photons should also be detected in the rising portion of the GBM emission while they can still escape the source, before the increased photon density attenuates the  $\gamma$ -rays [139]. An other possibility is that the prompt emission consists of two components: one is the emission component peaking at  $\sim 1$  MeV due to the synchrotron-self-Compton radiation of electrons accelerated in the internal shock of the jet and the other is the component peaking around 100 MeV due to inverse Compton up-scattering of the photospheric X-ray emission of the expanding cocoon (the optically thin the hot bubble produced by dissipation of the jet energy inside the progenitor star) off the same electrons in the jet [140], this model is sometimes referred as External Inverse Compton (EIC). The same authors in [141] refer that some of the parameters used may seem not common. In [141] they suggest that the difference of the delay timescales of long and short GRBs might be due to the differences in their progenitors.

For the hadronic origin, the time delay could be a consequence of the time needed to accelerate protons or ions to energies where they can radiate by photopion or proton synchrotron radiation and generate an electromagnetic cascade [142] [143]. If the high energy emission is related to the afterglow (external shock)[144] [134] this could explain naturally this delayed onset. The delayed onset feature could be an important hint for the information of relativistic jet as well as the gamma-ray emission mechanism of GRBs.

### 3.1.2 Extra spectral component

Fermi detected distinct spectral component from three GRBs above the Band function [15], including both short (GRB 090510) and long duration

GRBs (GRB 090902B and 090926A). GRB 090510 is the first case of the significant detection of extra component with Fermi observations. The extra power-law component with photon index of  $-1.62 \pm 0.03$  is required for more than  $5 \sigma$  significance compared with single canonical Band function[216]. The power-law component appears to extrapolate to energies well below  $E_{peak}$  and dominates the Band function emission below  $\approx 20$  keV, similar to the behavior seen in GRB 090902B, see the following paragraph. For GRB 090926A[137] the extra power law component gives an improvement to the fit of over  $\sim 10\sigma$  ( $\Delta C - STAT = 107.3$ ). The power-law photon component dominates above 100 MeV and it has a photon index  $\lambda = -1.80 \pm 0.01$ . A further improvement is obtained with an exponential cut-off ( $E_{pivot} = 1$  GeV) at a  $\sim 6\sigma$  level ( $\Delta C - STAT = 39.5$ ). The preliminary [137] folding energy is  $E_{fold} = 1.41_{-0.42}^{+0.22}(stat.) \pm 0.30(syst.)$  GeV, with the power-law photon index below the cutoff energy is  $\lambda = -1.72_{-0.02}^{+0.10}(stat.) \pm 0.01(syst.)$ . This is the first time that a cut-off gives rise a significant improvement to the fit. For some theoretical interpretation on the extra component see section 3.2.

In other burst LAT bursts the significance of different spectral component other than the Band function are not significant above  $5\sigma$ . In GRB080916C [213] the additional power law component was not significant enough. The probability, that there was no additional spectral component, is of 1% in the fourth time bin where there are three photons above 6 GeV. In the first time bin (2.7s) of GRB080825C [217] a significance of  $4.3 \sigma$  was found for an exponential cutoff with a cutoff energy around  $E_{fold} = 1.77_{-0.56}^{+1.59}$  MeV. With a  $\pm 15\%$  variation in the BGO effective area the significance becomes  $\sim 3.7\sigma$ .

### 3.1.3 Long lived high-energy emission

*Fermi* also confirmed that the high-energy emission is observed longer time than low energy emission in almost all LAT GRBs. In the case of GRB 090510, fortunately, a simultaneous observation between Fermi and Swift was performed, and we found that the high-energy emission of the LAT is detected until when Swift/XRT observation started [218]. Furthermore, the decay profile of high-energy emission is similar to that of

X-ray afterglow. Future Fermi/Swift joint observation will provide more samples and relation between high-energy emission and afterglow will be revealed. Two GRB in March 2009 (GRB 090323 and GRB 090328) have shown a very long duration emission up to several kilo-seconds[145]. In both cases, an Autonomous Repoint Request allowed the afterglow emission to be monitored for 5 hours. The origin of the long lasting GeV afterglow after the prompt emission phase is unclear. If it is from the external forward shock, one needs to introduce abnormal shock parameters, and to argue for coincidence to connect with the internal-origin early GeV emission to form a simple PL decay lightcurve. Alternatively, the long lasting GeV emission can be also of the internal origin.

Delayed onset, long-lived emission, and extra power-law component as described above have been detected from several LAT GRBs and some of them might be a common feature of the high-energy emission of GRBs for both short and long GRBs. However, a few LAT GRBs, such as GRB 090217 do not show any special features in high-energy emission (e.g., single Band function, no delay and no long-lived emission)[219]. Future Fermi GRB observations will increase the sample number of GRBs with high-energy emission and such systematic study will help us to investigate the high-energy gamma-ray emission mechanism of GRBs

## 3.2 GRB090902B

### 3.2.1 Detection and Observation

On 2009 September 2 at 11:05:08.31 UT ( $T_0$ ) the *Fermi* GBM localized the GRB090902B (trigger 273582310/090902462) [146]. This burst was within the LAT field of view (FoV), initially, with an angle of  $51^\circ$  deg from the *Fermi* boresight. This burst was sufficiently bright in the GBM that an ARR (see section 2.14) was issued and the spacecraft began slewing within 10 s towards the burst. After  $\sim 200$  s the boresight of the LAT was within few degrees from the final localization. *Fermi* maintained that pointing until  $\sim 1$  ks after the trigger, when the Earth's limb was starting to enter the LAT FoV. This burst was detected up to an energy of  $\sim 5$  MeV by the GBM, and the emission was significantly detected by the LAT, with 39

photons above 1 GeV [296]. The highest energy photon had  $E = 33.4_{-3.5}^{+2.7}$  GeV and arrived 82 seconds after the trigger. This is until now still the highest energy photon ever detected by a GRB. A Monte Carlo simulation was generated to evaluate if this photon is associated to this bursts and the errors on the estimated energy. Preliminary analysis detected photons as late as 300 s after the trigger [297]. The observation and the analysis are extensively reported in [214] [299].

From the LAT data, the burst was localized to R.A.(J2000), Dec(J2000)=265.00°, 27.33° with a statistical uncertainty of 0.04° (+ < 0.1° systematic) [296], enabling Target of Opportunity observation to begin at 23:36 UT ( $\sim 12.5$  h after  $T_0$ ) [147] with the narrow field instrument on *Swift*. The afterglow was discovered in both the XRT 0.3-10 keV energy range and UVOT u-band and was confirmed to be fading [147]. The first ground-based optical observations were obtained by ROTSE-IIIa  $\sim 1.4$  hours post trigger [148]. The prompt part of the burst was observed also by *Suzaku* WAM [149] and INTEGRAL SPI-ACS [146]. Other detection were reported in the optical [150], in the near infrared [151] and in the radio [152] and [153]. The afterglow redshift of  $z=1.822$  was measured by the GMOS spectrograph mounted on the Gemini-North telescope [154].

### 3.2.2 Spectral characteristics

In the Fig. 3.3 the light curves of GBM and LAT are shown in different energy bands. The first three panels show the data from the most brightly illuminated NaI and BGO detectors of the GBM and the bottom three panels show the LAT data with various event selection. Detailed analysis of the GBM data for energies 50-300 keV yields a formal  $T_{90}$  duration of 21.9 s starting at  $T_0 + 2.2$  s, the LAT detects emission from this GRB as late as 1 ks after the trigger and the first high energy peak is at  $T_0 + 9$  s.

The spectral analysis of the prompt phase was performed using the GBM and LAT data together in different time bins and in the whole interval. The time integrated spectrum of this GRB is best modeled by a Band function and a power-law component, the evidence of this distinct spectral component was already noticed in the second GBM-LAT circular [297]. The power-law component significantly improves the fit between 8 keV and 200 GeV in

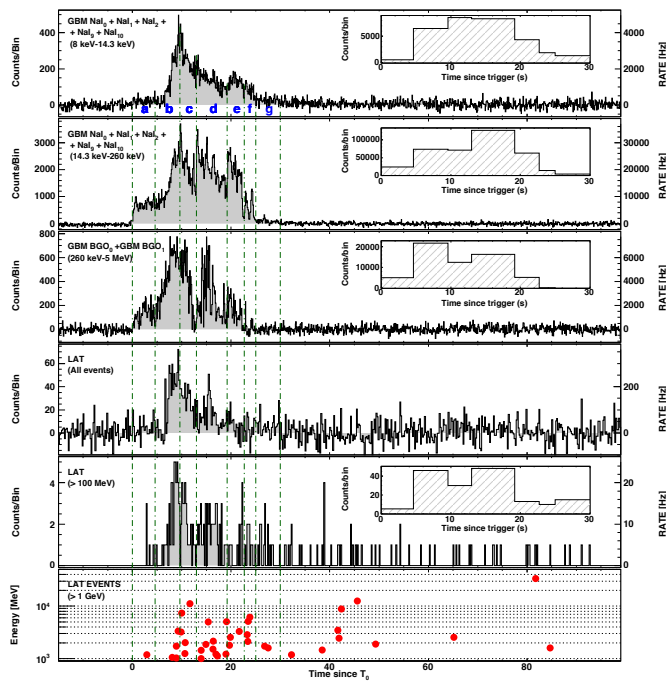


**Figure 3.3:** Light curve of the GRB 090902B. The data from the GBM NaI detectors were divided into soft (8–14.3 keV) and hard (14.3–260 keV) bands in order to reveal any obvious similarities between the light curve at the lowest energies and that of the LAT data. The fourth panel shows all LAT events that pass the on-board gamma filter, while the fifth and sixth panels show data for the transient class event selection for energies  $> 100$  MeV and  $> 1$  GeV, respectively. The vertical lines indicate the boundaries of the intervals used for the time-resolved spectral analysis. Those time boundaries are at  $T_0 + (0, 4.6, 9.6, 13.0, 19.2, 22.7, 25.0, 30.0)$  s. The insets show the counts for the corresponding data set binned using these intervals in order to illustrate the relative numbers of counts considered in each spectral fit. Taken from [214]

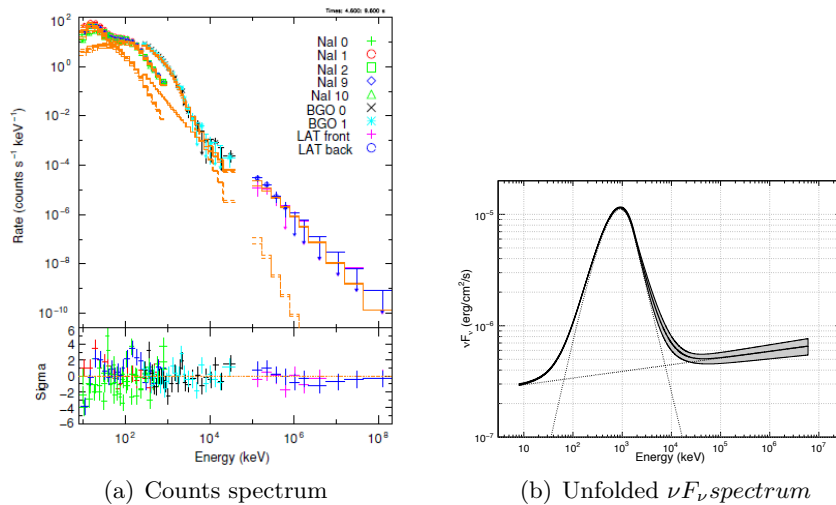


**Figure 3.4:** Fit of the second bin ( $T_0 + 4.6s, T_0 + 9.6s$ ). Taken from [214]

both the time-integrated spectrum and in the fits of each time interval, where there is sufficient statistic. Using only all the GBM data (8 keV-40 MeV), this component is also required, it can be neglected only excluding the GBM data below  $\sim 50$  keV. In [214] we conclude that this power-law component contributes to a significant part of the emission both at low ( $< 50$  keV) and high ( $> 100$  MeV) energies. In Fig.3.4 there are the counts spectrum and the unfolded  $\nu F_\nu$  spectra for a Band function with a power-law component fit to the data for interval  $T_0 + 4.6s - T_0 + 9.6s$  when the low energy excess is most significant. The spectral evolution in the prompt phase is shown in Fig. 3.5. A possible cutoff is observed in the second time bin, being the improvement at  $3\sigma$  level, and indicates weak evidence for a cutoff in the second component, placing a lower limit on the cutoff energy in this interval of about 1 GeV. In the joint analysis of the fifth and sixth interval an equally good fit is obtained with an exponential cutoff at high energies, with the preferred cutoff energy lying above 2 GeV.

The spectrum of the extended emission observed by the LAT is consistent with a power-law with photon index  $\Gamma = -2.1 \pm 0.1$  and its flux, above 100 MeV, declines as  $t^{-1.5 \pm 0.1}$  over the interval ( $T_0 + 25 s, T_0 + 1000 s$ ). The upper limit at times  $> T_0 + 3600 s$  was derived from the data collected after the source emerged from occultation by the Earth and it is compatible with

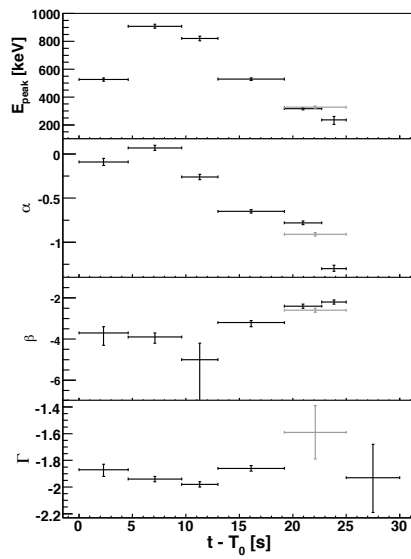


**Figure 3.5:** Spectral evolution. The  $E_{peak}$  value of the Band function change throughout the burst, while  $\beta$  remains soft until the fifth interval when it hardens significantly and remains hard in the following bin. In the last time bin the Band function component is no longer detected. The hardening of  $\beta$  is accompanied by an apparent hardening of the power-law index,  $\Gamma$ , which until the fifth interval does not exhibit much variation. However, this is not definitive since the flux is too low to constrain  $\Gamma$  in the fifth and sixth intervals separately. A spectral fit (this values are indicated with gray points) of the sum of these two intervals confirms the presence of both a harder  $\beta$  and a harder  $\Gamma$ , with a clear statistical preference for the inclusion of the power-law component. The value are taken from the [214]

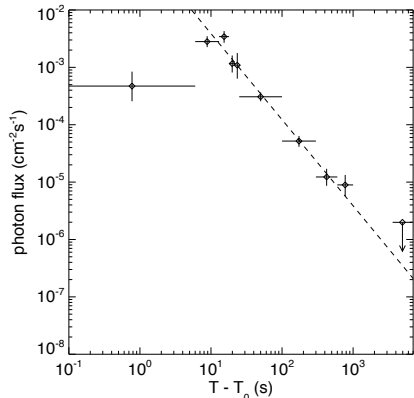


**Figure 3.6:** Light curve of GRB 090902B for energies 0.1–300 GeV from unbinned likelihood fits to the LAT data. After the prompt phase, extended or afterglow emission consistent with a temporal profile  $\propto t^{-1.5}$  (dashed line) lasts until  $\sim T_0 + 1000$  s. The upper limit at times  $> T_0 + 3600$  s was derived from the data collected after the source emerged from occultation by the Earth. From [214]

the extrapolation of the flux decline (see [214]). We note that the temporal decay index measured by XRT in the X-rays at latter time ( $T_0 + 12.5$  h,  $T_0 + 17$  d) is  $-1.38 \pm 0.06$  (90% C.L.) [147].

The total fluence of GRB090902B in the prompt phase is  $(4.36 \pm 0.06) \times 10^{-4}$  erg  $cm^{-2}$  (10 keV–10 GeV) that gives an  $E_{iso} = (3.63 \pm 0.05) \times 10^{54}$  ergs, comparable to that of GRB080916C [213].

### 3.2.3 Theoretical analysis

From the observation of a  $11.16_{-0.58}^{+1.48}$  GeV photon in third interval (the highest energy photon during the prompt in phase), we derive a minimum value of the bulk Lorentz factor ( $\Gamma_{min}$ )  $\approx 1000$  using the flux variability time scale of  $t_v \approx 53$  ms found in the BGO data. This limit follows from the constraint that the opacity for  $e^\pm$  pair production with target photons fitted by the Band+PL model in the third interval is less than unity for the 11.16 GeV photon (see [155]). This high  $\Gamma_{min}$  value is of the same order of the values derived with the same technique for GRB 080916C [213] and GRB 090510 [216].

The *Fermi* data for GRB090902B show for the first time clear evidence of excess emission both at low energies ( $\lesssim 50$  keV) and at high energies ( $> 100$  MeV), while the Band function alone fits data at intermediate energies

adequately. These excess are well fit by a single power-law component suggesting a common origin. This power-law component accounts for the  $\approx 24\%$  of the total fluence in the 10 keV-10 GeV range, and its photon index is hard, with a value of  $\sim -1.9$  through most of the prompt phase. Those spectral characteristics and the delayed onset of the  $\approx 100$  MeV emission are hard to be reconciled with the simplest version of lepton synchrotron self-Compton mechanism (SSC) [214]. The peak of the SSC emission is expected to have a much higher energy than the synchrotron peak at MeV energies, and the SSC component has a soft tail that is well below the synchrotron flux at lower energies and so would not produce excess emission below  $\sim 50$  keV. Hadronic models, either in the form of proton synchrotron radiation [142] or photohadronic interactions ([156] and applied to GRB090510 [143]), can produce a hard component with a similar low energy excess via direct and cascade radiation (e.g., synchrotron emission by secondary pairs at low energies). However, the total energy release in hadronic models would exceed the observed gamma-ray energy of  $E_{iso}$  significantly and may pose a challenge for the total energy budget, the collimation into a narrow jet may alleviate the energy requirements.

A different analysis and interpretation of this burst in [206] suggests that the prompt burst spectrum is consistent with emission from the jet photosphere combined with non-thermal emission described by a power-law. The photospheric emission gives rise to a strong quasi-black body spectrum described as a phenomenological multicolor blackbody. These results were obtained using smaller time bins ( $\sim 1$ s requiring a (S/N) of 40 in the NaI 1, the most strongly illuminated GBM detector) than in the [214] analysis. This can suggest that the observed Band plus power-law spectra can be the time super position of several blackbody function with different temperature. The thermal and non thermal component are strongly correlated with a lag of 0.5s, that is interpreted as a delay between the photospheric emission and the non thermal emission (synchrotron) emitted further from the central engine. In [135] a similar analysis with different time bins is reported with similar results and a time evolution of the blackbody temperature. More informations on this models are in [157] and [158] where the not thermal component is associated to the Synchrotron

emission, SSC and Comptonization of the thermal photons with same order of magnitude component. Their most plausible source of energy is magnetic and so a Poynting flux dominated outflow. In [141] they suggest that the non thermal component is due to the Compton scattering (or *up scattering*) to the high-energy range by the electrons (and positrons) accelerated in the internal shocks, while the low energy excess can be explained using Synchrotron and SSC emission. In the same class of photospheric models [159] there is the possibility that the extracomponent is emitted through synchrotron emission in internal shock of Very High Lorentz Factor (VHLF,  $10^3 - 10^6$ ) jets of relativistic (not thermalized) baryons. Other models on the photosphere emission can be found in [95]. All these models suppose that the extended emission is due to the standard external shock model.

In [144] and also [97] they conclude that the signal above 100 MeV, the X-ray and optical photons were all produced by the same source, and they suggest that this source must be the external forward shock. Their relevant assumption on the synchrotron cooling frequency  $\nu_c$  (the synchrotron frequency corresponding to the electrons energy for which the radiative loss time-scale equals the dynamical time) is not in agreement with the multi-wavelengths analysis and observations of this burst done by [160] and [161]. In [134] they suggest that the high-energy emission has, similarly, an afterglow origin. They suggest that the time overlap of the high-energy emission with the prompt phase, observed by the GBM, can be explained by invoking a relatively large value of the bulk Lorentz factor, corresponding to relatively small deceleration radii and onset times largely contracted by the Doppler effect. Another afterglow model is in [162], where also the highest energy photon results compatible with synchrotron radiation; a complete evaluation of the needed magnetic fields and possible limits of this model are in [163]. The observed variability time scale ( $\approx 90$  ms) [214] in the LAT data argues against such afterglow models. Another problem with this kind of interpretation is that often the high energy component (see the second peak of GRB080916C and the sharp peak of GRB090926A) seems to follow well the GBM lightcurve, while this two component should be unrelated or at least delayed. Another interpretation in [164] is that the emission after  $\sim 50$  s detected by the LAT and low energy (radio, optical and X-

ray) are caused by a two-component forward-reverse external shock in a monotonic circumburst environment. The two-component jet model consists of a narrow and bright jet component in the core and a surrounding wider and less energetic jet component (this is a model suitable for the simulations with a more accurate model is probably a gaussian angular profile of the jet). The early-time high-energy emission detected by LAT before  $\sim 50$  s is likely due to internal origin as that of the sub-MeV emission. When observers view along the axis, one will see the afterglow emission produced by both the bright core and the broad wings surrounding the core. As the narrow component has a small opening angle, the jet break in the light curve can occur very early and the afterglow emission produced by the narrow component will have a fast decay after that time. This provides a potential mechanism to produce the early-time fast decaying optical emission of GRB 090902B, while the late radio, optical and X-ray afterglows that have normal light curves can arise from the wide component [164]. They attributed the extended high-energy emission detected by LAT to the afterglow emission (forward shock) of the narrow component before the jet break. The prompt emission could not be included even with a really high bulk lorentz factor ( $\Gamma = 3000$ ) but need an different component (a similar result was also obtained for GRB090510 [165] and [166]). A possible issue with this kind of model is the fact that the whole LAT detected emission has a similar spectral index from the beginning and the flux has a continuous decay, so the two mechanism internal and external should match.

The 33.4 GeV photon, the highest energy yet detected from a GRB, and the  $z = 1.822$  redshift of this burst have put some significant constraint on some models of Extragalactic Background Light (EBL) [214]. The highest energy photon would not be absorbed by the EBL in any models except for the *fast evolution* and the *baseline* models [167], which give optical depths of  $\tau_{\gamma\gamma} = 7.7$  and 5.8, respectively. Using Monte Carlo simulations this two models are disfavoured at a  $> 3\sigma$  level. Several other analysis on this topic have been done on each GRB and all together with also the AGN data [220] increasing the statistical relevance (above  $10\sigma$  post-trial).

### 3.2.4 Multi-wavelengths Observations

Several multi wavelength study have been performed and reported on this burst (for a full list and references see [83]) with different results. For [161] only the declining radio afterglow seems to require a jet break at  $t_j = 6.2_{-0.8}^{+2.4} \text{days}$ . Their multi wavelength analysis suggest an high kinetic energy released in the afterglow ( $E_{KE,iso} = 6.8_{-0.6}^{+1.4} \times 10^{53}$  erg, a factor of five less than the prompt gamma-ray energy release) and a really low circumburst density ( $n = 5.8_{-1.8}^{+1.2} \times 10^{-4} \text{cm}^{-3}$ ). Such a small density is similar to the one measured in the Interstellar medium or even Inter Galactic Medium. The opening angle they [161] evaluate is:  $\theta_j = (3.4_{-0.3}^{+0.4})^\circ$ , and so the collimated energy release is  $E_{\gamma, collimated} = (5.6 \pm 1.5) \times 10^{51}$  erg. A similar analysis [160] derived a limit on the opening angle of  $\theta_j > 6^\circ$  (based on a lower limit to the jet break time of  $t_j > 6$  days), where this opening angle is bigger than the previous estimate and so the total energy budget evaluated in  $E_\gamma > 2.2 \times 10^{52}$ . The difference between the two analysis is in the estimated value of the circumburst medium.

In both the analysis [161][160] a presence of the reverse shock is used to explain the early (up to 12.5 h after  $T_0$ ) optical and radio afterglow, then it becomes not relevant and the best fit is for a forward-shock afterglow models. In [83] they used a latter time for the jet break, they have an indication from optical observation for a break time of around 1.5 Ms post burst ( $\sim 17$  days) and the resulting half opening angle would be  $7.2^\circ$ , with a conservative lower limit of  $t_{break} \gtrsim 1.1$  Ms the resulting angle is  $\theta_{jet} \gtrsim 6.4^\circ$ . This implies a beaming corrected energy of  $E_\gamma \gtrsim 2.2 \times 10^{52} \text{erg}$ .

Even with different analysis and datasets this burst results in one of the most energetic events ever observed, with other LAT detected bursts as GRB080916C.

### 3.3 GRB091031A and GRB100325A

At 12:00:28.85 UT on 31 October 2009, the Fermi Gamma-Ray Burst Monitor triggered and located GRB 091031A [168]. The angle of the GBM best position (RA, Dec= 70.58, -59.08) with respect to the LAT boresight was  $\sim 22^\circ$  at trigger time, which is well inside the field of view, it remains

observable for more than 1 ks. The LAT [298] detected several events correlated in space and time with the GBM emission. In the time interval  $T_0 - T_0 + 100$ s using likelihood methods on photons above 100 MeV this burst has a significance of more than  $3\sigma$ ; using counting methods (e.g. Li and Ma [169]) the significance is well over 6 sigma in the full LAT energy band (20 MeV - 300 GeV). About 20 photons above 100 MeV were observed in the same time interval in an energy dependent ROI centered on the GBM position, the main part of the emission is at a lower energy where the reconstruction is not yet validated. The best LAT on-ground localization is found to be (RA, Dec = 71.7, -57.5) with a 90% containment radius of 0.3 deg (statistical; 68% containment radius: 0.2 deg, preliminary systematic error is less than 0.1 deg) which is consistent with the GBM localization. This localization could be affected from the small photons statistics. This burst was also detected by Konus-Wind and Konus RF [170] for  $\sim 40$ s. Their preliminary best fit is a power law with exponential cutoff and a fluence of  $(1.94 \pm 0.2) \times 10^{-5} \text{ erg/cm}^2$  (20 keV - 2 MeV). At 06:36:08.02 UT on 25 March 2010, the *Fermi* GMB triggered and located GRB 100325A [171]. The angle between the GRB and the LAT boresight was  $\sim 9.2^\circ$  at the time of the trigger, close to the center of the LAT field of view. The data from the LAT showed a weak increase in the event rate that is spatially and temporally correlated with the GBM emission [295]. It was a relatively weak detection ( $\sim 4\sigma$ ) with 4 photons above 100 MeV within 9 seconds after the GBM trigger (3 diffuse class and one transient class, see paragraph 2.8). The highest energy photon has an energy just above 800 MeV. The best LAT on-ground localization was preliminary found to be (RA, Dec = 330.24,-26.47) (J2000) with a 90% containment radius of  $0.9^\circ$  (statistical; 68% containment radius:  $0.6^\circ$ ) which is consistent with the GBM localization. The observed flux (100 MeV-300 GeV) from this location is  $(1.18 \pm 0.76) \text{ E-04 (ph/cm}^2\text{/s)}$ . Unluckily there were not other observation of this burst by other instruments.

### 3.4 GRB090510 and limits on the lorentz invariance violation

On the 10th of May 2009 at 00:22:59.97 UT the bright and intense GRB 090510 triggered autonomously both the instrument on board the *Fermi* satellite, LAT [172] and GBM [173]. The prompt part of this burst was observed also by AGILE [174] and Swift [218]. The spectral analysis of this burst is in [216] and also in [175].

The known distance of GRB090510 ( $z = 0.903 \pm 0.003$  [176]) and the detection of  $> 1$  GeV photons after less than a second from its onset allowed us to constrain the possible variation of the speed of light with photon energy, known as photon dispersion: one form of the Lorentz Invariance Violation (LIV). This analysis is extensively reported in [221] and in [300]. Some quantum-gravity theories [177] [178] [179] are consistent with the photon-propagation speed  $v_{ph}$  varying with photon energy  $E_{ph}$ , and become considerably different from the ordinary (or low-energy limit of) speed of light,  $c \equiv v_{ph}(E_{ph} \rightarrow 0)$ , near the Planck scale (when  $E_{ph}$  becomes comparable to  $E_{Planck} = M_{Planck}c^2$ ). For  $E_{ph} \gg E_{Planck}$ , the leading term in a Taylor series expansion of the classical dispersion relation is  $|v_{ph}/c - 1| < (E_{ph}/M_{QG,n}c^2)^n$ , where  $M_{QG,n}$  is the quantum gravity mass for order  $n$  and  $n = 1$  or  $2$  is usually assumed. The linear case ( $n = 1$ ) gives a difference  $\Delta t = \pm(\Delta E/M_{QG,1}c^2)D/c$  in the arrival time of photons emitted together at a distance  $D$  from us, and differing by  $\Delta E = E_{high} - E_{low}$ . At cosmological distances this simple expression is modified (see SM 4 of [221]).

When allowing for LIV-induced time-delays, the measured arrival time,  $t_h$ , of the high-energy photons might not directly reflect their emission time,  $t_{em}$  (which would have been their arrival time if  $v_{ph} = c$ ). Therefore, we make reasonable and conservative assumptions on  $t_{em}$ , constraining it using the observed lower-energy emission (for which LIV-induced time-delays are relatively negligible). The limits obtained on this analysis are shown in the Table 3.2; the most conservative are in bold and more information on this analysis can be found in SM 4 of [221].

It is important to notice that our most conservative limits (the first and the last in Tab. 3.2), rely on very different and largely independent

$t_{start}$ [ms]	limit on $ \Delta t $ [ms]	Reason for choice of $t_{start}$ or limit on $\Delta t$ or $ \Delta t/\Delta E $	$E_l^a$ [MeV]	Valid for $s_n^b$	Lower limit on $\frac{M_{QG,1}}{M_{Planck}}$	limit on $\frac{M_{QG,2}}{M_{Planck}}$ in $10^{10}$ $\text{GeV}/c^2$
-30	< 859	start of any observed emission	0.1	1	> <b>1.19</b>	> 2.99
530	< 299	start of main < 1 MeV emission	0.1	1	> 3.42	> 5.06
630	< 199	start of > 100 MeV emission	100	1	> 5.12	> 6.20
730	< 99	start of > 1 GeV emission	1000	1	> 10.0	> 8.79
-	< 10	association with < 1 MeV spike	0.1	$\pm 1$	> 102	> 27.7
-	< 19	if 0.75 GeV $\gamma$ is from 1 <sup>st</sup> spike	0.1	-1	> 1.33	> 0.54
-	$ \frac{\Delta t}{\Delta E}  < 30 \frac{ms}{GeV}$	lag analysis of all LAT events	-	$\pm 1$	> <b>1.22</b>	-

<sup>a</sup>The typical energy of the low-energy photons that were used for reference.

<sup>b</sup> $s_n = 1$  and  $-1$  stand for a positive ( $v_{ph} < c$ ) and negative ( $v_{ph} > c$ ) time delay, respectively.

**Table 3.2:** Limits on Lorents Invariance Violation (LIV). The two most conservative limits are in **bold**. The first four limits on the table are established using different  $t_{start}$  and always the 31 GeV photons. The different values of  $t_{start}$  are chosen because, in general, it is highly reasonable that an high energy photon is emitted in temporal coincidence with other  $\gamma$ -rays of lower energy that should suffer less the LIV induced delay. Higher is the  $E_l$  of the photons considered, closer is the  $t_{start}$  to the  $t_h$  of the 31 GeV photon and higher is the limits on the LIV (even if less conservative). The following 2 limits of either sign are based on the temporal association of the 31 GeV photon with the 7th GBM spike, and by associating the 0.75 GeV photon with the first GBM spike. The last limit is based on an upper limit of  $|\frac{\Delta t}{\Delta E}| < 30 \frac{ms}{GeV}$  on the spectral lag of the LAT photons (energetic interval: 35 MeV-31 GeV, time interval: 0.50-1.45 s) obtained with DisCan method [180] (see SM 3 of [221] and also [181]).

analysis, yet still give a very similar limit, of  $M_{QG,1}/M_{Planck} > 1.2$ . This gives considerable support to this result, and makes it more robust and secure than for each of the methods separately. This limit is much stronger than the previous best limit of this kind ( $M_{QG,1}/M_{Planck} > 0.1$  from GRB080916C [213]) and fundamentally more meaningful. Given that in most quantum gravity scenarios  $M_{QG,n} \leq M_{Planck}$ , even our most conservative limits greatly reduce the parameter space for  $n=1$  models as [182] and [183]. Our other limits, and especially our least conservative limit of  $M_{QG,1}/M_{Planck} > 102$ , make such theories highly implausible (models with  $n > 1$  are not significantly constrained by our results). Compatible limits are reported in [175], they associate the HE component ( $> 100$  MeV) to the afterglow not to the prompt part observed by the GBM. Therefore their limits are determined using only LAT photons. The detection of a possible earlier ( $T_0 - 13s$ ) precursor [184] in the Swift BAT data (probability of a chance fluctuation  $< 10^{-5}$ ) shows that emission started well before the GRB, implying a maximum delay of  $\sim 13.3$  s between the lowest and highest energy photons. The corresponding upper limit on the quantum gravity mass is therefore significantly reduced to  $M_{QG} > 0.09M_{Pl}$ . However, it is not easy to explain which mechanism can accelerate the highest energy photon in coincidence of low energies precursors (both the one observed by the GBM and the one by Swift) in absence of a significant contemporaneous emission in the LAT.

The constraint on the quantum gravity mass scale from GRB 080916C, with the photon of  $E_h = 13.22^{+0.70}_{-1.54}$  GeV, which arrived 16.54 s after the GRB trigger is  $M_{QG,1} > 0.1M_{Planck}$  (making the conservative assumption that the high energy photon is not emitted before the trigger). The limits obtained with GRB090902B are similar and weaker than the one illustrated fro GRB090510C.

## Chapter 4

# GRB091003

### 4.1 Detections and Light Curves

The 2009-10-03 at 04:35:45.58 (Mission Elapsed Time 276237347.58) the GBM triggered on a long burst [185]. The first on ground LAT localization was: (Right Ascension, Declination)=(251.39, 36.58) ( with a 90% statistical containment radius of 0.21 deg and a preliminary systematic error is estimated less than 0.1 deg). This localization was reported in [186] and is consistent with the GBM one. The spectral characteristics of this burst satisfied the condition of an ARR. The satellite started to move only 21-22 seconds after the trigger time (the 1 second interval is due to the ft2 file 1s binning, see section 2.11); the maneuver ended 198 seconds later while the satellite remained in pointing mode for 5 hours, then it returned to the normal operation mode 18ks after. During all this time interval the SAA zone was not encountered so the data taking was continuous.

Several other detectors on satellites observed this GRB as INTEGRAL SPI-ACS, Konus-Wind [187] and Suzaku-WAM [188], Swift XRT and UVOT [189] detected the GRBs afterglow from 15.5 hours after the trigger. Swift XRT localized this burst in (R.A., Dec.)=(251.51980, 36.62470) with an uncertainty of 1.7 arcsec (radius, 90% confidence) [190], this was compatible with the UVOT localization. This location was used in the following analysis, the localization reported in the final report [189] is slightly different but is compatible within the errors. The optical afterglow was also observed with ground-based instruments [191] [192] and a possible host galaxy was observed and an emission-line redshift of  $z = 0.8969$  was determined for

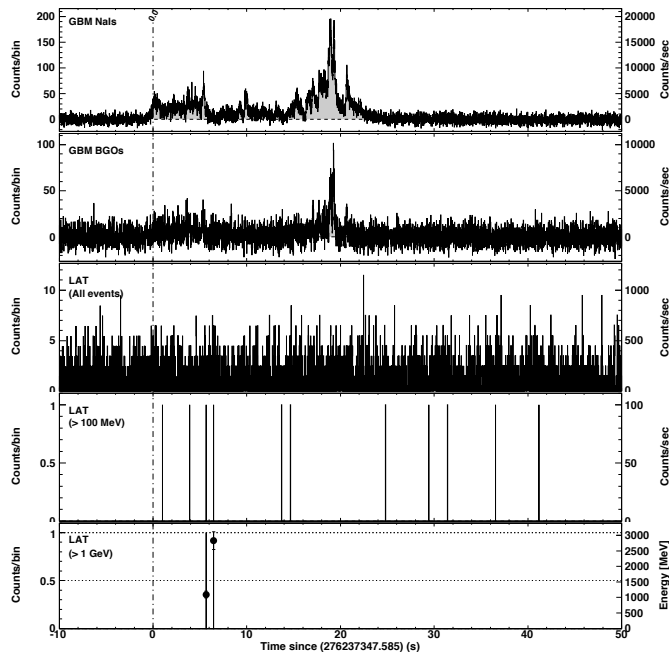


**Figure 4.1:** Light curve of the GRB 091003. From the upper panel, the NaIs data and then the BGOs and all the LAT data that are reconstructed on the ground. In the two panels at the bottom the transient class events are shown, respectively above 100 MeV and 1 GeV. GBM and LAT "all events" data are background subtracted with the background evaluated by fitting the interval before the burst.

it [193]. The composed light curve of all the *Fermi* detector used in the analysis of the burst is shown in Fig. 4.1 and the LAT photons are plotted also in Fig. 4.2.

The analysis in this chapter should be considered *preliminary*, since a full validation and verification through the *Fermi* LAT working group is on going.

## 4.2 Prompt emission spectral analysis

For a complete spectral analysis of this burst the LAT data were divided in time bins equal to the one of the CSPEC data files of the GBM ( $\sim 1$  s) and in 10 bins in energy between 80 MeV and 100 GeV logarithmically spaced. There were no transient photons between 80 and 100 MeV, a lower limit was chosen for increase the statistics using looser selections, not reported extensively here. The photons used in the analysis are in an energy dependent Region Of Interest based on the 95% containment radius

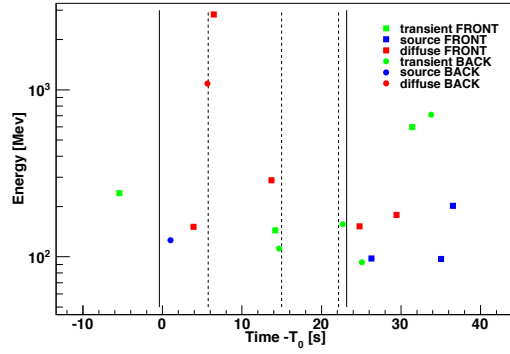


**Figure 4.2:** LAT light curve of the GRB 091003. This are all the photons in an energy dependent Region Of Interest (ROI) around the Swift enhanced localization. This are the same photons used for the spectral analysis. The different time intervals are shown with the vertical lines. Photons of different event class, see paragraph 2.8 are depicted with different color.

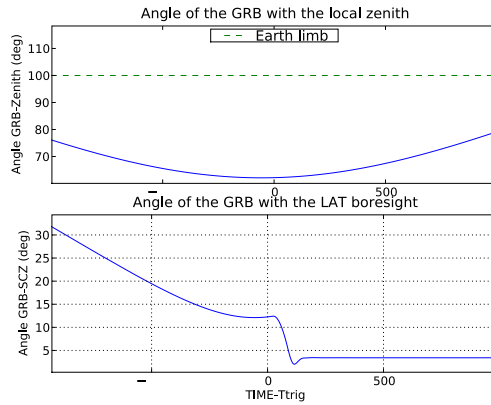


**Figure 4.3:** Fermi orbital informations obtained by the ft2 files (see section 2.11). In the upper panel the angular distance of the GRB from the local zenith is depicted. In the lower panel there is the angular distance between the GRB and the Fermi boresight. Around 20 second after the trigger the slew started and the ARR has kept the GRB close to the center of the field of view.

( $PSF_{95}$ ) and the Swift error localization (LocErr):

$$ROI(E) = \sqrt{PSF_{95}(E)^2 + LocErr^2}. \quad (4.2.1)$$

similarly to other LAT bursts, see also [217]. The background for the LAT was estimated using the data in various orbit in a similar attitude and localization. The fit were performed using RMFIT (v3.3pr7<sup>1</sup>) and it were minimized using the Cash statistics [129], that gives less biased results when used in low count regime as in this case. The implementation of the Cash in RMFIT is also known as Castor statistic since it tends to  $\chi^2$  for large counts.

The background of the GBM data was estimated using the pre and post data of each detector fitted with a polynomial function, to account for the background change. This standard procedure was particularly important since the ARR changed the pointing direction of the spacecraft, and this affected the background, even if the ARR started after 22 s the trigger time when the prompt part of the burst was almost over.

The best fit of the time integrated spectra is a single Band function, even if the low energy part observed by the GBM only can be described by an harder but more complex spectra as a Power Law with two spectral break ( $\Delta Cstat \sim 20$ ). The improvement is not statistically significant and also the high energy part of the spectra goes even further from the LAT part. The fit results of the whole interval are reported in the table 4.1. Given the presence of two distinct spikes in the NaIs and BGOs lightcurve, Fig. 4.1, a time resolved analysis was done, whose results are in the tables 4.2, 4.3 and 4.5 respectively for the first peak, the plateau and the second peak. Photons above 100 MeV were detected by the LAT only in the first two intervals, see Fig. 4.2, since in each of them an additive component (modeled as a PL with Pivot energy at 100 MeV) is not statistically significance, they were analyzed together and the results are reported in the table 4.4. Even if the fit is far from some of the high energy bins (but each of them contains only 1 photon) an additive component is not significant and the best fit remains a Band function. The Pivot energy of the additive Power Law used in the analysis shown here is 100 MeV, different values were tried from 100 keV to

<sup>1</sup><http://fermi.gsfc.nasa.gov/ssc/data/analysis/user/>

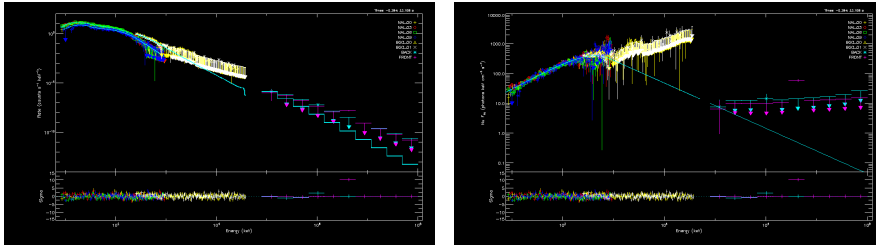


**Figure 4.4:** Band fit of the full interval

1 GeV, the results were similar but using 100 MeV the profile likelihood of the spectral index is more symmetric than in the other cases.

During the second peak photons above 100 MeV were not observed and the spectrum seems to become steeper also in the BGO energy range. In table 4.5 different spectral fits are reported. The presence of an high energy cut-off modeled as  $exp(E/E_{fold})$  gives rise to a variation of the Cash statistics of 38 without the effective area correction and 41 using it, with respect to the Band only fit. Comptonized spectra (obtainable from a Band function with  $\beta \rightarrow -\infty$ ) give rise to a similar fit to the Band function and the improvement with Band+HC is similar.

The high energy cut described in the table can be obtained with a particular choice of the starting parameters, basically a not too steep  $\beta \sim -2$  and a low  $E_{fold} \sim 100keV - 1MeV$ . Without this choice the fitting algorithm misses the minimum, as shown in Fig. 4.5, the statistical improvement is less relevant, as shown in the last row in table 4.5, and the fit basically becomes equal to the Band fit only. This does not happen when using the effective area correction for the two BGOs, where for a large set of starting point a similar minimum is reached (even if sometimes the minimization algorithm needs to run twice). The profile likelihood is broader but has several less local minimum.

### 4.3 Highest energy photon

The highest energy photon of this burst has an energy of 2828.478 MeV the energy resolutions is around 10%, it falls in the 6th energy bin of the previous binned spectral analysis (EVENT\_ID = 10303815). Since the distance of this bin from the fitted Band function is around  $10\sigma$  in the residual space (in the

Model	Amplitude	$E_{peak}$	$\alpha$ or Compt. Index	$\beta$	PL Index	C-Stat/DOF	Ph. Flux [ $phs^{-1}cm^{-2}$ ] ( $10 \div 10^7 keV$ )	En. Flux [ $ergs^{-1}cm^{-2}$ ] ( $10 \div 10^7 keV$ )
Band	$0.03 \pm 0.00$	$447.30 \pm 11.60$	$-1.09 \pm 0.01$	$-2.76 \pm 0.05$	-	925.17/743	$8.60 \pm 0.04$	$(1.537 \pm 0.011)E-06$
PL w/ Band	$5.21E-11 \pm 1.96E-10$ $0.03 \pm 0.00$	$451.00 \pm 12.00$	$-1.09 \pm 0.01$	$-2.85 \pm 0.12$	$-1.35 \pm 1.09$	921.67/741	$8.80 \pm 0.04$	$(2.119 \pm 0.067)E-06$
PL w/ Comp	$3.25E-10 \pm 1.35E-08$ $0.02 \pm 0.00$	$464.90 \pm 11.20$	$-1.09 \pm 0.01$	-	$-1.75 \pm 0.22$	928.94/742	$8.78 \pm 0.04$	$(1.872 \pm 0.031)E-06$
Band w/ Eff. Area	$0.03 \pm 0.00$	$377.30 \pm 11.20$	$-1.05 \pm 0.01$	$-2.72 \pm 0.05$	-	883.87/741	$8.67 \pm 0.04$	$(1.981 \pm 0.043)E-06$
PL w/ Band w/ Eff. Area	$4.445E-11 \pm 1.81E-10$ $0.03 \pm 0.00$	$381.00 \pm 11.60$	$-1.05 \pm 0.01$	$-2.78 \pm 0.10$	$-1.32 \pm 1.17$	880.80/739	$8.68 \pm 0.04$	$(1.959 \pm 0.061)E-06$

**Table 4.1:** Full interval fit, from  $T_0 - 0.384$  s to  $T_0 + 23.168$  s of the GBM data (NaI0-3-6-9, BGO 0-1) and FRONT and BACK LAT data. Compatible results were obtained using GBM data only and looser cuts, this is not unexpected given the small number of LAT photons. The Effective Area correction, listed here and in the other section is intended for correct some observational issues and it is a flat correction of the response function, during this analysis it was used only on the BGOs and the relative correction to NaI0 is  $0.80 \pm 0.02$  and  $0.84 \pm 0.02$  for the Band fit and it's compatible for the other cases (fit leaving the other GBM detectors effective area normalization free to vary have lead to really similar fit and the correction values are compatible with 1). The Pivot Energy of the additive Power Law used in this analysis is 100 MeV, this was chosen since it gives the more symmetric curve of the PL index, changing this value from 100 keV to 10 GeV did not change in a significant way the results.

Model	Amplitude	$E_{peak}$	$\alpha$ or Compt. Index	$\beta$	PL Index	C-Stat/DOF	Ph. Flux [ $phs^{-1}cm^{-2}$ ] ( $10 \div 10^7 keV$ )	En. Flux [ $ergs^{-1}cm^{-2}$ ] ( $10 \div 10^7 keV$ )
Band	$0.03 \pm 0.00$	$575.30 \pm 25.70$	$-0.94 \pm 0.02$	$-2.82 \pm 0.10$	-	728.70/743	$8.65 \pm 0.08$	$(2.665 \pm 0.094)E-06$
PL w/ Band	$4.04E-10 \pm 3.66E-10$ $0.02 \pm 0.00$	$565.10 \pm 30.20$	$-0.90 \pm 0.05$	$-2.98 \pm 0.26$	$-1.97 \pm 0.14$	727.82/741	$8.67 \pm 0.09$	$(2.593 \pm 0.120)E-06$
PL w/ Comp	$6.55E-10 \pm 2.98E-10$ $0.02 \pm 0.00$	$573.10 \pm 27.20$	$-0.90 \pm 0.05$	-	$-1.94 \pm 0.10$	729.48/742	$8.65 \pm 0.09$	$(2.356 \pm 0.069)E-06$
Band w/ Eff. Area	$0.03 \pm 0.00$	$532.50 \pm 28.00$	$-0.93 \pm 0.02$	$-2.81 \pm 0.10$	-	724.78/741	$8.42 \pm 0.08$	$(2.643 \pm 0.100)E-06$

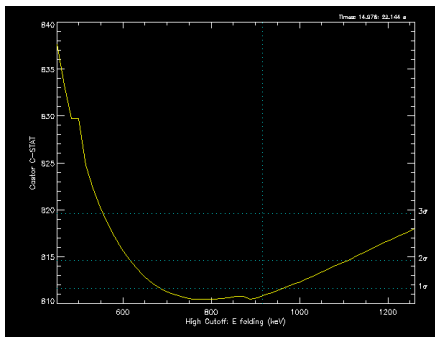
**Table 4.2:** First Peak, from  $T_0 - 0.384$  s to  $T_0 + 5.760$  s, of the GBM data (NaI0-3-6-9, BGO 0-1) and FRONT and BACK LAT data. Compatible results were obtained using GBM data only and looser cuts. The effective area correction for the two BGOs are respectively  $0.90 \pm 0.03$  and  $0.92 \pm 0.03$ . Similar results are obtained with looser cuts and with the GBM only data.

Model	Amplitude	$E_{peak}$	$\alpha$ or Compt. Index	$\beta$	PL Index	C-Stat/DOF	Ph. Flux [ $phs^{-1}cm^{-2}$ ] ( $10 \div 10^7 keV$ )	En. Flux [ $ergs^{-1}cm^{-2}$ ] ( $10 \div 10^7 keV$ )
Band	$0.01 \pm 0.00$	$198.30 \pm 21.80$	$-1.34 \pm 0.04$	$-2.41 \pm 0.06$	-	778.86/743	$4.14 \pm 0.06$	$(6.294 \pm 0.380)E-07$
PL Band w/	$5.75E-10 \pm 2.90E-10$ $0.01 \pm 0.00$	$205.70 \pm 19.50$	$-1.31 \pm 0.09$	$-6.29 \pm 237.00$	$-1.88 \pm 0.23$	773.99/741	$4.12 \pm 0.07$	$(5.288 \pm 0.900)E-07$
PL Comp w/	$5.37E-10 \pm 2.82E-10$ $0.01 \pm 0.00$	$204.20 \pm 17.70$	$-1.32 \pm 0.06$	-	$-1.84 \pm 0.25$	773.97/742	$4.11 \pm 0.06$	$(5.258 \pm 0.370)E-07$
Band w/ Eff. Area	$0.01 \pm 0.00$	$185.80 \pm 21.90$	$-1.33 \pm 0.05$	$-2.42 \pm 0.06$	-	777.18/t41	$4.13 \pm 0.06$	$(6.233 \pm 0.380)E-07$

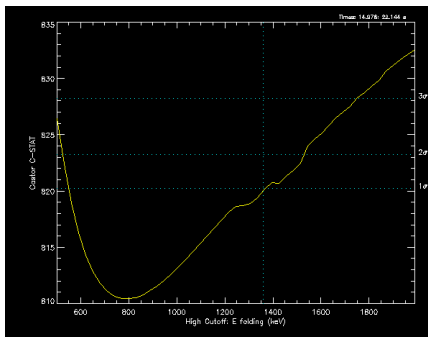
**Table 4.3:** Plateau, from  $T_0+5.760$  s to  $T_0+14.976$  s, of the GBM data (NaI0-3-6-9, BGO 0-1) and FRONT and BACK LAT data. Compatible results were obtained using GBM data only and looser cuts. Similar results are obtained with looser cuts and with the GBM only data. The effective area parameters for the two BGOs in this time intervals are badly constrained, they result  $0.74 \pm 0.11$  and  $0.95 \pm 0.17$ .

Model	Amplitude	$E_{peak}$	$\alpha$ or Compt. Index	$\beta$	PL Index	C-Stat/DOF	Ph. Flux [ $phs^{-1}cm^{-2}$ ] ( $10 \div 10^7 keV$ )	En. Flux [ $ergs^{-1}cm^{-2}$ ] ( $10 \div 10^7 keV$ )
Band	$0.02 \pm 0.00$	$469.90 \pm 24.50$	$-1.14 \pm 0.02$	$-2.62 \pm 0.05$	-	811.21/743	$5.78 \pm 0.05$	$(1.411 \pm 0.045)E-06$
PL Band w/	$9.10E-11 \pm 3.30E-10$ $0.02 \pm 0.00$	$474.30 \pm 25.00$	$-1.14 \pm 0.02$	$-2.72 \pm 0.16$	$-1.37 \pm 1.06$	808.05/741	$5.77 \pm 0.05$	$(1.391 \pm 0.069)E-06$
PL Comp w/	$6.33E-10 \pm 1.89E-10$ $0.02 \pm 0.00$	$471.70 \pm 25.40$	$-1.09 \pm 0.05$	-	$-1.93 \pm 0.09$	811.36/742	$5.77 \pm 0.05$	$(1.216 \pm 0.037)E-06$
Band w/ Eff. Area	$0.02 \pm 0.00$	$410.10 \pm 24.70$	$-1.12 \pm 0.02$	$-2.60 \pm 0.05$	-	802.02/741	$5.75 \pm 0.05$	$(1.400 \pm 0.046)E-06$

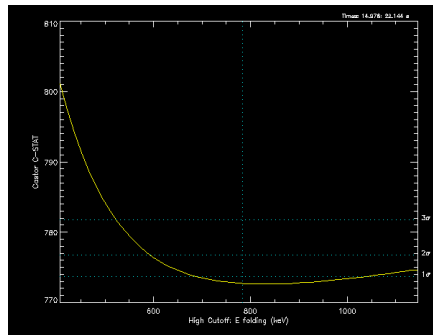
**Table 4.4:** First part (First peak + Plateau), from  $T_0 - 0.384$  s to  $T_0 + 14.976$  s, of the GBM data (NaI0-3-6-9, BGO 0-1) and FRONT and BACK LAT data. Compatible results were obtained using GBM data only and looser cuts. The effective area correction for the two BGOs are respectively  $0.82 \pm 0.04$  and  $0.89 \pm 0.04$ . Similar results are obtained with looser cuts and with the GBM only data.



(a) Best fit



(b) Fit with steeper  $\beta$



(c) Best Fit with Eff. Area.

**Figure 4.5:** Profile probability for the  $E_{fold}$  for the fit in the second peak

Model	Amplitude	$E_{peak}$	$\alpha$ or Compt. Index	$\beta$	$E_{fold}$	C-Stat/DOF	Ph. Flux [ $phs^{-1}cm^{-2}$ ] ( $10 \div 10^7$ keV)	En. Flux [ $ergs^{-1}cm^{-2}$ ] ( $10 \div 10^7$ keV)
Band	$0.05 \pm 0.00$	$451.80 \pm 12.00$	$-1.02 \pm 0.01$	$-3.47 \pm 0.60$	-	848.69/743	$15.85 \pm 0.09$	$(3.580 \pm 0.170)E-06$
Comp	$0.05 \pm 0.00$	$458.10 \pm 10.60$	$-1.03 \pm 0.01$	-	-	849.19/744	$15.84 \pm 0.09$	$(3.415 \pm 0.045)E-06$
Band w/ Hi Cut	$0.07 \pm 0.00$	$295.00 \pm 36.70$	$-0.83 \pm 0.02$	$-1.34 \pm 0.01$	$915.80 \pm 90.20$	810.60/742	$15.71 \pm 0.23$	$(3.840 \pm 0.190)E-06$
Band w/ Eff. Area	$0.05 \pm 0.00$	$372.50 \pm 11.70$	$-0.98 \pm 0.01$	$-2.94 \pm 0.19$	-	813.76/741	$15.61 \pm 0.09$	$(3.456 \pm 0.160)E-06$
Comp w/ Eff. Area	$0.05 \pm 0.00$	$401.50 \pm 10.40$	$-1.00 \pm 0.01$	-	-	818.90/742	$15.63 \pm 0.09$	$(3.122 \pm 0.042)E-06$
Band w/ Hi Cut w/ Eff. Area	$0.06 \pm 0.00$	$343.00 \pm 34.1$	$-0.84 \pm 0.01$	$-1.41 \pm 0.02$	$786.1 \pm 95.4$	772.70/740	$15.46 \pm 0.17$	$(3.367 \pm 0.170)E-06$
Band w/ Hi Cut	$0.06 \pm 0.00$	$308.30 \pm 26.50$	$-0.86 \pm 0.01$	$-1.50 \pm 0.01$	$1378.00 \pm 168.00$	819.55/742	$15.78 \pm 0.17$	$(4.073 \pm 0.210)E-06$

**Table 4.5:** *Second Peak, from  $T_0 + 14.976s$  to  $T_0 - 0.384 s$  to, of the GBM data (NaI0-3-6-9, BGO 0-1) and FRONT and BACK LAT data. Compatible results were obtained using GBM data only and looser cuts. The effective area correction for the two BGOs are respectively (for band and band cut cut)  $0.80 \pm 0.02$  and  $0.82 \pm 0.02$  while for the Compton fit is  $0.82 \pm 0.02$  and  $0.85 \pm 0.02$ . Similar results are obtained with looser cuts and with the GBM only data.*

count space the distance is zero, since in the bin 6 there is just on photon and the associated Poisson error is exactly a unity) a further investigation was needed. Ten thousands simulation of the LAT FRONT spectrum were generated with RMFIT using both the full first part of the GRB and only the plateau, with respectively an exposure of 13.52 s and 8.1 s obtained summing the exposure in the interval in each bin of the PHA2 file. The simulations were all summed together and divided by their total number, the results are shown in Fig. 4.6. The plots are not normalized in total counts since each simulation can have none or more than only one photons in the same bin or in an higher one. The number of photons divided by the number of simulations in the 6th bin or above it are respectively  $13.9 \times 10^{-3}$  and  $21.8 \times 10^{-3}$  for the plateau, whereas if we consider the full first part of the emission they become  $12.0 \times 10^{-3}$  and  $18.3 \times 10^{-3}$ . Since all these photons are independent events the uncertainties on this numbers are poissonian. This numbers are shown also in Fig.4.6.

The fraction of each of the simulated dataset with at least one photon

in the 6th (in this case it is normalized on the number of the dataset simulated) for the plateau part of the emission is 1.37% while the fraction of the dataset that has any of the bins between 6 and 10 not empty is 2.16%. This probability for the full first part are respectively 1.20% and 1.81%. These results allow us to say that we cannot reject the hypothesis at 99.9% confidence level for the 2.8 GeV photons to belong to the same spectral function that well describes the rest of the low energy emission. The probability of the full first part is smaller than the one related just to the plateau since the  $\beta$  value of the Band function in the plateau part is harder than that in the whole first part. But because of the possible fluctuation on the observed values they seem compatible.

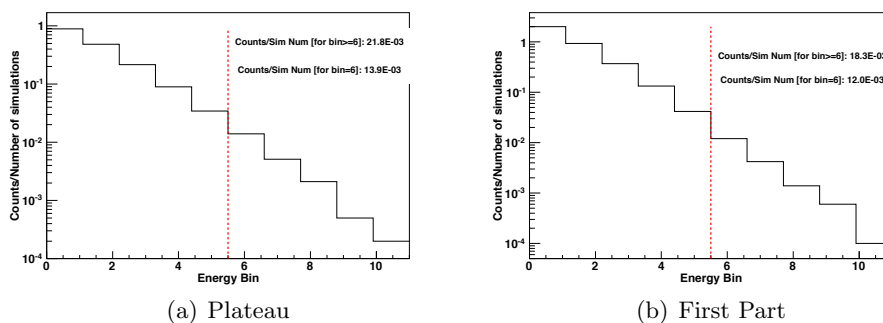


**Figure 4.6:** Counts divided by the number of the simulations (10k in this case)

#### 4.4 Simulation study of the High Energy cutoff

The variation of the Cash statistics between the Band fit and Band with an exponential high energy cut off in the latest interval fit is 38 (without effective area correction) and 41 (with effective area correction). If the Wilks theorem [194] holds, and so the  $\Delta$  Cstat is distributed as  $\chi^2(n$  degrees of freedom) and the statistical significance is respectively  $6.1 \sigma$  and  $6.4 \sigma$  with 1 degrees of freedom (d.o.f.). The d.o.f. is only one since the Band function with high energy cutoff has only one parameter fitted more than the simple Band function. The Wilks theorem can be applied since the two models are nested. A similar variation of Cstat is observed using the GBM only data (while excluding the NaI9 data, that is the most noisy one,

the  $\Delta C_{\text{stat}}$  decrease and becomes  $\sim 27$ ).

To evaluate if the  $\Delta C_{\text{stat}}$  have the expected distribution  $\chi^2$  just for the statistical fluctuation, one thousand simulations were generated with RMFIT for the Band function fit and they were refitted with the band function with and without the cutoff (this analysis was done twice with and without the effective area correction). The distribution seems far from the theoretical curve of a  $\chi^2$  function with both 1 or 2 d.o.f. The tails are higher and the distribution seems to follow more likely an exponential decay. This is still an open issue and it was already observed in previous version of the analysis software. A possible source of this problem is the starting value of the parameters that is forced to be too high and could not reach an optimal value for each dataset. Even in this conservative hypothesis none of the simulated dataset has shown an improvement above or equal the observed ones.

To study in greater details the presence of this Cutoff, twenty thousands simulations of the dataset (GBM + LAT) were generated and analyzed using XSPEC<sup>2</sup> (version 12.6.0q). The dataset used in the Xspec analysis is the same that is used for RMFIT and the background used for each GBM detector is obtained from the temporal fit used in RMFIT. The LAT background is estimated in a similar way as for RMFIT from the spacial attitude of the spacecraft. Xspec uses a slightly different implementation of the C-statistics, also known as W-statistics [195] that consider also poissonian fluctuation of the background (while RMFIT consider it fixed). Given this difference one or two channels on the low edge of the GBM datasets were excluded in the Xspec analysis. In the table 4.6 the comparison between the results obtained between Xspec and RMFIT are reported. In this analysis the Band function is parametrized differently, it is minimized on  $E_0 = E_{\text{peak}}(2 + \alpha)$  instead of  $E_{\text{peak}}$  as the definition 1.3.2. The  $\Delta C_{\text{stat}}$  obtained using Xspec is smaller (26.91,  $5.2\sigma$ ) than the one obtained, with RMFIT (45.48,  $6.7\sigma$ ) due probably to the added poissonian uncertainties of the background. Given the simulation study summarized in Fig.4.7, in both cases if the Wilks theorem holds, as it seems from the simulations, the significance of the cutoff with this selection seems above  $5\sigma$ .

---

<sup>2</sup><http://heasarc.gsfc.nasa.gov/docs/xanadu/xspec/>

Model	Amplitude	$E_0$ or tem	$\alpha$	$\beta$	$E_{fold}$	C-Stat /DOF
Band Old	$0.05 \pm 0.00$	$452.40 \pm 16.80$	$-1.02 \pm 0.01$	$-3.30 \pm 0.45$	-	839.37/735
Band Old w/ Hi Cut	$0.07 \pm 0.00$	$219.20 \pm 27.40$	$-0.80 \pm 0.02$	$-1.41 \pm 0.01$	$1074.00 \pm 117.00$	793.89/734
grbm	$0.05 \pm 0.00$	$433.62 \pm 24.63$	$-1.01 \pm 0.02$	$-3.82 \pm 2.02$	-	535.96/735
grbm*highcut	$0.06 \pm 0.00$	$271.38 \pm 59.71$	$-0.84 \pm 0.05$	$-1.33 \pm 0.10$	$828.96 \pm 200.40$	509.05/734

**Table 4.6:** *Second Peak analysis with RMFIT (the upper two row) and XSPEC (the lower two row) the function used in the two analysis is the same and differs from the usual definition since it use  $E_0 = E_{peak}/(2 + \alpha)$ . The Xspec fit with Band function has a worse constrained  $\beta$  than the RMFIT. The  $\Delta Cstat$  for RMFIT with this selection is 45.48 while for Xspec is smaller and is 26.91.*

Similar results are obtained by minimizing with Xspec using the  $\chi^2$  statistics (the error on  $\beta$  is smaller) with the errors on counts estimated using the Gehrels weighting [196] (for N counts the error is equal to  $1 + \sqrt{N + 0.75}$ , a better approximation when N is small). The Ftest performed on the variation of  $\chi^2$  between the Band fit and the Band with high energy cut-off has a value of 42.195 and probability of  $1.52312e-10$  ( $6.4 \sigma$ ).

## 4.5 Extended emission spectral analysis

A common characteristics of LAT burst detected up to now is that the high energy emission last more than the low energy ones. For this burst the GBM  $T_{90}$  is  $21.1 \pm 0.5s$  [185], the analysis of the LAT photons of the diffuse class shows that the high energy emission is still significant as long as 300 s after the trigger time. The events used in this analysis are in 15 degrees around the Swift localizations and are shown in the count plots in figure 4.8. The background used in this analysis is the standard one of galactic and extragalactic origin with normalization let free to vary, their variation in time can be explained also with the change of the satellite angle with the earth zenith due to the ARR that followed the trigger (see Fig. 4.3). The GRB in this analysis is modeled as a Power Law with integrated flux (between 100 MeV and 300 GeV) and the photon index as free parameters (*PowerLaw2*<sup>3</sup>). This allows a direct estimate of the error by

<sup>3</sup>[https://glast-ground.slac.stanford.edu/workbook/scienceAnalysis\\_Home.htm](https://glast-ground.slac.stanford.edu/workbook/scienceAnalysis_Home.htm)

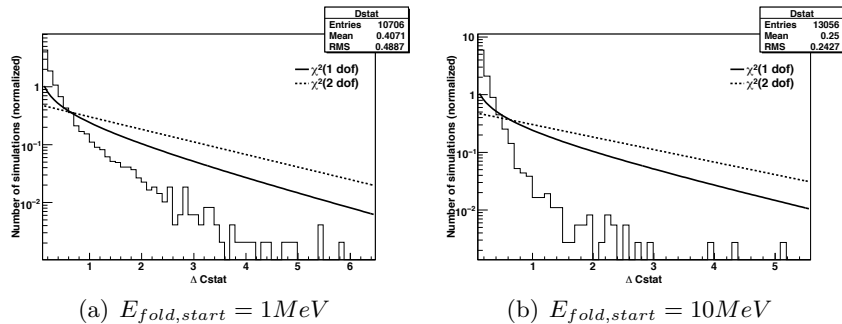


**Figure 4.7:** Distribution of the variation of the Cstat with the *xspec* simulation. Twenty thousands simulations were generated accordingly to the fit with the Band only fit described in table 4.6. The  $E_{fold}$  value in the two dataset is of 1 Mev and 10 MeV (since the runs were contemporaneous the seed of the two simulations can be the same and so they are not independent). In the plots are reported only the fits that improve the results of the fit ( $\Delta Cstat > 0$ ) and where  $\beta$  is not close to the edge of the allowed interval (-1, -5). The variation of Cstat between the Band fit alone and the Band fit with high energy cutoff seems to be below the theoretical curve of  $\chi^2(1d.o.f.)$  so the assumption of that curve for extrapolate the probability of the cutoff seems quite conservative. The theoretical curve and the histogram are normalized to unity. Different starting point of the parameters of the fit where tried but the results are similar. The difference between the observed distribution and the  $\chi^2(1d.o.f.)$  distribution could be due to the high error on beta and the overestimation of the errors on the data points.

the likelihood and also an estimate of their value if they are asymmetrical (e.g. the parabolic approximation is not completely true) without the errors propagations.

The resulting Test Statistics [197] ( $TS = -2\ln(L_{max,0}/L_{max,1})$  where  $L_{max,0}$  is the maximum likelihood for the model without the source while the  $L_{max,1}$  is the maximum likelihood with the source in the specified location) obtained by the likelihood in the different time interval is shown in Fig. 4.9. The TS remains above 30 for the first 3 bins that cover the interval from  $T_0$  to 300s while the low energy part of the spectra detected by the GBM is already well below the background, as shown in the lightcurve in Fig 4.1. The Wilks theorem [194] states that the TS for the null hypothesis is asymptotically distributed as  $\chi^2$  with number of degrees of freedom equal to the number of parameters characterizing the additional source, two in this case, the normalization and index of the power-law. It should be noticed that as shown in Fig. 4.10 the number of observed photons is small and so there could be deviations from the theoretical curve. A TS of 30 with two degrees of freedom correspond to  $5.1\sigma$ , usually [222] a TS of 25 ( $4.6\sigma$ ) is

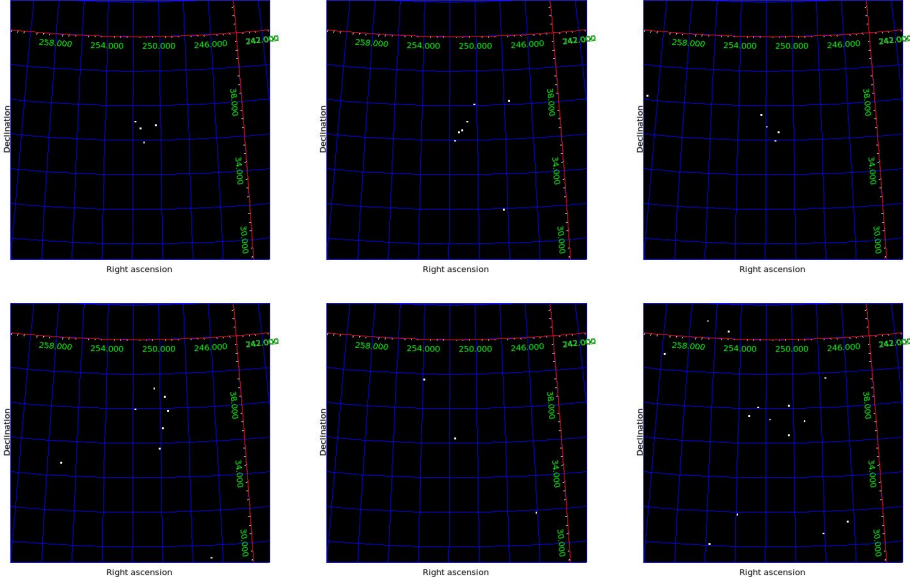


*Figure 4.8: Counts plots of photons used in the extended emission analysis in time bins  $T_0 - 0.384000003338$  s,  $+23.1679999828$  s,  $+100$ s,  $+300$ s,  $+700$ s,  $+1000$ s,  $+2000$ s*

considered as a threshold for a detection. The same analysis was done using also the transient class instead of the diffuse one, see par. 2.8. In this case the diffuse background was modeled with a Power Law with both normalization and index left free (a test with fixed index at -2.2 was performed also). Compatible results were found, except that the significance of the signal in the third bin is about 20 (instead than above 30) namely less than 5 sigma above the background. This difference could be explained with the increase of the Signal/Noise ration in the latter case; 4 diffuse class events in total 6 where associated with the GRB, while on 47 transient class events only 7 where associated with the GRB (see Fig. 4.10). The observed flux is shown in Fig. 4.11 with asymmetric errors and Upper limits at 95% confidence level when the TS is below 10 (so the signal is well compatible with the background). Two different upper limits are used, one based on the Helene technique and the other on the profile likelihood (**reference missing**), that gives similar results. Usually the decrease of the flux of GRBs detected by the LAT is of the type  $t^{-\alpha}$ , for this burst since only 3 points are available and each has a large error a good fit is impossible, but the decay seems steeper than other already observed. Indeed the signal above 100 MeV is

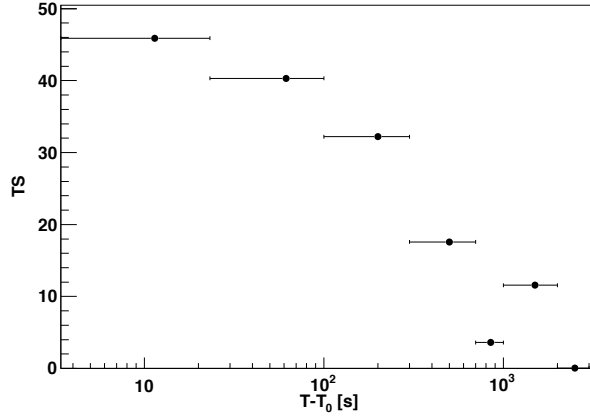


**Figure 4.9:** Test Statistics of GRB091003 in different time bin. In the first 3 bins it is above 30 and the signal is significantly ( $> 5\sigma$ ) above the background.

detectable for only few hundreds of seconds while is observable for several kseconds in other burst.

## 4.6 Discussion

This burst has shown in this preliminary analysis some interesting spectral features, future analysis will be able to put more light on them. The extended emission common to several LAT burst, except for the *featureless* GRB 090217 [219] is present even if the high energy tail is short compared to the other burst observed up to several ks after the trigger time. The possible cut-off during the second peak is interesting and unexpected as reported for the case GRB080825C [217] since it should not be due to the opacity but it could be due to a particular energy spectrum of the accelerated electrons, but it is not clear why a power-law would extend over a very narrow range in this case and a much larger dynamical range in most other cases.

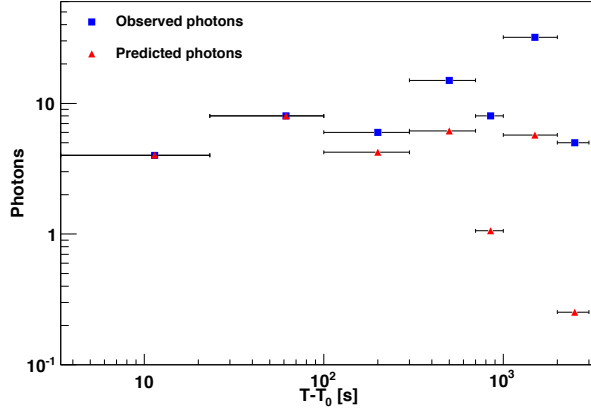


**Figure 4.10:** Observed number of photons in the ROI =  $15^\circ$  and number of photons associated to the GRB by the likelihood.

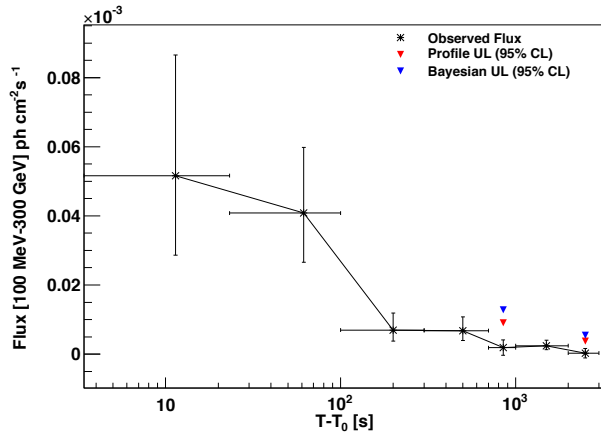


**Figure 4.11:** Observed flux of GRB091003 in different time bin. Each of the values shown has asymmetric errors at  $1\sigma$  level (obtained with MINOS). Two different Upper Limits (UL) at 95% Confidence Level (CL) are shown in the same plot for the intervals where the TS is below 10. The values obtained using the transient class where higher, so they could be considered conservative.

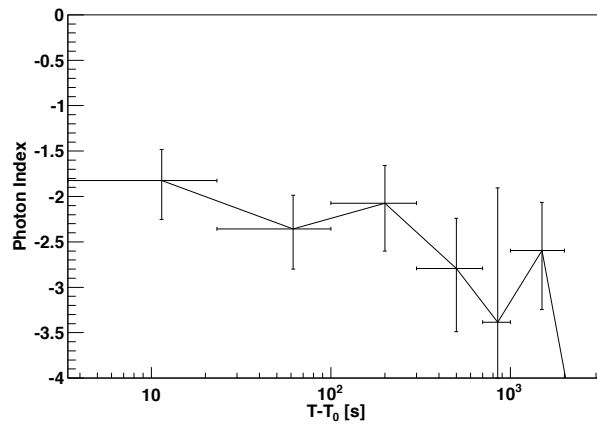


**Figure 4.12:** Plot of the photon indexes of the Power Law used for model the high energy part of the spectrum.



# Conclusions

The main topic of my thesis work is the analysis of the GRB observed by *Fermi*. As described in this thesis, they were discovered by chance in the sixties and they are still some of the most interesting and less understood object in the universe. *Fermi* LAT has all the characteristics needed for make unprecedented discoveries in this field for its large effective area, precise time resolution, small dead time and an extended energy range covered (from 100 MeV to 300 GeV, the lower bound is going to decrease down to  $\sim 20$  MeV in the near future with large statistical improvement of several analysis). Several test were done on orbit for verify that the expected behavior was respected, from studying the thermal trends to use different selections to evaluate the correct events reconstruction and possible spectral features.

Through my prompt analysis several burst were revealed as GRB090902B, GRB091031A and GRB100325A. The first of these three is still the burst with the highest number of high energy ( $> 100$  MeV) photons ever observed. Thanks to the precise temporal and spatial resolution of the LAT, several interesting spectral characteristics were found. Their explanation is still matter of debate in the literature. The highest energy photon from GR090902B is also used for both constrain a really high ( $\sim 1000$ ) minimum value for the bulk Lorentz Factor of the ejecta (otherwise it would have been absorbed in the source) and also for test several model of extra galactic background light. GRB091031A and GRB100325A have a significance above  $4\sigma$  and they were studied using several statistical technique.

In this thesis is also described one of the most relevant discovery that *Fermi* has made, putting stringent constraint on a possible effect of the

Lorentz Invariance Violation. This was possible only using the joint analysis of the *Fermi* LAT and GBM data with the redshift value evaluated on the ground. This kind of analysis can be done only using cosmological sources that have a really short duration, otherwise this effect would be undetectable for its small scale and for the impossibility to determine exactly when each photon is emitted. In the last chapter the preliminary analysis on GRB091003 is described, it has shown interesting characteristics, as the expected long lasting high energy component, evident in all the *Fermi* LAT burst except one. Even if the photons associated to this burst are not so many with the standard selection, the possibility of particular spectral features is evaluated using several Monte Carlo simulations. In this way a significant improvement is found if the Band function has an high energy Cutoff around 1 MeV. This has to be further investigated but is really interesting since up to now only GRB090926A has shown an high energy cutoff.

## Appendix A

# Other space telescopes

### Agile

AGILE (Astro-rivelatore Gamma a Immagini LEggero)[198][199] was launched on April 23, 2007. The AGILE scientific payload is made of three detectors combined into one integrated instrument with broadband detection and imaging capabilities, the Data Handling (DH) systems complete the instrument. The gamma-ray imaging detector (GRID) is sensitive in the energy range  $\sim 30$  MeV–50 GeV, and consists of a Silicon–Tungsten Tracker, a Cesium Iodide Calorimeter, and the Anticoincidence system. The angular resolution at 100 MeV is characterized by a 68% containment radius of  $\sim 3.5^\circ$  for a large field of view (2.5 sr) and a good sensitivity (average effective area near 400 MeV of  $A_{eff} = 400$   $cm^2$ ) The hard X-ray imager (Super-AGILE) is an ultra-compact and light hard-X-ray imager composed by a coded-mask system made of a silicon detector plane and a thin tungsten mask positioned 14 cm above it. This imager is placed on top of the gamma-ray detector and is sensitive in the 18–60 keV band. It has an optimal angular resolution(6 arcmin) and a good sensitivity over a  $\sim 1$  sr FOV. It detects GRBs at a rate of 1 per month [200]. A Mini-Calorimeter (MCAL) operating in the *burst mode* is the third AGILE detector. It is part of the GRID, but also is capable of independently detecting GRBs and other transients in the 350 keV - 100 MeV energy range with optimal timing capabilities. It detects GRBs at a rate of 1 per week [200].

## Swift

The Swift [201] spacecraft lifted off aboard a Boeing Delta II rocket from Cape Canaveral November 20, 2004 and it has an orbital lifetime of  $\sim 8$  years. On the spacecraft there are three instruments; the Burst Alert Telescope (BAT [202]) that will search the sky for new GRBs and, upon discovery, will trigger an autonomous spacecraft slew to bring the burst into the X-Ray Telescope (XRT [203]) and Ultraviolet-Optical Telescope (UVOT [204]) fields of view (FOVs). Such autonomy will allow Swift to perform X-ray and UV/optical observations of more than 100 bursts  $yr^{-1}$  within 20–70 s of a burst detection, resulting in a current data set as of December 2008 of 380 bursts [25]. Of these, there are 126 with redshift determination, mostly from spectrographs on large optical telescopes and new robotic telescopes on the ground, possible thanks to the fast and precise localization of the source.

BAT is a highly sensitive, large FOV instrument designed to provide critical GRB triggers and 4 arcmin positions. It is a two-dimension codedmask instrument with a 1.4 sr FOV (half-coded). The energy range is 15–150 keV for imaging with a non coded response up to 500 keV. BAT's 32,768 pieces of  $4 \times 4 \times 2$  mm CdZnTe (CZT) form a  $1.2 \times 0.6$  m sensitive area in the detector plane. Within the first 10 s of detecting a burst, BAT will calculate an initial position, decide whether the burst merits a spacecraft slew, and, if worthy, send the position to the Swift spacecraft. Since the BAT coded FOV always includes the XRT and UVOT FOVs, long-duration gamma-ray emission from the burst can be studied simultaneously with the X-ray and UV/optical emission.

Swift's XRT is designed to measure the fluxes, spectra, and light curves of GRBs and afterglows over a wide dynamic range covering more than 7 orders of magnitude in flux. XRT is a focusing X-ray telescope with a  $110 \text{ cm}^2$  effective area, 23 arcmin FOV, 18 arcsec resolution (half-power diameter), and 0.2–10 keV energy range. The XRT will pinpoint GRBs to 5 arcsec accuracy within 10 s of target acquisition for a typical GRB and will study the X-ray counterparts of GRBs beginning 20–70 s from burst discovery and continuing for days to weeks. Allowing the study of the decay

curve of the afterglow in the X band of the interesting GRBS studying flares and possible breaks.

UVOT<sup>1</sup> is co-aligned with XRT and allows low-resolution grism spectra of bright GRBs and broadband UV/visible photometry. It's sensible to photons in the wavelength range between 170 and 650 nm. Its ultraviolet capability are not possible from the ground, and it cannot be clouded out. It is also much more sensitive than any other quick reaction telescope. UVOT observations enables optimal ground-based observations by providing rapid optical images of the GRB field so that any optical or infrared counterpart can be quickly identified and studied. If the GRB has a redshift between  $z \sim 1.3$  and  $z \sim 5$ , the filtered observations can also measure the photometric redshift of the GRB.

Each result is diffused by the Swift team in GCN notices and circulars, if the burst is of particular interest, as it was observed also by Fermi, a GRB Report<sup>2</sup> is created with updated analysis and results.

Given the small Field of View of XRT ( $23''.6 \times 23''.6$ ) and UVOT ( $17'' \times 17''$ ) a sub degrees localization is needed for localize a burst triggered by Fermi, the possible localization area will be spanned in search of the possible afterglow. Given the actual GBM localization error, only a LAT detection and on-ground localization is enough precise to be used by the Swift team<sup>3</sup>. A contemporaneous observation between both Fermi and Swift it is very helpful in the understanding of the physics behind the feature of GRBs, since several band of energy could be available, from UV to GeV  $\gamma$ -rays.

---

<sup>1</sup>[http://heasarc.gsfc.nasa.gov/docs/swift/about\\_swift/uvot\\_desc.html](http://heasarc.gsfc.nasa.gov/docs/swift/about_swift/uvot_desc.html)

<sup>2</sup>[http://gcn.gsfc.nasa.gov/report\\_archive.html](http://gcn.gsfc.nasa.gov/report_archive.html)

<sup>3</sup><http://www.swift.psu.edu/too.html>



# Acronyms

**ACD** Anticoincidence Detector

**AEM** ACD Electronics Module

**ARR** Autonomous Repoint Request

**BAP** Burst Alert Processor

**BAT** Burst Alert Telescope

**BATSE** Burst And Transient Source Experiment

**BGO** Bismuth Germanate Oxide

**BSPR** Blind Search Pattern Recognition

**CAL** Calorimeter

**CGRO** Compton Gamma-Ray Observatory

**COMPTEL** imaging COMPTton TELescope

**CRU** Command Response Unit

**CSPR** Calorimeter-Seeded Pattern Recognition

**CU** Calibration Unit

**DAQ** Data Acquisition System

**DPU** Data Processing Unit

**DRM** Detector Response Matrice

**EBL** Extra galactic Background Light

**EBM** Event Builder Module

**EGRET** Energetic Gamma-Ray Experiment Telescope

**EPU** Event Processor Unit

**FEE** Front-End Electronics

**FITS** Flexible Image Transport System

**FOV** Field Of View

**FREE** FRont End Electronics

**FSSC** Fermi Science Support Center

**FWHM** Full Width of Half Maximum

**GASU** Global-trigger / ACD-module / Signal distribution Unit

**GBM** GLAST Burst Monitor

**GCFE** GLAST Calorimeter Front-End

**GCN** Gamma-ray burst Coordinates Network

**GEM** Global-Trigger Electronics Module

**GLAST** Gamma-ray Large Area Space Telescope

**GIOC** GBM Instrument Operation Center

**GRB** Gamma-Ray Burst

**HIB** Heater Interface Boxes

**INTEGRAL** INTERnational Gamma-Ray Astrophysics Laboratory

**IRF** Instrument Response Function

**LAT** Large Area Telescope

**MIP** Minimum Ionizing Particle

**MOC** Mission Operations Center

**OSSE** Oriented Scintillation Spectrometer Experiment

**PDU** LAT's Power Distribution Unit

**PMT** Photo-Multiplier Tube

**PSF** Point Spread Function

**PPS** Pulse Per Second

**SAA** South Atlantic Anomaly

**SGR** Soft Gamma-ray Repeater

**SIU** Spacecraft Interface Unit

**TEM** Tower Electronics Module

**TKR** Tracker

**ToT** Time over Threshold

**TOO** Target Of Opportunity

**UVOT** UltraViolet/Optical Telescope

**WLS** WaveLength Shifting fibers

**XRT** X-Ray Telescope



# Bibliography

- [1] R. W. Klebesadel, I. B. Strong, and R. A. Olson. Observations of Gamma-Ray Bursts of Cosmic Origin. *The Astrophysical Journal Letters*, 182:L85+, June 1973.
- [2] N. Gehrels and J. K. Cannizzo. Gamma-ray telescopes. 400 Years of astronomical telescopes. *Experimental Astronomy*, 26:111–122, August 2009.
- [3] G. Schilling. *Flash! The Hunt for the Biggest Explosions in the Universe*. 2002.
- [4] C. A. Meegan et al. Spatial distribution of gamma-ray bursts observed by BATSE. *Nature*, 355:143–145, January 1992.
- [5] B. Paczynski and J. E. Rhoads. Radio Transients from Gamma-Ray Bursters. *The Astrophysical Journal Letters*, 418:L5+, November 1993.
- [6] E. Costa et al. Discovery of an X-ray afterglow associated with the  $\gamma$ -ray burst of 28 February 1997. *Nature*, 387:783–785, June 1997.
- [7] J. S. Bloom, S. G. Djorgovski, and S. R. Kulkarni. The Redshift and the Ordinary Host Galaxy of GRB 970228. *The Astrophysical Journal*, 554:678–683, June 2001.
- [8] E. Costa et al. GRB 970508. *IUAC*, 6649:1–+, May 1997.
- [9] M. R. Metzger et al. Spectral constraints on the redshift of the optical counterpart to the  $\gamma$ -ray burst of 8 May 1997. *Nature*, 387:878–880, June 1997.
- [10] T. J. Galama et al. The Radio-to-X-Ray Spectrum of GRB 970508 on 1997 May 21.0 UT. *The Astrophysical Journal Letters*, 500:L97+, June 1998.
- [11] G. R. Ricker et al. The High Energy Transient Explorer (HETE): Mission and Science Overview. In G. R. Ricker & R. K. Vanderspek, editor, *Gamma-Ray Burst and Afterglow Astronomy 2001: A Workshop Celebrating the First Year of the HETE Mission*, volume 662 of *American Institute of Physics Conference Series*, pages 3–16, April 2003.
- [12] F. Münz and G. Pizzichini. Burst statistics in HETE-2 catalogue. In *American Institute of Physics Conference Series*, volume 1111 of *American Institute of Physics Conference Series*, pages 387–390, May 2009.
- [13] R. Salvaterra et al. GRB090423 at a redshift of  $z \sim 8.1$ . *Nature*, 461:1258–1260, October 2009.
- [14] J. L. Racusin et al. Broadband observations of the naked-eye  $\gamma$ -ray burst GRB080319B. *Nature*, 455:183–188, September 2008.
- [15] D. Band et al. BATSE observations of gamma-ray burst spectra. I - Spectral diversity. *The Astrophysical Journal*, 413:281–292, August 1993.
- [16] Y. Kaneko et al. The Complete Spectral Catalog of Bright BATSE Gamma-Ray Bursts. *The Astrophysical Journal Supplement Series*, 166:298–340, September 2006.
- [17] R. D. Preece et al. The BATSE Gamma-Ray Burst Spectral Catalog. I. High Time Resolution Spectroscopy of Bright Bursts Using High Energy Resolution Data. *The Astrophysical Journal Supplement Series*, 126:19–36, January 2000.
- [18] B. Zhang and P. Meszaros. An Analysis of Gamma-Ray Burst Spectral Break Models. *The Astrophysical Journal*, 581:1236–1247, December 2002.
- [19] D. Grupe et al. Late-Time Detections of the X-Ray Afterglow of GRB 060729 with Chandra-The Latest Detections Ever of an X-Ray Afterglow. *The Astrophysical Journal*, 711:1008–1016, March 2010.

- [20] J. A. Nousek et al. Evidence for a Canonical Gamma-Ray Burst Afterglow Light Curve in the Swift XRT Data. *The Astrophysical Journal*, 642:389–400, May 2006.
- [21] J. L. Racusin et al. Jet Breaks and Energetics of Swift Gamma-Ray Burst X-Ray Afterglows. *The Astrophysical Journal*, 698:43–74, June 2009.
- [22] P. Mészáros. Gamma-ray bursts. *Reports on Progress in Physics*, 69:2259–2321, August 2006.
- [23] E.-W. Liang et al. A Comprehensive Analysis of Swift/X-Ray Telescope Data. IV. Single Power-Law Decaying Light Curves Versus Canonical Light Curves and Implications for a Unified Origin of X-Rays. *The Astrophysical Journal*, 707:328–342, December 2009.
- [24] E.-W. Liang et al. A Comprehensive Analysis of Swift XRT Data. III. Jet Break Candidates in X-Ray and Optical Afterglow Light Curves. *The Astrophysical Journal*, 675:528–552, March 2008.
- [25] N. Gehrels, E. Ramirez-Ruiz, and D.B. Fox. Gamma-ray bursts in the swift era. *Annual Review of Astronomy and Astrophysics*, 47(1):567–617, 2009.
- [26] G. Chincarini et al. The First Survey of X-Ray Flares from Gamma-Ray Bursts Observed by Swift: Temporal Properties and Morphology. *The Astrophysical Journal*, 671:1903–1920, December 2007.
- [27] B. L. Dingus. EGRET Observations of  $> 30$  MeV Emission from the Brightest Bursts Detected by BATSE. *Astrophysics and Space Science*, 231:187–190, September 1995.
- [28] M. Sommer et al. High-energy gamma rays from the intense 1993 January 31 gamma-ray burst. *The Astrophysical Journal Letters*, 422:L63–L66, February 1994.
- [29] M. M. González, B. L. Dingus, Y. Kaneko, R. D. Preece, C. D. Dermer, and M. S. Briggs. A  $\gamma$ -ray burst with a high-energy spectral component inconsistent with the synchrotron shock model. *Nature*, 424:749–751, August 2003.
- [30] Y. Kaneko et al. COMPTEL Observation of GRB941017 with Distinct High-Energy Component. In E. Fenimore & M. Galassi, editor, *Gamma-Ray Bursts: 30 Years of Discovery*, volume 727 of *American Institute of Physics Conference Series*, pages 244–247, September 2004.
- [31] K. Hurley et al. Detection of a  $\gamma$ -ray burst of very long duration and very high energy. *Nature*, 372:652–654, December 1994.
- [32] A. Giuliani et al. AGILE detection of delayed gamma-ray emission from GRB 080514B. *Astronomy & Astrophysics*, 491:L25–L28, November 2008.
- [33] G. F. Marani et al. On Similarities among GRBs. In *Bulletin of the American Astronomical Society*, volume 29 of *Bulletin of the American Astronomical Society*, pages 839–+, May 1997.
- [34] C. Kouveliotou et al. Identification of two classes of gamma-ray bursts. *The Astrophysical Journal Letters*, 413:L101–L104, August 1993.
- [35] T. M. Koshut et al. Systematic Effects on Duration Measurements of Gamma-Ray Bursts. *The Astrophysical Journal*, 463:570–+, June 1996.
- [36] J. P. Norris and J. T. Bonnell. Short Gamma-Ray Bursts with Extended Emission. *The Astrophysical Journal*, 643:266–275, May 2006.
- [37] L. G. Balázs et al. On the difference between the short and long gamma-ray bursts. *Astronomy & Astrophysics*, 401:129–140, April 2003.
- [38] I. Horváth, L. G. Balázs, Z. Bagoly, and P. Veres. Classification of Swift’s gamma-ray bursts. *Astronomy & Astrophysics*, 489:L1–L4, October 2008.
- [39] J. P. Norris, G. F. Marani, and J. T. Bonnell. Connection between Energy-dependent Lags and Peak Luminosity in Gamma-Ray Bursts. *The Astrophysical Journal*, 534:248–257, May 2000.
- [40] J. P. Norris, J. D. Scargle, and J. T. Bonnell. Short Gamma-Ray Bursts Are Different. In E. Costa, F. Frontera, & J. Hjorth, editor, *Gamma-ray Bursts in the Afterglow Era*, pages 40–+, 2001.

- [41] W. S. Paciesas et al. Spectral Properties of Short Gamma-Ray Bursts. In G. R. Ricker & R. K. Vanderspek, editor, *Gamma-Ray Burst and Afterglow Astronomy 2001: A Workshop Celebrating the First Year of the HETE Mission*, volume 662 of *American Institute of Physics Conference Series*, pages 248–251, April 2003.
- [42] A. Goldstein, R. D. Preece, and M. S. Briggs. A New Discriminator for Gamma-ray Burst Classification: The  $E_{peak}$ -fluence Energy Ratio. *The Astrophysical Journal*, 721:1329–1332, October 2010.
- [43] C. Kouveliotou et al. BATSE observations of the very intense gamma-ray burst GRB 930131. *The Astrophysical Journal Letters*, 422:L59–L62, February 1994.
- [44] B. Zhang et al. Discerning the Physical Origins of Cosmological Gamma-ray Bursts Based on Multiple Observational Criteria: The Cases of  $z = 6.7$  GRB 080913,  $z = 8.2$  GRB 090423, and Some Short/Hard GRBs. *The Astrophysical Journal*, 703:1696–1724, October 2009.
- [45] N. Gehrels et al. A short  $\gamma$ -ray burst apparently associated with an elliptical galaxy at redshift  $z = 0.225$ . *Nature*, 437:851–854, October 2005.
- [46] L. Amati et al. Intrinsic spectra and energetics of BeppoSAX Gamma-Ray Bursts with known redshifts. *Astronomy & Astrophysics*, 390:81–89, July 2002.
- [47] G. Ghirlanda et al. The Collimation-corrected Gamma-Ray Burst Energies Correlate with the Peak Energy of Their  $\nu F_\nu$  Spectrum. *The Astrophysical Journal*, 616:331–338, November 2004.
- [48] G. Ghirlanda, L. Nava, and G. Ghisellini. Spectral-luminosity relation within individual Fermi gamma rays bursts. *Astronomy & Astrophysics*, 511:A43+, February 2010.
- [49] G. Ghirlanda et al. Spectral evolution of Fermi/GBM short Gamma-Ray Bursts. *ArXiv e-prints*, August 2010.
- [50] D. Yonetoku et al. Gamma-Ray Burst Formation Rate Inferred from the Spectral Peak Energy-Peak Luminosity Relation. *The Astrophysical Journal*, 609:935–951, July 2004.
- [51] G. Ghirlanda et al. Short versus long gamma-ray bursts: spectra, energetics, and luminosities. *Astronomy & Astrophysics*, 496:585–595, March 2009.
- [52] T. J. Galama et al. An unusual supernova in the error box of the  $\gamma$ -ray burst of 25 April 1998. *Nature*, 395:670–672, October 1998.
- [53] C. Kouveliotou et al. Chandra Observations of the X-Ray Environs of SN 1998bw/GRB 980425. *The Astrophysical Journal*, 608:872–882, June 2004.
- [54] J. Hjorth et al. A very energetic supernova associated with the  $\gamma$ -ray burst of 29 March 2003. *Nature*, 423:847–850, June 2003.
- [55] B. E. Cobb et al. Discovery of SN 2009nz Associated with GRB 091127. *The Astrophysical Journal Letters*, 718:L150–L155, August 2010.
- [56] A. M. Soderberg, E. Nakar, E. Berger, and S. R. Kulkarni. Late-Time Radio Observations of 68 Type Ibc Supernovae: Strong Constraints on Off-Axis Gamma-Ray Bursts. *The Astrophysical Journal*, 638:930–937, February 2006.
- [57] A. M. Soderberg et al. A relativistic type Ibc supernova without a detected  $\gamma$ -ray burst. *Nature*, 463:513–515, January 2010.
- [58] Z. Paragi et al. A mildly relativistic radio jet from the otherwise normal type Ic supernova 2007gr. *Nature*, 463:516–518, January 2010.
- [59] J. P. U. an dothers Fynbo. No supernovae associated with two long-duration  $\gamma$ -ray bursts. *Nature*, 444:1047–1049, December 2006.
- [60] J. S. Bloom, S. R. Kulkarni, and S. G. Djorgovski. The Observed Offset Distribution of Gamma-Ray Bursts from Their Host Galaxies: A Robust Clue to the Nature of the Progenitors. *The Astronomical Journal*, 123:1111–1148, March 2002.
- [61] A. S. Fruchter and other. Long  $\gamma$ -ray bursts and core-collapse supernovae have different environments. *Nature*, 441:463–468, May 2006.
- [62] S. E. Woosley and J. S. Bloom. The Supernova Gamma-Ray Burst Connection. *Annual Review of Astronomy & Astrophysics*, 44:507–556, September 2006.

- [63] D. H. Hartmann. Gamma-ray bursts: A supernova connection. *Nature Physics*, 6:241–243, April 2010.
- [64] J. C. Wheeler, S. Akiyama, and P. T. Williams. Asymmetric Supernovae: Yes, Rotation and Magnetic Fields are Important. *Astrophysics and Space Science*, 298:3–8, July 2005.
- [65] W. H. Lee and E. Ramirez-Ruiz. The progenitors of short gamma-ray bursts. *New Journal of Physics*, 9:17–+, January 2007.
- [66] A. Burrows, E. Livne, L. Dessart, C. D. Ott, and J. Murphy. A New Mechanism for Core-Collapse Supernova Explosions. *The Astrophysical Journal*, 640:878–890, April 2006.
- [67] K. Iwamoto et al. A hypernova model for the supernova associated with the  $\gamma$ -ray burst of 25 April 1998. *Nature*, 395:672–674, October 1998.
- [68] K. Nomoto, K. Maeda, N. Tominaga, T. Ohkubo, J. Deng, and P. A. Mazzali. Hypernovae and Gamma-Ray Bursts. *Astrophysics and Space Science*, 298:81–86, July 2005.
- [69] A. V. Filippenko. Optical Spectra of Supernovae. *Annual Review of Astronomy and Astrophysics*, 35:309–355, 1997.
- [70] W. Zhang, S. E. Woosley, and A. Heger. The Propagation and Eruption of Relativistic Jets from the Stellar Progenitors of Gamma-Ray Bursts. *The Astrophysical Journal*, 608:365–377, June 2004.
- [71] D. Lazzati, B. J. Morsony, and M. C. Begelman. Short-duration Gamma-ray Bursts From Off-axis Collapsars. *The Astrophysical Journal*, 717:239–244, July 2010.
- [72] V. V. Usov. Millisecond pulsars with extremely strong magnetic fields as a cosmological source of gamma-ray bursts. *Nature*, 357:472–474, June 1992.
- [73] D. M. Palmer et al. A giant  $\gamma$ -ray flare from the magnetar SGR 1806 - 20. *Nature*, 434:1107–1109, April 2005.
- [74] E. Troja et al. Swift Observations of GRB 070110: An Extraordinary X-Ray Afterglow Powered by the Central Engine. *The Astrophysical Journal*, 665:599–607, August 2007.
- [75] T. A. Thompson, B. D. Metzger, and N. Bucciantini. Proto-Magnetars as GRB Central Engines: Uncertainties, Limitations, and Particulars. *ArXiv e-prints*, August 2010.
- [76] J. S. Bloom et al. Closing in on a Short-Hard Burst Progenitor: Constraints from Early-Time Optical Imaging and Spectroscopy of a Possible Host Galaxy of GRB 050509b. *The Astrophysical Journal*, 638:354–368, February 2006.
- [77] E. Berger. The Host Galaxies of Short-Duration Gamma-Ray Bursts: Luminosities, Metallicities, and Star-Formation Rates. *The Astrophysical Journal*, 690:231–237, January 2009.
- [78] R. Narayan, B. Paczynski, and T. Piran. Gamma-ray bursts as the death throes of massive binary stars. *The Astrophysical Journal Letters*, 395:L83–L86, August 1992.
- [79] E. Troja, A. R. King, P. T. O’Brien, N. Lyons, and G. Cusumano. Different progenitors of short hard gamma-ray bursts. *Monthly Notices of the Royal Astronomical Society*, 385:L10–L14, March 2008.
- [80] W. Fong, E. Berger, and D. B. Fox. Hubble Space Telescope Observations of Short Gamma-Ray Burst Host Galaxies: Morphologies, Offsets, and Local Environments. *The Astrophysical Journal*, 708:9–25, January 2010.
- [81] E. Berger. A Short Gamma-ray Burst "No-host" Problem? Investigating Large Progenitor Offsets for Short GRBs with Optical Afterglows. *The Astrophysical Journal*, 722:1946–1961, October 2010.
- [82] J. F. Graham et al. GRB 070714B Discovery of the Highest Spectroscopically Confirmed Short Burst Redshift. *The Astrophysical Journal*, 698:1620–1629, June 2009.
- [83] S. McBreen et al. Optical and near-infrared follow-up observations of four Fermi/LAT GRBs: redshifts, afterglows, energetics, and host galaxies. *Astronomy & Astrophysics*, 516:A71+, June 2010.
- [84] E. Ramirez-Ruiz and W. Lee. Gamma-ray bursts: Maybe not so old after all. *Nature*, 460:1091–1092, August 2009.
- [85] P. N. Bhat et al. Evidence of sub-millisecond structure in a gamma-ray burst. *Nature*, 359:217–+, September 1992.

- [86] E. Ramirez-Ruiz and A. Socrates. Supernovae and Gamma-Ray Bursts Powered by Hot Neutrino-Cooled Coronae. *ArXiv Astrophysics e-prints*, April 2005.
- [87] R. Mochkovitch, M. Hernanz, J. Isern, and X. Martin. Gamma-ray bursts as collimated jets from neutron star/black hole mergers. *Nature*, 361:236–238, January 1993.
- [88] C. L. Fryer and P. Mészáros. Neutrino-driven Explosions in Gamma-Ray Bursts and Hypernovae. *The Astrophysical Journal Letters*, 588:L25–L28, May 2003.
- [89] R. D. Blandford and R. L. Znajek. Electromagnetic extraction of energy from Kerr black holes. *Monthly Notices of the Royal Astronomical Society*, 179:433–456, May 1977.
- [90] R. D. Blandford and D. G. Payne. Hydromagnetic flows from accretion discs and the production of radio jets. *Monthly Notices of the Royal Astronomical Society*, 199:883–903, June 1982.
- [91] R. D. Blandford. To the Lighthouse. In M. Gilfanov, R. Sunyaev, & E. Churazov, editor, *Lighthouses of the Universe: The Most Luminous Celestial Objects and Their Use for Cosmology*, pages 381–+, 2002.
- [92] R. C. Duncan and C. Thompson. Formation of very strongly magnetized neutron stars - Implications for gamma-ray bursts. *The Astrophysical Journal Letters*, 392:L9–L13, June 1992.
- [93] Y.-Z. Qian and S. E. Woosley. Nucleosynthesis in Neutrino-driven Winds. I. The Physical Conditions. *The Astrophysical Journal*, 471:331–+, November 1996.
- [94] R. Abbasi et al. Search for Muon Neutrinos from Gamma-ray Bursts with the IceCube Neutrino Telescope. *The Astrophysical Journal*, 710:346–359, February 2010.
- [95] A. M. Beloborodov. Collisional mechanism for gamma-ray burst emission. *Monthly Notices of the Royal Astronomical Society*, 407:1033–1047, September 2010.
- [96] A. Achterberg, Y. A. Gallant, J. G. Kirk, and A. W. Guthmann. Particle acceleration by ultrarelativistic shocks: theory and simulations. *Monthly Notices of the Royal Astronomical Society*, 328:393–408, December 2001.
- [97] P. Kumar and R. Barniol Duran. On the generation of high-energy photons detected by the Fermi Satellite from gamma-ray bursts. *Monthly Notices of the Royal Astronomical Society*, 400:L75–L79, November 2009.
- [98] G. B. Rybicki and A. P. Lightman. *Radiative processes in astrophysics*. 1979.
- [99] R. D. Preece et al. The Synchrotron Shock Model Confronts a “Line of Death” in the BATSE Gamma-Ray Burst Data. *The Astrophysical Journal Letters*, 506:L23–L26, October 1998.
- [100] NASA Goddard Space Flight Center 433-SRD-0001. Glast project science requirements document, September 2000.
- [101] W. B. Atwood et al. The Large Area Telescope on the Fermi Gamma-Ray Space Telescope Mission. *The Astrophysical Journal*, 697:1071–1102, June 2009.
- [102] C. Meegan et al. The Fermi Gamma-ray Burst Monitor. *The Astrophysical Journal*, 702:791–804, September 2009.
- [103] D. J. Thompson et al. Calibration of the Energetic Gamma-Ray Experiment Telescope (EGRET) for the Compton Gamma-Ray Observatory. *The Astrophysical Journal Supplement Series*, 86:629–656, June 1993.
- [104] L. Baldini et al. Preliminary results of the LAT Calibration Unit beam tests. In S. Ritz, P. Michelson, & C. A. Meegan, editor, *The First GLAST Symposium*, volume 921 of *American Institute of Physics Conference Series*, pages 190–204, July 2007.
- [105] S. Germani. Preliminary results from the GLAST silicon tracker beam test. *Nuclear Instruments and Methods in Physics Research A*, 582:898–901, December 2007.
- [106] C. Monte. *Performance of the Fermi Large Area Telescope for the detection of cosmic gamma-rays*. PhD thesis, Università di Bari, 2009.
- [107] A. A. Moiseev et al. Observation and simulations of the backscplash effects in high-energy  $\gamma$ -ray telescopes containing a massive calorimeter. *Astroparticle Physics*, 22:275–283, November 2004.

- [108] A. A. Moiseev et al. The anti-coincidence detector for the GLAST large area telescope. *Astroparticle Physics*, 27:339–358, June 2007.
- [109] A. A. Moiseev et al. High efficiency plastic scintillator detector with wavelength-shifting fiber readout for the GLAST Large Area Telescope. *Nuclear Instruments and Methods in Physics Research A*, 583:372–381, December 2007.
- [110] W. B. Atwood et al. Design and initial tests of the Tracker-converter of the Gamma-ray Large Area Space Telescope. *Astroparticle Physics*, 28:422–434, December 2007.
- [111] W. N. Johnson et al. CsI Hodoscopic Calorimeter for the GLAST Mission. In *Bulletin of the American Astronomical Society*, volume 31 of *Bulletin of the American Astronomical Society*, pages 735–+, April 1999.
- [112] J. Eric Grove et al. The Calorimeter of the Fermi Large Area Telescope. 2010.
- [113] S. Bergenius Gavler et al. Radiation tests of CsI(Tl) crystals for the GLAST satellite mission. *Nuclear Instruments and Methods in Physics Research A*, 545:842–851, June 2005.
- [114] P. Carlson, T. Francke, C. Fuglesang, N. Weber, and M. Suffert. Long narrow CsI(Tl) rods as calorimeter elements. *Nuclear Instruments and Methods in Physics Research A*, 376:271–274, February 1996.
- [115] W. Neil Johnson et al. The building of Fermi-LAT. 2010.
- [116] S. Agostinelli et al. G4—a simulation toolkit. *Nuclear Instruments and Methods in Physics Research Section A: Accelerators, Spectrometers, Detectors and Associated Equipment*, 506(3):250 – 303, 2003.
- [117] R. Frühwirth, M. Regler, R. K. Bock, H. Grote, and D. Notz. *Data Analysis Techniques for High-Energy Physics*. August 2000.
- [118] Leo Breiman, J. H. Friedman, R. A. Olshen, and C. J. Stone. *Classification and Regression Trees*. Wadsworth, 1984.
- [119] P. Sreekumar et al. EGRET Observations of the Extragalactic Gamma-Ray Emission. *The Astrophysical Journal*, 494:523–+, February 1998.
- [120] J. E. Davis. The Formal Underpinnings of the Response Functions Used in X-Ray Spectral Analysis. *The Astrophysical Journal*, 548:1010–1019, February 2001.
- [121] R. Rando and for the Fermi LAT Collaboration. Post-launch performance of the Fermi Large Area Telescope. *ArXiv e-prints*, July 2009.
- [122] Global positioning system standard positioning service performance standard , fourth ed., September 2008.
- [123] L. Kuiper, W. Hermsen, R. Walter, and L. Foschini. Absolute timing with IBIS, SPI and JEM-X aboard INTEGRAL. Crab main-pulse arrival times in radio, X-rays and high-energy gamma -rays. *Astronomy & Astrophysics*, 411:L31–L36, November 2003.
- [124] R. J. Hanisch, A. Farris, E. W. Greisen, W. D. Pence, B. M. Schlesinger, P. J. Teuben, R. W. Thompson, and A. Warnock, III. Definition of the Flexible Image Transport System (FITS). *Astronomy & Astrophysics*, 376:359–380, September 2001.
- [125] F. Kuehn et al. LAT Onboard Science: Gamma-Ray Burst Identification. In S. Ritz, P. Michelson, & C. A. Meegan, editor, *The First GLAST Symposium*, volume 921 of *American Institute of Physics Conference Series*, pages 556–557, July 2007.
- [126] J. McEnery et al. Update to the configuration of the Fermi-LAT onboard GRB search. *GRB Coordinates Network, Circular Service*, 10777, pages 1–+, 2010.
- [127] C. Kouveliotou et al. Search for soft gamma repeaters in the SMM/HXRBS data. *The Astrophysical Journal*, 392:179–186, June 1992.
- [128] M. S. Briggs et al. The Accuracy of GBM GRB Locations. In *American Institute of Physics Conference Series*, volume 1133, pages 40–42, May 2009.
- [129] W. Cash. Parameter estimation in astronomy through application of the likelihood ratio. *The Astrophysical Journal*, 228:939–947, March 1979.
- [130] S. Barthelmy. <http://gcn.gsfc.nasa.gov/>.

- [131] J. Granot et al. Highlights from Fermi GRB observations. *ArXiv e-prints*, March 2010.
- [132] H. Takahashi et al. GRB100414A: Fermi LAT detection. *GRB Coordinates Network, Circular Service*, 10594, 1 (2010), 594:1–+, 2010.
- [133] M. Ohno. Fermi Observations of Gamma-ray Bursts. In *American Institute of Physics Conference Series*, volume 1279 of *American Institute of Physics Conference Series*, pages 9–12, October 2010.
- [134] G. Ghisellini et al. GeV emission from gamma-ray bursts: a radiative fireball? *Monthly Notices of the Royal Astronomical Society*, 403:926–937, April 2010.
- [135] B.-B. Zhang et al. A Comprehensive Analysis of Fermi Gamma-Ray Burst Data. I. Spectral Components and Their Possible Physical Origins of LAT/GBM GRBs. *ArXiv e-prints*, September 2010.
- [136] C. W. Akerlof, W. Zheng, S. B. Pandey, and T. A. McKay. Searching for Needles in Haystacks - Using the Fermi/GBM to Find GRB  $\gamma$ -rays with the Fermi/LAT Detector. *The Astrophysical Journal Letters*, 725:L15–L18, December 2010.
- [137] T. Uehara. Fermi view of the bright long GRB 090926A. In *American Institute of Physics Conference Series*, volume 1279 of *American Institute of Physics Conference Series*, pages 451–453, October 2010.
- [138] T. Piran. The physics of gamma-ray bursts. *Reviews of Modern Physics*, 76:1143–1210, October 2004.
- [139] J. Granot et al. Opacity Buildup in Impulsive Relativistic Sources. *The Astrophysical Journal*, 677:92–126, April 2008.
- [140] K. Toma et al. An Up-Scattered Cocoon Emission Model of Gamma-Ray Burst High-Energy Lags. *The Astrophysical Journal*, 707:1404–1416, December 2009.
- [141] K. Toma, X.-F. Wu, and P. Meszaros. A Photosphere-Internal Shock Model of Gamma-Ray Bursts: Case Studies of Fermi/LAT Bursts. *ArXiv e-prints*, February 2010.
- [142] S. Razzaque, C. D. Dermer, and J. D. Finke. Synchrotron Radiation from Ultra-High Energy Protons and the Fermi Observations of GRB 080916C. *The Open Astronomy Journal*, 3:150–155, August 2010.
- [143] K. Asano, S. Guiriec, and P. Mészáros. Hadronic Models for the Extra Spectral Component in the Short GRB 090510. *The Astrophysical Journal Letters*, 705:L191–L194, November 2009.
- [144] P. Kumar and R. Barniol Duran. External forward shock origin of high-energy emission for three gamma-ray bursts detected by Fermi. *Monthly Notices of the Royal Astronomical Society*, 409:226–236, November 2010.
- [145] J. E. McEnery. Fermi LAT Observations of High Energy Gamma-Ray Burst Afterglows. In *American Astronomical Society Meeting Abstracts*, volume 215 of *American Astronomical Society Meeting Abstracts*, page 207.03, January 2010.
- [146] E. Bissaldi and V. Connaughton. GRB 090902B: Fermi GBM detection of a bright burst. *GRB Coordinates Network*, 9866:1–+, 2009.
- [147] G. Stratta et al. Swift Observations of Fermi-LAT GRB 090902B. *GCN Report*, 249:1–+, 2009.
- [148] S. B. Pandey et al. GRB 090902B: ROTSE-III detection of optical afterglow. *GRB Coordinates Network*, 9878:1–+, 2009.
- [149] Y. Terada et al. GRB 090902B: Suzaku WAM observation of the prompt emission. *GRB Coordinates Network*, 9897:1–+, 2009.
- [150] D. A. Perley et al. GRB 090902B: optical afterglow candidate. *GRB Coordinates Network*, 9870:1–+, 2009.
- [151] F. Olivares et al. GRB 090902B: GROND NIR afterglow observations. *GRB Coordinates Network*, 9874:1–+, 2009.
- [152] A. J. van der Horst et al. GRB 090902B: WSRT Radio Observation. *GRB Coordinates Network*, 9883:1–+, 2009.

- [153] P. Chandra et al. GRB 090902B: VLA radio detection. *GRB Coordinates Network*, 9889:1–+, 2009.
- [154] A. Cucchiara et al. GRB 090902B: Gemini-N absorption redshift. *GRB Coordinates Network*, 9873:1–+, 2009.
- [155] Y. Lithwick and R. Sari. Lower Limits on Lorentz Factors in Gamma-Ray Bursts. *The Astrophysical Journal*, 555:540–545, July 2001.
- [156] K. Asano, S. Inoue, and P. Mészáros. Prompt High-Energy Emission from Proton-Dominated Gamma-Ray Bursts. *The Astrophysical Journal*, 699:953–957, July 2009.
- [157] A. Pe’er et al. The Connection Between Thermal and Non-Thermal Emission in Gamma-ray Bursts: General Considerations and GRB090902B as a Case Study. *ArXiv e-prints*, July 2010.
- [158] A. Pe’er and F. Ryde. A Theory of Multicolor Black Body Emission from Relativistically Expanding Plasmas. *ArXiv e-prints*, August 2010.
- [159] K. Ioka. Very High Lorentz Factor Fireballs and Gamma-Ray Burst Spectra. *Progress of Theoretical Physics*, 124:667–710, October 2010.
- [160] S. B. Pandey et al. GRB 090902B: Afterglow Observations and Implications. *The Astrophysical Journal*, 714:799–804, May 2010.
- [161] S. B. Cenko et al. Afterglow Observations of Fermi-LAT Gamma-Ray Bursts and the Emerging Class of Hyper-Energetic Events. *ArXiv e-prints*, April 2010.
- [162] S. Y. Feng and Z. G. Dai. Multiband Fitting to Three Long GRBs with Fermi/LAT Data: Structured Ejecta Sweeping up a Density-Jump Medium. *ArXiv e-prints*, November 2010.
- [163] T. Piran and E. Nakar. On the External Shock Synchrotron Model for Gamma-ray Bursts’ GeV Emission. *The Astrophysical Journal Letters*, 718:L63–L67, August 2010.
- [164] R.-Y. Liu and X.-Y. Wang. Modeling the broadband emission of Fermi/LAT GRB 090902B. *ArXiv e-prints*, September 2010.
- [165] H.-N. He et al. On the High Energy Emission of the Short GRB 090510. *ArXiv e-prints*, September 2010.
- [166] A. Corsi et al. High-energy Emission Components in the Short GRB 090510. *The Astrophysical Journal*, 720:1008–1015, September 2010.
- [167] F. W. Stecker, M. A. Malkan, and S. T. Scully. Intergalactic Photon Spectra from the Far-IR to the UV Lyman Limit for  $0 < z < 6$  and the Optical Depth of the Universe to High-Energy Gamma Rays. *The Astrophysical Journal*, 648:774–783, September 2006.
- [168] S. McBreen and V. Chaplin. GRB 091031: Fermi GBM detection. *GRB Coordinates Network, Circular Service*, 10115, 1 (2009), 115:1–+, 2009.
- [169] T.-P. Li and Y.-Q. Ma. Analysis methods for results in gamma-ray astronomy. *The Astrophysical Journal*, 272:317–324, September 1983.
- [170] S. Golenetskii et al. Konus-wind and Konus-RF observations of GRB 091031. *GRB Coordinates Network, Circular Service*, 10166, 1 (2009), 166:1–+, 2009.
- [171] A. von Kienlin. GRB 100325A: Fermi GBM detection. *GRB Coordinates Network, Circular Service*, 10546, 1 (2010), 546:1–+, 2010.
- [172] M. Ohno and V. Pelassa. Fermi LAT detection of GRB 090510. *GRB Coordinates Network*, 9334:1–+, 2009.
- [173] S. Guiriec, V. Connaughton, and M. Briggs. GRB 090510: Fermi GBM detection. *GRB Coordinates Network*, 9336:1–+, 2009.
- [174] A. Giuliani et al. AGILE Detection of Delayed Gamma-ray Emission From the Short Gamma-Ray Burst GRB 090510. *The Astrophysical Journal Letters*, 708:L84–L88, January 2010.
- [175] G. Ghirlanda, G. Ghisellini, and L. Nava. The onset of the GeV afterglow of GRB 090510. *Astronomy & Astrophysics*, 510:L7+, February 2010.

- [176] A. Rau, S. McBreen, and T. Kruehler. GRB090510: VLT/FORS2 spectroscopic redshift. *GRB Coordinates Network*, 9353:1–+, 2009.
- [177] G. Amelino-Camelia et al. Tests of quantum gravity from observations of  $\gamma$ -ray bursts. *Nature*, 393:763–765, June 1998.
- [178] V. A. Kostelecký and M. Mewes. Astrophysical Tests of Lorentz and CPT Violation with Photons. *The Astrophysical Journal Letters*, 689:L1–L4, December 2008.
- [179] G. Amelino-Camelia and L. Smolin. Prospects for constraining quantum gravity dispersion with near term observations. *Physical Review D*, 80(8):084017–+, October 2009.
- [180] J. D. Scargle, J. P. Norris, and J. T. Bonnell. An Algorithm for Detecting Quantum Gravity Photon Dispersion in Gamma-Ray Bursts: DisCan. *The Astrophysical Journal*, 673:972–980, February 2008.
- [181] J. Albert et al. Probing quantum gravity using photons from a flare of the active galactic nucleus Markarian 501 observed by the MAGIC telescope. *Physics Letters B*, 668:253–257, October 2008.
- [182] J. Ellis et al. Derivation of a vacuum refractive index in a stringy space time foam model. *Physics Letters B*, 665:412–417, July 2008.
- [183] K. G. Zloshchastiev. Logarithmic nonlinearity in generally covariant quantum theories: Origin of time and observational consequences. *ArXiv e-prints*, June 2009.
- [184] E. Troja et al. Precursors of Short Gamma-ray Bursts. *The Astrophysical Journal*, 723:1711–1717, November 2010.
- [185] A. Rau. GRB 091003A: Fermi GBM detection. *GRB Coordinates Network*, 9983:1–+, 2009.
- [186] J. McEnery, J. Chiang, and Y. Hanabata. GRB 091003A: Fermi LAT detection. *GRB Coordinates Network*, 9985:1–+, 2009.
- [187] S. Golenetskii et al. Konus-wind observation of GRB 091003A. *GRB Coordinates Network*, 9994:1–+, 2009.
- [188] K. Kono et al. GRB 091003A: Suzaku WAM observation of the prompt emission. *GRB Coordinates Network*, 9998:1–+, 2009.
- [189] R. L. C. Starling et al. Swift observations of GRB 091003. *GCN Report*, 253:1–+, 2009.
- [190] R. L. C. Starling, P. A. Evans, A. P. Beardmore, and M. R. Goad. GRB 091003: UVOT-enhanced XRT position. *GRB Coordinates Network*, 9988:1–+, 2009.
- [191] K. Wiersema et al. GRB 091003: WHT ACAM observations. *GRB Coordinates Network*, 9995:1–+, 2009.
- [192] D. A. Perley et al. GRB 091003: Lick observations and possible SDSS host galaxy. *GRB Coordinates Network*, 9997:1–+, 2009.
- [193] A. Cucchiara et al. GRB 091003: Gemini-N redshift of possible host galaxy. *GRB Coordinates Network, Circular Service, 1031, 1 (2009)*, 31:1–+, 2009.
- [194] S. S. Wilks. The Large-Sample Distribution of the Likelihood Ratio for Testing Composite Hypotheses. *The Annals of Mathematical Statistics*, 9:60–62, March 1938. <http://www.jstor.org/stable/2957648>.
- [195] K. A. Arnaud. Parameter estimation in X-ray astronomy in the Chandra and XMM-Newton era. *The Astrophysical Journal (submitted)*, 2003. <http://heasarc.gsfc.nasa.gov/docs/xanadu/xspec/wstat.ps>.
- [196] N. Gehrels. Confidence limits for small numbers of events in astrophysical data. *The Astrophysical Journal*, 303:336–346, April 1986.
- [197] J. R. Mattox et al. The Likelihood Analysis of EGRET Data. *The Astrophysical Journal*, 461:396–+, April 1996.
- [198] M. Tavani et al. The AGILE space mission. *Nuclear Instruments and Methods in Physics Research A*, 588:52–62, April 2008.
- [199] M. Tavani et al. The AGILE Mission. *Astronomy & Astrophysics*, 502:995–1013, August 2009.

- [200] E. Striani and M. Tavani. The AGILE Mission: the first 2 years. In C. Cecchi, S. Ciprini, P. Lubrano, & G. Tosti, editor, *American Institute of Physics Conference Series*, volume 1223 of *American Institute of Physics Conference Series*, pages 23–32, March 2010.
- [201] N. Gehrels et al. The Swift Gamma-Ray Burst Mission. *The Astrophysical Journal*, 611:1005–1020, August 2004.
- [202] S. D. Barthelmy et al. The Burst Alert Telescope (BAT) on the SWIFT Midex Mission. *Space Science Reviews*, 120:143–164, October 2005.
- [203] D. N. Burrows et al. The Swift X-Ray Telescope. *Space Science Reviews*, 120:165–195, October 2005.
- [204] P. W. A. Roming et al. The Swift Ultra-Violet/Optical Telescope. *Space Science Reviews*, 120:95–142, October 2005.

# Publications on reviews with international advisory editorial board

- [205] A. A. Abdo et al. Search for Gamma-ray Emission from Magnetars with the Fermi Large Area Telescope. *The Astrophysical Journal Letters*, 725:L73–L78, December 2010.
- [206] F. Ryde et al. Identification and Properties of the Photospheric Emission in GRB090902B. *The Astrophysical Journal Letters*, 709:L172–L177, February 2010.
- [207] A. A. Abdo et al. The on-orbit calibration of the Fermi Large Area Telescope. *Astroparticle Physics*, 32:193–219, October 2009.
- [208] A. A. Abdo et al. Measurement of the Cosmic Ray  $e^+ + e^-$  Spectrum from 20GeV to 1TeV with the Fermi Large Area Telescope. *Physical Review Letters*, 102(18):181101–+, May 2009.
- [209] D. L. Band et al. Prospects for GRB Science with the Fermi Large Area Telescope. *The Astrophysical Journal*, 701:1673–1694, August 2009.
- [210] A. A. Abdo et al. Fermi Large Area Telescope Observations of the Crab Pulsar And Nebula. *The Astrophysical Journal*, 708:1254–1267, January 2010.
- [211] A. A. Abdo et al. Fermi Large Area Telescope Observations of the Vela Pulsar. *The Astrophysical Journal*, 696:1084–1093, May 2009.
- [212] A. A. Abdo et al. Pulsed Gamma Rays from the Millisecond Pulsar J0030+0451 with the Fermi Large Area Telescope. *The Astrophysical Journal*, 699:1171–1177, July 2009.
- [213] A. A. Abdo et al. Fermi Observations of High-Energy Gamma-Ray Emission from GRB 080916C. *Science*, 323:1688–, March 2009.
- [214] A. A. Abdo et al. Fermi Observations of GRB 090902B: A Distinct Spectral Component in the Prompt and Delayed Emission. *The Astrophysical Journal Letters*, 706:L138–L144, November 2009.
- [215] A. A. Abdo et al. Fermi Detection of Delayed GeV Emission from the Short Gamma-Ray Burst 081024B. *The Astrophysical Journal*, 712:558–564, March 2010.
- [216] M. Ackermann et al. Fermi Observations of GRB 090510: A Short-Hard Gamma-ray Burst with an Additional, Hard Power-law Component from 10 keV TO GeV Energies. *The Astrophysical Journal*, 716:1178–1190, June 2010.
- [217] A. A. Abdo et al. Fermi Observations of High-energy Gamma-ray Emission from GRB 080825C. *The Astrophysical Journal*, 707:580–592, December 2009.
- [218] M. De Pasquale et al. Swift and Fermi Observations of the Early Afterglow of the Short Gamma-Ray Burst 090510. *The Astrophysical Journal Letters*, 709:L146–L151, February 2010.
- [219] M. Ackermann et al. Fermi Observations of High-energy Gamma-ray Emission from GRB 090217A. *The Astrophysical Journal Letters*, 717:L127–L132, July 2010.
- [220] A. A. Abdo et al. Fermi Large Area Telescope Constraints on the Gamma-ray Opacity of the Universe. *The Astrophysical Journal*, 723:1082–1096, November 2010.

- [221] A. A. Abdo et al. A limit on the variation of the speed of light arising from quantum gravity effects. *Nature*, 462:331–334, November 2009.
- [222] A. A. Abdo et al. Fermi Large Area Telescope First Source Catalog. *The Astrophysical Journal Supplement Series*, 188:405–436, June 2010.
- [223] A. A. Abdo et al. The Fermi Gamma-Ray Space Telescope Discovers the Pulsar in the Young Galactic Supernova Remnant CTA 1. *Science*, 322:1218–, November 2008.
- [224] F. Aharonian et al. Simultaneous Observations of PKS 2155-304 with HESS, Fermi, RXTE, and Atom: Spectral Energy Distributions and Variability in a Low State. *The Astrophysical Journal Letters*, 696:L150–L155, May 2009.
- [225] A. A. Abdo et al. Discovery of Pulsed  $\gamma$ -Rays from the Young Radio Pulsar PSR J1028-5819 with the Fermi Large Area Telescope. *The Astrophysical Journal Letters*, 695:L72–L77, April 2009.
- [226] A. A. Abdo et al. Fermi/Large Area Telescope Discovery of Gamma-Ray Emission from the Flat-Spectrum Radio Quasar PKS 1454-354. *The Astrophysical Journal*, 697:934–941, May 2009.
- [227] A. A. Abdo et al. Fermi Discovery of Gamma-ray Emission from NGC 1275. *The Astrophysical Journal*, 699:31–39, July 2009.
- [228] A. A. Abdo et al. Early Fermi Gamma-ray Space Telescope Observations of the Quasar 3C 454.3. *The Astrophysical Journal*, 699:817–823, July 2009.
- [229] A. A. Abdo et al. Fermi/Large Area Telescope Discovery of Gamma-Ray Emission from a Relativistic Jet in the Narrow-Line Quasar PMN J0948+0022. *The Astrophysical Journal*, 699:976–984, July 2009.
- [230] A. A. Abdo et al. Discovery of Pulsations from the Pulsar J0205+6449 in SNR 3C 58 with the Fermi Gamma-Ray Space Telescope. *The Astrophysical Journal Letters*, 699:L102–L107, July 2009.
- [231] A. A. Abdo et al. Bright Active Galactic Nuclei Source List from the First Three Months of the Fermi Large Area Telescope All-Sky Survey. *The Astrophysical Journal*, 700:597–622, July 2009.
- [232] A. A. Abdo et al. Fermi/Large Area Telescope Bright Gamma-Ray Source List. *The Astrophysical Journal Supplement Series*, 183:46–66, July 2009.
- [233] A. A. Abdo et al. Pulsed Gamma-rays from PSR J2021+3651 with the Fermi Large Area Telescope. *The Astrophysical Journal*, 700:1059–1066, August 2009.
- [234] A. A. Abdo et al. Fermi LAT Observations of LS I +61 deg 303: First Detection of an Orbital Modulation in GeV Gamma Rays. *The Astrophysical Journal Letters*, 701:L123–L128, August 2009.
- [235] A. A. Abdo et al. Detection of 16 Gamma-Ray Pulsars Through Blind Frequency Searches Using the Fermi LAT. *Science*, 325:840–, August 2009.
- [236] A. A. Abdo et al. Detection of High-Energy Gamma-Ray Emission from the Globular Cluster 47 Tucanae with Fermi. *Science*, 325:845–, August 2009.
- [237] A. A. Abdo et al. A Population of Gamma-Ray Millisecond Pulsars Seen with the Fermi Large Area Telescope. *Science*, 325:848–, August 2009.
- [238] A. A. Abdo et al. Fermi LAT Observation of Diffuse Gamma Rays Produced Through Interactions Between Local Interstellar Matter and High-energy Cosmic Rays. *The Astrophysical Journal*, 703:1249–1256, October 2009.
- [239] A. A. Abdo et al. Fermi LAT Discovery of Extended Gamma-Ray Emission in the Direction of Supernova Remnant W51C. *The Astrophysical Journal Letters*, 706:L1–L6, November 2009.
- [240] A. A. Abdo et al. Fermi/LAT observations of LS 5039. *The Astrophysical Journal Letters*, 706:L56–L61, November 2009.
- [241] A. A. Abdo et al. Fermi Large Area Telescope Detection of Pulsed  $\gamma$ -rays from the Vela-like Pulsars PSR J1048-5832 and PSR J2229+6114. *The Astrophysical Journal*, 706:1331–1340, December 2009.
- [242] A. A. Abdo et al. Fermi Large Area Telescope Gamma-Ray Detection of the Radio Galaxy M87. *The Astrophysical Journal*, 707:55–60, December 2009.

- [243] A. A. Abdo et al. Multiwavelength Monitoring of the Enigmatic Narrow-Line Seyfert 1 PMN J0948+0022 in 2009 March–July. *The Astrophysical Journal*, 707:727–737, December 2009.
- [244] A. A. Abdo et al. Fermi Observations of TeV-Selected Active Galactic Nuclei. *The Astrophysical Journal*, 707:1310–1333, December 2009.
- [245] A. A. Abdo et al. Radio-Loud Narrow-Line Seyfert 1 as a New Class of Gamma-Ray Active Galactic Nuclei. *The Astrophysical Journal Letters*, 707:L142–L147, December 2009.
- [246] A. A. Abdo et al. Fermi large area telescope observations of the cosmic-ray induced  $\gamma$ -ray emission of the Earth’s atmosphere. *Physical Review D*, 80(12):122004–+, December 2009.
- [247] A. A. Abdo et al. Fermi large area telescope measurements of the diffuse gamma-ray emission at intermediate galactic latitudes. *Physical Review Letters*, 103(25):251101, December 2009.
- [248] A. A. Abdo et al. Modulated high-energy gamma-ray emission from the microquasar Cygnus X-3. *Science*, 326:1512–1516, December 2009.
- [249] A. A. Abdo et al. Fermi Observations of the Very Hard Gamma-ray Blazar PG 1553+113. *The Astrophysical Journal*, 708:1310–1320, January 2010.
- [250] P. Weltevrede et al. Gamma-ray and Radio Properties of Six Pulsars Detected by the Fermi Large Area Telescope. *The Astrophysical Journal*, 708(2):1426–1441, January 2010.
- [251] V. A. Acciari et al. Discovery of Very High Energy Gamma Rays from PKS 1424+240 and Multiwavelength Constraints on Its Redshift. *The Astrophysical Journal Letters*, 708(2):L100–L106, January 2010.
- [252] A. A. Abdo et al. Detection of Gamma-Ray Emission from the Starburst Galaxies M82 and NGC 253 with the Large Area Telescope on Fermi. *The Astrophysical Journal Letters*, 709:L152–L157, February 2010.
- [253] A. A. Abdo et al. Fermi Observations of Cassiopeia and Cepheus: Diffuse Gamma-ray Emission in the Outer Galaxy. *The Astrophysical Journal*, 710:133–149, February 2010.
- [254] A. A. Abdo et al. PKS 1502+106: A New and Distant Gamma-ray Blazar in Outburst Discovered by the Fermi Large Area Telescope. *The Astrophysical Journal*, 710:810–827, February 2010.
- [255] A. A. Abdo et al. Spectral Properties of Bright Fermi-Detected Blazars in the Gamma-Ray Band. *The Astrophysical Journal*, 710:1271–1285, February 2010.
- [256] A. A. Abdo et al. Fermi-Lat Discovery of GeV Gamma-Ray Emission from the Young Supernova Remnant Cassiopeia A. *The Astrophysical Journal Letters*, 710:L92–L97, February 2010.
- [257] Fermi-Lat Collaboration, Members Of The 3C 279 Multi-Band Campaign, et al. A change in the optical polarization associated with a  $\gamma$ -ray flare in the blazar 3C279. *Nature*, 463:919–923, February 2010.
- [258] A. A. Abdo et al. Gamma-Ray Emission from the Shell of Supernova Remnant W44 Revealed by the Fermi LAT. *Science*, 327:1103–, February 2010.
- [259] A. A. Abdo et al. Observations of the Large Magellanic Cloud with Fermi. *Astronomy & Astrophysics*, 512:A7+, March 2010.
- [260] A. A. Abdo et al. PSR J1907+0602: A Radio-Faint Gamma-Ray Pulsar Powering a Bright TeV Pulsar Wind Nebula. *The Astrophysical Journal*, 711:64–74, March 2010.
- [261] A. A. Abdo et al. Observations of Milky Way Dwarf Spheroidal Galaxies with the Fermi-Large Area Telescope Detector and Constraints on Dark Matter Models. *The Astrophysical Journal*, 712:147–158, March 2010.
- [262] A. A. Abdo et al. Observation of Supernova Remnant IC 443 with the Fermi Large Area Telescope. *The Astrophysical Journal*, 712:459–468, March 2010.
- [263] A. A. Abdo et al. Fermi Large Area Telescope Search for Photon Lines from 30 to 200 GeV and Dark Matter Implications. *Physical Review Letters*, 104(9):091302–+, March 2010.
- [264] A. A. Abdo et al. Spectrum of the Isotropic Diffuse Gamma-Ray Emission Derived from First-Year Fermi Large Area Telescope Data. *Physical Review Letters*, 104(10):101101–+, March 2010.

- [265] A. A. Abdo et al. Discovery of Pulsed  $\gamma$ -Rays from PSR J0034-0534 with the Fermi Large Area Telescope: A Case for Co-Located Radio and  $\gamma$ -Ray Emission Regions. *The Astrophysical Journal*, 712:957–963, April 2010.
- [266] A. A. Abdo et al. Fermi Large Area Telescope Observations of PSR J1836+5925. *The Astrophysical Journal*, 712:1209–1218, April 2010.
- [267] A. A. Abdo et al. Fermi Large Area Telescope Observations of the Vela-X Pulsar Wind Nebula. *The Astrophysical Journal*, 713:146–153, April 2010.
- [268] A. A. Abdo et al. The Vela Pulsar: Results from the First Year of Fermi LAT Observations. *The Astrophysical Journal*, 713:154–165, April 2010.
- [269] A. A. Abdo et al. The First Fermi Large Area Telescope Catalog of Gamma-ray Pulsars. *The Astrophysical Journal Supplement Series*, 187:460–494, April 2010.
- [270] A. A. Abdo et al. Constraints on cosmological dark matter annihilation from the Fermi-LAT isotropic diffuse gamma-ray measurement. *Journal of Cosmology and Astroparticle Physics*, 4:14–+, April 2010.
- [271] A. A. Abdo et al. Detection of the Energetic Pulsar PSR B1509-58 and its Pulsar Wind Nebula in MSH 15-52 Using the Fermi-Large Area Telescope. *The Astrophysical Journal*, 714:927–936, May 2010.
- [272] A. A. Abdo et al. Fermi-Large Area Telescope Observations of the Exceptional Gamma-ray Outbursts of 3C 273 in 2009 September. *The Astrophysical Journal Letters*, 714:L73–L78, May 2010.
- [273] A. A. Abdo et al. The First Catalog of Active Galactic Nuclei Detected by the Fermi Large Area Telescope. *The Astrophysical Journal*, 715:429–457, May 2010.
- [274] V. A. Acciari et al. The Discovery of  $\gamma$ -Ray Emission from the Blazar RGB J0710+591. *The Astrophysical Journal Letters*, 715:L49–L55, May 2010.
- [275] M. Ackermann et al. Constraints on dark matter annihilation in clusters of galaxies with the Fermi large area telescope. *Journal of Cosmology and Astroparticle Physics*, 5:25–+, May 2010.
- [276] Fermi-LAT Collaboration et al. Fermi Gamma-Ray Imaging of a Radio Galaxy. *Science*, 328:725–, May 2010.
- [277] A. A. Abdo et al. The Spectral Energy Distribution of Fermi Bright Blazars. *The Astrophysical Journal*, 716:30–70, June 2010.
- [278] M. Ackermann et al. GeV Gamma-ray Flux Upper Limits from Clusters of Galaxies. *The Astrophysical Journal Letters*, 717:L71–L78, July 2010.
- [279] A. A. Abdo et al. Fermi Large Area Telescope Observations of the Supernova Remnant W28 (G6.4-0.1). *The Astrophysical Journal*, 718:348–356, July 2010.
- [280] A. A. Abdo et al. Fermi Large Area Telescope View of the Core of the Radio Galaxy Centaurus A. *The Astrophysical Journal*, 719:1433–1444, August 2010.
- [281] A. A. Abdo et al. Gamma-Ray Emission Concurrent with the Nova in the Symbiotic Binary V407 Cygni. *Science*, 329:817–821, August 2010.
- [282] A. A. Abdo et al. Fermi Large Area Telescope Observations of Gamma-ray Pulsars PSR J1057-5226, J1709-4429, and J1952+3252. *The Astrophysical Journal*, 720:26–40, September 2010.
- [283] A. A. Abdo et al. Fermi-LAT Observations of the Geminga Pulsar. *The Astrophysical Journal*, 720:272–283, September 2010.
- [284] A. A. Abdo et al. The Fermi-LAT High-Latitude Survey: Source Count Distributions and the Origin of the Extragalactic Diffuse Background. *The Astrophysical Journal*, 720:435–453, September 2010.
- [285] A. A. Abdo et al. Fermi Large Area Telescope Observations of Misaligned Active Galactic Nuclei. *The Astrophysical Journal*, 720:912–922, September 2010.
- [286] M. Ackermann et al. Fermi Gamma-ray Space Telescope Observations of Gamma-ray Outbursts from 3C 454.3 in 2009 December and 2010 April. *The Astrophysical Journal*, 721:1383–1396, October 2010.

- [287] A. A. Abdo et al. Fermi Large Area Telescope and Multi-wavelength Observations of the Flaring Activity of PKS 1510-089 between 2008 September and 2009 June. *The Astrophysical Journal*, 721:1425–1447, October 2010.
- [288] A. A. Abdo et al. Gamma-ray Light Curves and Variability of Bright Fermi-detected Blazars. *The Astrophysical Journal*, 722:520–542, October 2010.
- [289] A. A. Abdo et al. Fermi-LAT Study of Gamma-ray Emission in the Direction of Supernova Remnant W49B. *The Astrophysical Journal*, 722:1303–1311, October 2010.
- [290] A. A. Abdo et al. Fermi Large Area Telescope observations of Local Group galaxies: detection of M 31 and search for M 33. *Astronomy & Astrophysics*, 523:L2+, November 2010.
- [291] A. A. Abdo et al. Fermi Large Area Telescope Observation of a Gamma-ray Source at the Position of Eta Carinae. *The Astrophysical Journal*, 723:649–657, November 2010.
- [292] M. Ackermann et al. Searches for cosmic-ray electron anisotropies with the Fermi Large Area Telescope. *Physical Review D*, 82(9):092003–+, November 2010.
- [293] M. Ackermann et al. Fermi LAT observations of cosmic-ray electrons from 7 GeV to 1 TeV. *Physical Review D*, 82(9):092004–+, November 2010.



# Gamma-ray bursts Coordinate Network Circulars

- [294] F. Piron et al. GRB 100225A: Fermi LAT detection. *GRB Coordinates Network, Circular Service, 10450, 1 (2010)*, 450:1–+, 2010.
- [295] F. de Palma et al. GRB 100325A: Fermi LAT detection. *GRB Coordinates Network, Circular Service, 10548, 1 (2010)*, 548:1–+, 2010.
- [296] F. de Palma et al. GRB 090902B: Fermi LAT detection. *GRB Coordinates Network, 9867:1–+*, 2009.
- [297] F. de Palma et al. GRB 090902B: Fermi LAT and GBM refined analysis. *GRB Coordinates Network, 9872:1–+*, 2009.
- [298] F. de Palma et al. GRB 091031: Fermi LAT detection of a faint burst. *GRB Coordinates Network, 10163:1–+*, 2009.



# Conferences proceedings

- [299] F. de Palma, Fermi LAT collaboration, and Fermi GBM collaboration. Grb 090902b, a long grb with high energy emission detected with fermi. 2010. (referato e accettato per la pubblicazione).
- [300] F. de Palma, Fermi LAT collaboration, and Fermi GBM collaboration. Grb090510: a short bright and hard grb detected by fermi. *AIP Conference Proceedings*, 1223(1):173–182, 2010.